AN ABSTRACT OF THE DISSERTATION OF

Levi F. Kilcher for the degree of Doctor of Philosophy in Oceanography presented on December 1, 2010.

Title: Dynamics of the Columbia River tidal plume

Abstract approved: _____

Jonathan D. Nash

This dissertation investigates the dynamics of the tidally modulated outflow from the Columbia River mouth using high resolution measurements of velocity, density and turbulent microstructure. At high tide, flow through the river mouth reverses from flood (onshore) to ebb (offshore). During ebb, buoyant fluid issues from the river mouth and spreads offshore across the ocean surface. This is the Columbia River tidal plume. The fluid velocity of the tidal plume is super-critical (greater than the wavespeed of coastal stratification), which creates a zone of sharp surface velocity convergence at its leading edge, causing a front to form. From early ebb to peak ebb, constant front propagation speed and plume expansion rate are controlled by a linearly increasing volume-flux through the river mouth. Within the plume, turbulence at the plume base is strongly related to the difference between the shear-squared, S^2, and four times the buoyancy frequency squared, $4N^2$. A parameterization based on the excess shear-squared, $S^2 - 4N^2$, represents Reynolds

stress well, indicating that it is driven by Kelvin-Helmholtz instability. During peak ebb of large tides, high volume-flux through the mouth drives high $S^2 - 4N^2$, causing high plume-base stress, which forces significant deceleration of the plume. During smaller tides the volume-flux is smaller, $S^2 - 4N^2$ lower, and the stress too weak to significantly decelerate the plume. During mid-ebb of both small and large ebbs, increasing buoyancy flux from the river mouth raises plume stratification, which suppresses $S^2 - 4N^2$ and stress. As ebb ends, decreasing volume flux and deflection by the Coriolis effect limit plume expansion. This weakens surface velocity convergence, causing the front to diffuse. On longer timescales, plume N^2 is modulated by changes in river flow; higher river flow causes higher N^2. During peak ebb of large tides this increase in N^2 supports higher S^2, resulting in higher $S^2 - 4N^2$, which causes larger internal stress. These results describe the primary dynamics of the Columbia River tidal plume from front formation to late-ebb, and relate variability in those dynamics to tidal and river-flow forcing.

Dynamics of the Columbia River tidal plume

by

Levi F. Kilcher

A DISSERTATION

submitted to

Oregon State University

in partial fulfillment of
the requirements for the
degree of

Doctor of Philosophy

Presented December 1, 2010
Commencement June 2011

Doctor of Philosophy dissertation of Levi F. Kilcher presented on December 1, 2010.

APPROVED:

Major Professor, representing Oceanography

Dean of the College of Oceanic and Atmospheric Sciences

Dean of the Graduate School

I understand that my dissertation will become part of the permanent collection of Oregon State University libraries. My signature below authorizes release of my dissertation to any reader upon request.

Levi F. Kilcher, Author

ACKNOWLEDGEMENTS

Thanks, most of all, to Jonathan Nash. Jonathan was an excellent adviser and a supportive mentor. Jonathan has taught me that effectively communicating ideas is at least as important as forming them. For this, and numerous other lessons, I am grateful. Thank you Jonathan for your support, patience and effort. Thanks also to my co-adviser, Jim Moum. Jim's pragmatic, businesslike approach to his work – which he obviously enjoys – is a model for productivity and professionalism that I value highly. This work would not have been possible without the instrumentation that he and the mixing group have developed.

I would also like to thank my committee members, Ed Dever and Kipp Shearman, for their support, time and perspective. Thanks to Bill Smyth and Roland De Szoeke. Roland served on my committee until he retired, and Bill was an informal member of my committee throughout my time at COAS. Their support, perspective and encouragement was always valuable and appreciated. Thank you John Schmitt, for your time serving as my graduate representative.

This work would not be possible without the technical expertise of Ray Kreth, Mike Neeley-Brown and Alexander Perlin. From long days at the lab prepping Chameleon, to monotonous hours waiting for it to hit "bottom", I always enjoyed the laughs.

Thanks to everyone on the River Influences on Shelf Ecosystems (RISE) project,

for providing a fun and collaborative research group. Thanks, as well, to the Captain and Crew of the R/V Pt. Sur, and to everyone who helped with Chameleon profiling: S. Kelly, R. Bjorkquist, D. Franklin, E. Spahn, G. Avicola, and A. Horner-Devine. Thanks to the National Science Foundation for funding my research (grant OCE-0238727).

Thanks to my peers, Satoshi Kimura, Sam Kelly, Jeffrey Early, Anthony Kirincich and Emily Shroyer, for scientific discussion, late nights in the office, $5 lunches and health-care debates. Thanks to Aaron Richards, for tofu curry dinners in the grasslands, breakfast sandwiches at camp 4, epic days in Tuolomne and everything along the way. Thanks Aaron, James Scott and Logan Mitchell for catching me on 25' whippers. Thanks to the Corvallis Ultimate community, and especially the Divas for three years of laughs and life lessons.

Thank you to open-source software developers. In particular, thanks to TeX and LaTeX developers everywhere, Marten O. Alver for JabRef, Guido van Rossum and the Python community, and John Hunter and the entire MatPlotLib team. Thanks to Linus Torvalds and all developers of the Linux kernel and the Linux-based operating systems I have used (Red Hat, Debian and Ubuntu). My PhD was made far more productive, and sane, by these powerful, open tools.

And of course, thanks to my family: my mother, for *always* being there and telling me what I needed to hear; my father, for caring as much as he does; my brother Eivin, for balancing me out and taking me to Thailand; my new sister,

Ellen, for proof-reading at the last minute; and August, Charlotte, Pam and Torrey, for your love and support. Thanks to Jessica Luna, for caring enough to endure these last few months.

This work is dedicated to my grandparents,

John and Colleen McKemie, Joan and Mark Keeney, Yule Kilcher and Ruth Marriott.

CONTRIBUTION OF AUTHORS

Dr. Jonathan D. Nash was involved in the writing and analysis of chapters 2 and 3. Dr. James N. Moum contributed writing and analysis to chapter 3. Dr. Nash was the primary investigator during the research cruises in which data for this dissertation was obtained.

TABLE OF CONTENTS

TABLE OF CONTENTS (Continued)

TABLE OF CONTENTS (Continued)

LIST OF FIGURES

LIST OF FIGURES (Continued)

LIST OF FIGURES (Continued)

LIST OF APPENDIX TABLES

Chapter 1 – Introduction

Throughout its history, human civilization has been closely linked to rivers. As populations have grown and technologies have extended our ability to control and influence our environment, the influence of human activity on river systems has increased remarkably. As we are increasingly faced with the realities of this powerful new role, an environmental ethic of reducing our impact on the environment is gaining popularity (e.g. *Moore and Nelson*, 2010). Because of the complexity of the earth system, and the socioeconomic system within it, this ethic demands detailed knowledge of the processes that are involved in, and being altered by, this anthropogenic change.

In the midst of today's fast-paced lifestyle, we often forget the vital services that rivers provide. Humans use rivers for drinking, power generation, transportation, agriculture, recreation and waste-dispersal. Freshwater is becoming an increasingly scarce and valuable resource (*Vörösmarty et al.*, 2010). This being the case, greater attention is being paid to all aspects of the hydrologic cycle. Much of this interest is focused on the equitable usage of freshwater before it mixes with the ocean. However, as evidence mounts that coastal ecosystems are impacted by anthropogenic pollutants and nutrients carried downstream by rivers (*Halpern et al.*, 2008), a greater urgency for understanding downstream freshwater mixing processes has emerged. This dissertation relates the dynamics of the Columbia

River outflow to its estuary and coastal forcing (river flow, wind and tides). By describing an energetic process that powers river-ocean mixing, this research contributes to a greater understanding of an important component of the hydrologic cycle.

1.1 Physical Setting

Rivers and oceans connect through a broad range of geological forms, spatial scales and flow patterns. In the broadest sense, the geology of these connections is distinguished by the existence, or not, of a river delta. River deltas form at the mouths of rivers where sediment accumulation overwhelms sediment export, which causes branched networks of waterways to form and distribute the river outflow over a broad section of coastline.

Where sediment accumulation does not form a delta, a single narrow estuary is the geological structure that connects a river to an ocean. This is the structure that connects the Columbia River to the Pacific Ocean. In this type of river-ocean connection, the mixing between river and ocean water is divided into three primary domains: 1) the estuary, where freshwater first encounters and mixes with seawater, 2) the near-field river plume, in which estuary water discharges into the coastal ocean and transitions from estuary to a regime dominated by coastal dynamics, and 3) the far-field river plume, where wind-forced mixing drives the final mixing of river water into the coastal ocean. The near-field plume domain is the subject of this dissertation, but I will first outline the important features of the Columbia

River estuary and the far-field plume.

1.1.1 The Columbia River

Located in the Pacific Northwest of the United States (U.S.), the Columbia River is the fourth largest river in the U.S. by flow rate, and the largest that discharges into the eastern Pacific Ocean. Its average volume flow rate is $\approx 7,000\text{m}^3/\text{s}$, and peaks to $> 12,000\text{m}^3/\text{s}$ during the spring freshet. The Columbia River drainage basin is $660,480\text{km}^2$ (*Sherwood et al.*, 1990), and stretches across the states of Idaho, western Montana, south-eastern British Columbia, eastern Washington and Oregon (Figure 1.1).

During the mid-20^{th} century, a series of dams were constructed along the Columbia River for power generation and flood prevention. These dams subdued the seasonal cycle of the river flow. Prior to this regulation, peak spring-freshet flow rates exceeded $25,000\text{m}^3/\text{s}$ (more than double current flow rates). Throughout the remainder of the year, modern river flow conditions generally exceed historical. Historical late-summer flow was sometimes as low as $1,000\text{m}^3/\text{s}$. Now, river flow rarely drops below $2,000\text{m}^3/\text{s}$ (*Sherwood et al.*, 1990).

1.1.2 The estuary: source to the near-field

The Columbia River estuary is a "drowned river valley" or "coastal plain" type estuary (*Simenstad et al.*, 1990). This indicates that the depth of the estuary is

relatively uniform for many kilometers from the mouth. This rather open connection to the ocean allows tides to propagate into the estuary and drive strong tidal velocities. This is distinct from "fjord" and "bar-built" type estuaries which generally deep inner basins connected to the ocean through a shallow sill at the mouth, causing tidal velocities within to be relatively weak *Pritchard* (1967).

In contrast, strong tidal velocities often drive significant mixing in coastal-plain estuaries. This mixing has been classified into three categories: 1) salt-wedge, 2) partially-mixed, and 3) well mixed *Pritchard* (1955); *Hansen and Rattray, Jr.* (1965). These regimes are classified by the strength of stratification in the estuary, and can be distinguished by the ratio of the river flow to the tidal currents. In well mixed estuaries, strong tides compared to river flow force intense top-to-bottom mixing and set up an unstratified along-channel density gradient. In salt-wedge, or highly stratified estuaries, tidal velocities are weaker than the river flow. This allows buoyant surface fluid to flow over the top of saltier water (the salt-wedge) that flows upstream through the mouth, along the bottom of the estuary. Strong stratification at the interface between the two layers helps to suppress mixing. Partially-mixed estuaries are intermediate to these two extremes.

The Columbia River estuary is a partially-mixed estuary. During most river flow levels a mid-depth stratification peak is present, as well as a significant along-channel surface density gradient. Tidal flow advects this gradient and a salt-wedge up and down the estuary. Though regulation has reduced the seasonality of the river flow, the variability that occurs does cause the estuary to vary between more and less strongly stratified periods. Stratification increases during high river flow,

causing the estuary structure to become more salt-wedge like. During low flow, stratification is suppressed and surface salinity increases *Jay and Smith* (1990a); *Nash et al.* (2009).

1.1.3 The far-field plume, context for the near-field

The far-field plume, as with most coastal systems, is dominated by wind-forcing and Coriolis acceleration, with the added influence of elevated stratification. During weak winds, water emerging from the estuary mouth forms a re-circulating "bulge" (*Chao and Boicourt*, 1986; *Yankovsky and Chapman*, 1997; *Horner-Devine*, 2009) that can retain a significant fraction of the estuary discharge to within a few Rossby-radii of the mouth. This raises the near-surface stratification of waters in the vicinity of the mouth. Water that escapes the bulge flows north along the Washington coast in a geostrophic coastal current.

Winds off the Oregon and Washington shelves change direction from predominantly upwelling (southward) during summer to predominantly downwelling (northward) during winter. Downwelling winds suppress bulge formation and intensify the northward coastal current. Reversal of the wind to upwelling, pushes this coastal current offshore and causes significant mixing along the offshore edge of the plume (*Chapman and Lentz*, 1994; *Yankovsky and Chapman*, 1997; *Lentz and Largier*, 2006).

Sustained upwelling conditions (typical in summer) push Columbia River water to the south and offshore (*Barnes et al.*, 1972; *Berdeal et al.*, 2002). Sustained

winds thus help to move plume fluid away from the river mouth. Reversing winds, on the other hand, can retain more plume fluid in the vicinity of the river mouth (*Hickey et al.*, 2009). As was the case for bulge formation, such retention of buoyant fluid near the mouth raises the stratification of this region, and thereby alters the near-field environment into which new estuary fluid emerges (*Fong et al.*, 1997; *Fong and Geyer*, 2001, 2002, e.g.).

1.2 Outline

The near-field region of the Columbia River is dominated by tidal variability. During flood, rising tides force water from the near-field region to flow into the estuary. As the tide reverses (ebbs), buoyant estuary fluid issues from the river mouth and spreads across the ocean surface. This spreading layer of fluid is the "tidal plume." At the leading edge of the tidal plume, intense surface velocity convergence causes a front to form that propagates up to 30km offshore.

This dissertation describes and diagnoses the dynamics of the tidal plume: chapter 2 investigates the "outer plume", or plume front, and chapter 3 investigates the dynamics of the nearfield "inner plume". The following gives a brief overview of each region and of relevant prior studies.

1.2.1 The outer plume: small-scale fronts

Throughout the 1970's and 1980's Richard W. Garvine's research provided some of the earliest observations of the internal structure of small-scale river plumes (*Garvine*, 1974a). This work showed that a narrow "foam line", visible in aerial photographs, coincided with a sharp surface density gradient. In *Garvine and Monk* (1974), the authors documented strong convergence and downwelling at the front, which brought buoyant surface fluid down and created unstable stratification in the frontal region. This flow structure has since been described as a "rotor" circulation (*Luketina and Imberger*, 1987).

Garvine and Monk (1974) also established that the length scale of these fronts was too small for their dynamics to be influenced by the earth's rotation and that their propagation was driven by a cross-front hydrostatic pressure gradient. In other words, these fronts propagated as buoyant gravity currents (*Benjamin*, 1968).

Luketina and Imberger (1987) investigated the outflow of estuary water from a narrow channel in Leschenault Estuary. The authors showed that the discharge formed a surface buoyant jet. As the discharge volume flux through the channel increased linearly in time, the jet strengthened and its length scale extended farther and farther offshore. At the offshore end of the jet, where the flow became sub-critical, a radially spreading plume developed. Fed by the discharge, the front of this plume expanded with constant velocity.

In chapter 2 we present observations of the Columbia River tidal plume front,

which was observed to have similar structure and dynamics as *Garvine and Monk* (1974) and *Luketina and Imberger* (1987). However, important distinctions and extensions are made. Thanks to the invention of acoustic Doppler profilers, we observed the velocity field of the Columbia River front at much higher resolution than those studies. In addition to resolving the generation of non-linear internal waves (NLIWs) at the plume front *Nash and Moum* (2005), these tools also captured the growth and formation of fronts at the end of the Columbia River bar. We show that NLIWs are often observed as a part of a complex frontal structure. It is possible that similar features, under-resolved in previous measurements, are the true nature of what have often been called "multiple fronts" (e.g. *Luketina and Imberger*, 1987). Furthermore, we extend the findings of *Luketina and Imberger* (1987) in suggesting a mechanism of frontal deceleration. This provides a synoptic perspective of the Columbia River plume front and its dominant dynamics, from formation and growth to eventual decay.

1.2.2 The inner plume: turbulent stress in the plume base

Chapter 3 investigates the momentum balance of the outflow from the Columbia River mouth during ebb. A number of works have indicated the importance of vertical mixing in the mass and momentum budgets of buoyant discharges (*Wright and Coleman*, 1971; *MacDonald and Geyer*, 2004; *Chen and MacDonald*, 2006; *Hetland*, 2005). However, only *Luketina and Imberger* (1989) and *MacDonald et al.* (2007) have made direct estimates of turbulent quantities that can be used

to estimate vertical fluxes. The temporal and spatial sampling of our data provides high resolution of the velocity, density and turbulent structure of the plume. We are able to estimate the majority of the terms in the momentum balance directly from our observations. Those that can not be estimated directly are estimated using a control-volume technique similar to *MacDonald and Geyer* (2004). This provides an estimates of the plume momentum balance so that we are able to show that the turbulent friction can play a significant role in decelerating plume fluid.

Figure 1.1: Map of the Columbia River drainage basin. Topography data from the U.S. Geological Survey, GTOPO30 dataset. Watershed data from Hydro1k dataset, estimated according to *Verdin and Verdin* (1999) based on GTOPO30. Image courtesy of Karl Musser and wikimedia.

Chapter 2 – Structure and dynamics of the Columbia River tidal plume front

Levi F. Kilcher, Jonathan D. Nash

Journal of Geophysical Research, Oceans

2000 Florida Avenue N.W., Washington, DC 20009

Volume 115, C05S90, 2010

Abstract

Time-dependent buoyant plumes form at the outflow of tidally-dominated estuaries. When estuary discharge velocity exceeds plume internal-wavespeed, c, a sharp front forms at the plume's leading edge that expands from the time-dependent source. Using observations of the Columbia River tidal plume from multiple tidal cycles we characterize time evolving plume structure and quantify front speed (U_f), plume internal-wavespeed, c, front curvature, and ultimate extent. We identify three distinct stages of propagation: (1) initially the plume is strongly influenced by shallow bathymetry near the river mouth. (2) As the front advances offshore the plume detaches from the bottom and expands as a freely-propagating gravity current with relatively constant U_f, c and frontal Froude number, $F = U_f/c$. Ambient currents explain intra-cycle variability in U_f and winds alter front shape. Variability in ambient stratification associated with previous cycles' plume remnants leads to complex fronts and internal waves. (3) Finally, the plume decelerates, adjusts towards geostrophy, and may radiate additional internal waves. Using a simple kinematic model, we suggest that constant frontal propagation speed, $U_f = 0.9 \pm 0.1$m/s, during stage 2 is primarily controlled by linearly increasing discharge from the Columbia River mouth. As this discharge rate subsides, the plume expands as a fixed volume with decreasing front speed (stage 3). The plume's final extent is controlled by the Rossby radius, which scales with a length based on the total volume discharged. This provides an integral description of plume front evolution based on the time dependent estuary discharge.

2.1 Introduction

Over the last half century considerable scientific effort has been devoted to regions of freshwater influence, those parts of the oceans whose physical, biological and chemical properties are strongly affected by river input (*Simpson*, 1997). This effort has focused in two distinct domains: the estuary (e.g. *Jay and Smith*, 1990b) and the far-field river plume (e.g. *Fong et al.*, 1997).

Estuaries are the domain in which fresh river water first encounters sea water. Their dynamics are largely determined by the competition between tidal stirring/mixing and freshwater input from upstream (*Hansen and Rattray, Jr.*, 1966; *Bowden and Gilligan*, 1971; *Jay and Smith*, 1990b; *Nash et al.*, 2009). Far-field plumes are low-salinity mesoscale features that disperse river water across coastal margins. Their dynamics are dominated by buoyancy, planetary rotation and wind forcing (*Yankovsky and Chapman*, 1997; *Fong and Geyer*, 2002; *Hickey et al.*, 2005). As interest in these domains has grown, so has attention to the processes that connect them. *Horner-Devine et al.* (2009) conceptualized four dynamic regimes: the source (i.e. estuary), tidal plume, re-circulating plume (*Yankovsky and Chapman*, 1997; *Horner-Devine*, 2009) and far-field plume. This work focuses on the tidal plume.

Fed by the ebb discharge from a river mouth, a tidal plume is an expanding volume of buoyant fluid that spreads offshore along the ocean surface. The dynamics and characteristics of tidal plumes are distinct from both estuaries and far-field plumes. In contrast to far-field plumes, they are highly time dependent

(tidally modulated), much smaller scale, and their dynamics are – at least initially – independent of the earth's rotation (*Garvine and Monk*, 1974). In contrast to estuaries, tidal plumes are not constrained by a river channel so are highly three-dimensional. Throughout this work we use the terms "plume" and "tidal plume" interchangeably and distinct from the larger scale "far-field plume".

2.1.1 Tidal plume fronts

Some of the earliest observations of tidal plume fronts were made at the Connecticut River mouth. *Garvine and Monk* (1974) identified "vigorous" convergence at the horizontally propagating plume front and determined that propagation was driven by the cross-front density gradient. Isopycnals were displaced downward in the O(50m) wide front. Inshore of it they were shallower and horizontal.

Luketina and Imberger (1987) (hereafter LI87) described the liftoff and radial expansion of the tidal plume that formed from the discharge of a small estuary into Koombana Bay, Australia. That work described frontal structure as rotary circulation around a turbulent core (see their Figure 2). *Marmorino and Trump* (2000) document further evidence of this head structure in the Chesapeake Bay plume. In the Columbia River tidal plume's front, intense turbulence and large vertical displacements support LI87's diagram of frontal structure (*Orton and Jay*, 2005). Throughout these studies it has been clear that these fronts propagate as buoyant gravity currents.

Beyond the mouth LI87 described two regimes: 1) a surface buoyant jet whose

cross-shore extent moved steadily offshore as ebb discharge through the mouth strengthened; 2) a buoyant plume that expanded radially from the location of the jet's extent. This resulted in a total front propagation speed that was the sum of the jet-extent translation speed and the plume spreading rate.

2.1.2 Gravity currents

In his seminal work on gravity currents, *Benjamin* (1968) proposed that the frontal Froude number,

$$F = \frac{U_f}{c} \qquad , \tag{2.1}$$

should be an order one function of the non-dimensional layer depth (ratio of plume thickness, h, to the full water depth, d). Here U_f is the gravity current front's speed relative to the ambient fluid and c is the 1^{st}-mode long-wavespeed within the plume. In the deep-water limit, Benjamin predicted, $F = \sqrt{2}$. More recently, in a lock-release framework, *Shin et al.* (2004) have proposed that $F = 1$ is the most appropriate value for deep-water gravity currents. Regardless of the debate regarding the specific value of F, LI87 and *Marmorino and Trump* (2000) observe F to be roughly constant and $O(1)$ (throughout this work, $O()$ is used to indicate the order of magnitude of the quantity in question).

2.1.3 Tidal plume models

In an effort to dynamically model a time-dependent plume, *Garvine* (1984) assumed a radially spreading flow with steady source conditions. Garvine simplified the plume dynamics to a two-layer system involving the shallow-water wave equations and assumed the front propagated as a gravity current (he used a $F = \sqrt{2}$ frontal condition). More recently, *Jay et al.* (2010) formulate a model that conserves mass, momentum and buoyancy in a quasi-steady, front-following frame. Rather than prescribing the frontal Froude number, *Jay et al.* (2010) explore the effect of different mass and momentum entrainment mechanisms on frontal evolution. Both models predict the plume front to propagate offshore with initially high deceleration that decreases offshore (i.e. front speed decreases rapidly, then more slowly).

Rapid deceleration conflicts LI87's observation that $U_f \approx$ Constant. Using *Chen* (1980)'s kinematic plume model (with $F =$ Constant frontal condition), LI87 found that roughly constant frontal propagation speeds could be explained if the volume flux through the mouth (the estuary discharge) increased linearly in time during the initial phase of the tidal cycle, a condition approximately observed. LI87's agreement between modeled and observed U_f evolution suggests the time dependence of the source discharge may be more important than both the dynamics of the plume interior (as in *Garvine*, 1984), and the details of frontal dynamics (as in *Jay et al.*, 2010) in predicting plume front motion.

2.1.4 Outline

This work describes the structure and explores the dynamics of the Columbia River tidal plume and front. While the Columbia plume is much larger than the small rivers in the above studies, there remain important similarities. For example, the Columbia River tidal plume source is highly supercritical, time dependent and produces a strong front (*Orton and Jay*, 2005). In less than 8hours this plume spreads estuary fluid greater than 20km offshore where it becomes strongly influenced by planetary rotation (*McCabe et al.*, 2008). Our observations capture front evolution from a bottom interacting regime through plume expansion to the tidal plume's ultimate adjustment toward geostrophy.

In section 2.2 we describe the physical and environmental setting of the observations and the measurements. Section 2.3 begins with a description of front shape and basic plume structure. Sections 2.3.3 and 2.3.4 describe the evolution of simple and complex fronts, respectively. The inter-ebb variability and intra-ebb evolution of plume structure and front speed, as well as estuary discharge are presented in section 2.4. In section 2.5 we employ *Chen* (1980)'s kinematic model to relate the evolution of front speed to the observed time dependence of the estuary discharge. Like LI87, we identify a regime of roughly constant U_f associated with the linearly increasing estuary discharge. We extend LI87's analysis to a "relaxation" regime – brought about by decreasing estuary discharge – during which the plume expands as a fixed volume and approaches geostrophic balance. Results and implications are summarized in section 2.6.

2.2 Setting and Data

The Columbia River flows into the Pacific Ocean from between the states of Washington and Oregon, U.S.A (Figure 2.1). Constricted by two jetties, the estuary narrows from 10 to 3.5km at the mouth and discharges its fluid westward into the relatively unbounded coastal ocean. Within 8km of the mouth is a relatively flat, shallow (water depth, $d \approx 20$m) region that is roughly radially symmetric about the tip of the north jetty; we refer to this as the "bar region". The 20m deep shipping channel, which runs from the river mouth to the southwest, is the primary exception to this symmetry (also, there is a 20m deep dredge pile at $(x, y) = (-8, 0)$km). Offshore of the bar region, the water depth increases rapidly from 20m to > 60m in only 2km (Figure 2.1a).

The origin of our chosen coordinate system is at 46.24° N, 124.08° W, with the positive x, u and y, v directions eastward and northward respectively (Figure 2.1b). The coordinate system is approximately aligned with the mean river discharge, perpendicular to the north-south coast, and has origin just north of the south jetty. z is defined as positive upward from the ocean surface.

2.2.1 Sampling

In August 2005, seven "front-tracking" experiments were performed from the R/V Pt. Sur as part of the River Influences on Shelf Ecosystems (RISE) study (*Hickey et al.*, 2010). During each tidal cycle approximately 8-15 E-W transects across the front were obtained as it propagated offshore (Figure 2.2a). This was continued

until the front was no longer a clear feature in the observations or when the ship returned inshore to catch the next ebb pulse. Each experiment is denoted by its "tidal ID" which is composed of the three letter month prefix ('aug') followed by its numeric day of August, followed by an 'a' or 'b' to denote the first or second ebb of that day, respectively. Repeated "Cross-mouth" transects, along lines 0 and 1 and over complete tidal periods (Figure 2.1b), resolved the cross-mouth structure and time dependence of estuary discharge. All transects were obtained at ship speeds of $4-6$knots.

2.2.2 Environmental Conditions

During our sampling, winds were mild, variable, and predominantly upwelling favorable (Figure 2.2b). Moderate winds ($O(5\text{m/s})$) were experienced during ebbs aug22a, aug22b and aug25b. River flow in August was low, $\approx 4,000\text{m}^3/\text{s}$, compared to peak freshet values in excess of $10,000\text{m}^3/\text{s}$ (*Hickey et al.*, 2010). Tidal elevations η, as computed from xtide (*Flater*, 2007) for the "Columbia River, N. Jetty" exhibit both a strong spring/neap modulation and variable diurnal inequality. We quantify the tidal drop $\Delta\eta_\circ$ for a given ebb as

$$\Delta\eta_\circ = \eta_{high} - \eta_{low} \quad , \tag{2.2}$$

where η_{low} is the tidal height minimum and η_{high} the preceding maximum (Figure 2.2c). Front tracking experiments capture a range of $\Delta\eta_\circ$ from 1.1 to 2.8m.

The strength of the diurnal inequality is represented by $\Delta\eta_\circ - \Delta\eta_{-1}$, where $\Delta\eta_{-1}$ is the prior ebb's tidal drop. For each experiment, time,

$$t = \hat{t} - t_{low} \qquad , \tag{2.3}$$

is referenced to the time of low tide, t_{low}, of the given ebb, where $\hat{t}$ is chronological time (Figure 2.2c).

2.2.3 Instrumentation

This work combines microstructure profiler measurements, shipboard acoustics and surface backscatter from X-band radar to capture the evolving internal plume structure and plan-view front shape.

Two RD Instruments acoustic Doppler current profilers (ADCPs) were used throughout this cruise. A hull-mounted 300kHz instrument measured velocities from 4.5 down to 100m below the surface in 1m bins. A 1200kHz instrument mounted 1.4m below the surface on a pole alongside the ship provided lower-noise velocity estimates in 0.5m bins from 2.2 to 24.2m depth. This data was preferred between $0 > z > -20$m. Both ADCPs bottom tracked and used 1.5s averaging intervals. A linear fit across data between 2.2 and 4.7m depth was used to extrapolate 1200kHz velocity data to the surface. A 120kHz Biosonics$^{\text{TM}}$ acoustic echosounder was mounted on a second pole 1m below the surface and recorded profiles of acoustic backscatter from zooplankton and turbulence every

0.5s in 0.017m bins.

Vertical profiles of conductivity, temperature, pressure, optical backscatter, velocity shear and temperature gradient were obtained every $1-3$minutes with the Chameleon microstructure profiler (*Moum et al.*, 1995). At this profile rate and ship speed, horizontal resolution was $100-500$m. Free-falling at 1m/s, Chameleon provides data with roughly 1cm vertical resolution. Turbulent kinetic energy (TKE) dissipation rate, ε, was calculated in 1m depth bins by fitting theoretical shear spectra to observed spectra from Chameleon's shear probes (*Moum et al.*, 1995). Estimates of ε were not obtained above 3m depth because the profiler was accelerating and changing orientation. Furthermore, contaminated ε data were identified when the ship orientation, drift and water-column shear combined to place the profiler in the ship's wake; this affected data, for short periods, down to 9m depth.

Images from the ship's X-band radar (e.g. Figure 2.1b), tuned to detect surface roughness, were captured every two-minutes. Bands of high radar backscatter intensity correspond with regions of surface velocity convergence (*Alpers*, 1985; *Marmorino et al.*, 2004). Bands were traced and indexed by hand then transformed into the earth's frame. These traces provide front position, shape and orientation as a function of time.

2.2.4 Front Identification

Because it is not always clear what internal feature a given band of elevated radar backscatter represents, it was necessary to use internal measurements to identify fronts. In general, front locations were identified objectively as the location of maximum horizontal velocity convergence at $z = -2.35$m. For well formed fronts, this also corresponds to the near-surface salinity gradient maximum $\left(\frac{\partial s}{\partial x}\right)_{max}$ at $z = -1.5$m and the frontal locations identified from echosounder and radar backscatter. When multiple or ambiguous fronts existed, it was necessary to use a salinity threshold to identify primary fronts and differentiate these from secondary fronts, which represented propagating wave-like disturbances either ahead or behind the main front (appendix A). When even this failed, front locations were interpolated between neighboring realizations. Ambiguity estimates were assigned subjectively to include all front locations that would be identified by alternate reasonable criteria. When fronts were simple and distinct these methods produced identical results (ambiguity is small). However, when frontal structure was complex (§2.3.4) these methods produce different results and front position ambiguity is large.

Front position, x_f, is defined as the intersection of the front with the x-axis. In cases where the front was identified away from the x-axis (experiments aug22b, aug25b), front locations were translated to the x-axis using radar estimates of front shape. This makes x_f a consistent variable for inter-ebb comparisons and minimizes error associated with radar derived front location estimates.

Based on these data, front speed is estimated as,

$$U_f^* = \frac{\Delta x'}{\Delta t} \qquad , \tag{2.4}$$

where Δt and $\Delta x'$ are the time and cross-front distance between realizations, respectively. Here $\Delta x' = |\vec{\Delta x}| \cos\phi$, where $|\vec{\Delta x}|$ is the magnitude of the vector connecting consecutive realizations of front position (x_f, y_f), and ϕ is the angle between this vector and the front-normal direction, determined from radar backscatter data (both vectors pointed generally westward). The velocity error upper bound was calculated by differencing front position ambiguity minima in one realization of front position from ambiguity maxima in the next, and vice-versa for the lower bound.

2.3 Plume front structure and evolution

2.3.1 Front shape and evolution

A defining characteristic of the Columbia River tidal plume is its time dependence. On each ebb, the pulsed discharge from the mouth generates a tidal plume that spreads offshore. Traces of front position illustrate this in plan view for 5 ebbs (Figure 2.3)[1].

[1]Ebbs aug08b and aug21a have been omitted from Figure 2.3. Traces of front aug08b are similar to those of aug09b until $t \approx$ 1hour at which time the ship returned inshore and the front was out of range of the radar. Due to wind and surface wave conditions many fronts were not resolved as clearly as aug09b. In particular front aug21a was nearly unidentifiable in radar images. Because of this incomplete and poor sampling these ebbs are not presented in Figure 2.3.

The second ebb of August 9$^{\text{th}}$ (aug09b) demonstrates plume-front evolution during a period of weak winds (Figure 2.3a). Four hours prior to low tide the front emerged from the estuary mouth. At this time it was "*S*" shaped and attached to the north jetty. Initially, the front propagated rapidly, as seen by large spacing between traces near $x = -4$km. During the next 15km ($-5 > x > -20$km) uniform trace spacing indicates constant, though slower, front speed. Throughout this time, increasing radius of curvature of traces suggests that the plume expanded radially. The centroid of expansion was near the x-axis so that the plume front was approximately normal to our ship track. Tighter trace spacing beyond -20km indicates front deceleration, after which the band of elevated radar backscatter was no longer visible.

Like aug09b, front aug21b emerged under weak wind conditions and was essentially perpendicular to the x-axis as it propagated offshore (Figure 2.3b). Between $x = -7$ and -16km (-2 to 0hours) this front propagated offshore more rapidly than any other. It then decelerated suddenly, released a nonlinear internal wave (NLIW) (i.e. *Nash and Moum*, 2005), and moved more slowly offshore over the remaining 8km. This rapid deceleration is explored further in section 2.4.3.

In contrast to the north-south symmetry of aug09b and aug21b, fronts aug22a, aug22b and aug25b propagated obliquely to the x-axis (Figures 2.3c,d,e). We attribute this asymmetry and associated plume deflection to the $\approx$ 5m/s wind that was blowing to the south during these periods, contrasting the weak winds during aug09b and aug21b. However, the magnitude of the plume's deflection exceeds that predicted by a wind-forced slab model, suggesting that wind-induced

surface currents may also contribute to plume shape and curvature.

Timing of frontal emergence – relative to low tide – varied from ebb to ebb and was uncorrelated with the wind. For example, front positions at low tide ($t = 0$) during ebbs aug22a and aug22b (similar wind conditions) were $x = -7$km and -15km, respectively. The relationship between front timing and the diurnal inequality is presented in section 2.4.5.

2.3.2 Plume Anatomy at Peak Ebb

We begin by describing the large-scale internal structure of a "classic" plume and gravity current front that resulted from propagation through a relatively homogeneous coastal environment (Figure 2.4). This front formed on the greater ebb of August 8$^{\text{th}}$ ($\Delta\eta_\circ - \Delta\eta_{-1} = 0.8$m), during spring tides ($\Delta\eta_\circ = 2.0$m) and weak and steady upwelling winds (Figure 2.2). It exhibited symmetrical spreading similar to aug09b (Figure 2.3a), but was not tracked past $x = -15$km. At the time of frontal crossing, at $x = -14$km, the front was moving offshore at $|U_f^*| = 0.96$m/s. The plume structure is most clearly visualized by elevated acoustic backscatter and shear squared, $S^2 = (\partial u/\partial z)^2 + (\partial v/\partial z)^2$ (Figure 2.4a,b), which have much higher horizontal resolution than Chameleon profile data. Density profiles in (b) clearly distinguish plume waters, which were often > 10kg/m^3 lighter than the ambient. Stratification, $N^2 = -g\rho_\circ^{-1}\partial\rho/\partial z$, can be inferred from the slope of density profiles. Coincidence of maximum N^2 and S^2 suggests S^2 is a useful representation of plume structure. Offshore of $x = -8$km, the over-arching plume structure is

that of a typical buoyant gravity current: led by a front, light fluid flows along the surface of a relatively motionless and denser ambient.

Within this over-arching structure, five regions of distinct internal structure are identified in Figure 2.4:

1. Liftoff ($x > -7.7$km)

The liftoff region extends from the river mouth across the bar region and is characterized by intense shear and turbulent dissipation throughout the water column. Throughout this region, the flow is super-critical, i.e., the depth mean fluid speed is greater than the 1^{st}-mode internal wavespeed. In this example, bands of high S^2, associated with the plume base, connect to the bottom at two locations ($x \approx -5.2$ and -7.7km), producing intense turbulent dissipation, ($\varepsilon > O(10^{-5}\text{W/kg})$), high bottom stress and sediment resuspension (*Spahn et al.*, 2009). These multiple attachment/detachment points are associated with individual liftoffs, which may result from (1) the flow disconnecting and reconnecting as it moves across the complex bathymetry, (2) the liftoff of an intermediate layer of plume fluid, or (3) the space-time aliasing inherent in our sampling. We also note that this liftoff region is not static, but moves in and out of the estuary with the tidal cycle; this snapshot is characteristic of its most seaward extent during peak ebb.

2. Transitional plume ($-11.3 < x < -7.7$km)

We identify two regions between liftoff and the front. The first, "transition" region, occurs offshore of liftoff and inshore of $x = -11.3$km. Here, S^2 and N^2 are high throughout the plume and TKE dissipation in the plume base ($\varepsilon = O(10^{-4}\text{W/kg})$) exceeds background levels by a factor of 1,000. We consider this a transition region because the flow appears to have "memory" of its bottom-interacting state (i.e. strongly sheared as in the liftoff region but no longer connected to the bottom). In addition, this region is considered transitional in that it rapidly thins from 20m when bottom-interacting to 10m. Surface velocities $|u(0)| > 2$m/s exceed the front speed by more than a factor of 2, which, combined with the strong vertical salinity gradient, efficiently supplies buoyant estuary fluid offshore toward the front. Numerous unstable overturns were observed in this region, such as that at $x = -8$km at 7m depth with $\varepsilon = O(10^{-3}\text{W/kg})$. Offshore of this, at nearly the same depth, a layer of weak stratification (profiles at -9.8 and -8.8km) is observed, likely a result of mixing.

3. Two-layer plume ($-13.5 < x < -11.3$km)

Offshore of $x = -11.3$km the plume had developed into a more well-mixed, 2-layer flow (S^2 and N^2 were concentrated at the plume base). Turbulence was strong in the plume base ($\varepsilon = O(10^{-5}\text{W/kg})$) but a lack of ε estimates in the surface (due to contamination by the ship's wake) inhibits comparing the detailed turbulent structure of this region to others.

4. Front ($-14.1 < x < -13.5$km)

The leading edge of the front is a region of intense horizontal convergence (u changes by > 1m/s in < 100m). This forces fluid downward at > 0.5m/s. Along the inshore side of the front upward velocities are > 0.3m/s, providing the return circulation for the turbulent rotor and "head" wave, as described by LI87. The head height, h_f, is the maximum isopycnal displacement through the front relative to the ambient fluid ahead of it, and often exceeds 20m (h_f is distinct from the plume thickness, h, defined as the depth of the 30salinity contour inshore of the front). Shear within the front is not well resolved, possibly due to small scales of variability relative to the ADCP footprint. A thin surface layer, $z > -2$m, of light fluid has been supplied to the front by the convergent flow. Below this, overturns of multiple scales are apparent in the density profile and TKE dissipation was extremely vigorous ($\varepsilon > 10^{-3}$W/kg).

5. Ambient ($x < -14.1$km)

The region offshore of the front provides context for the in-plume observations. At this time, ambient water is flowing weakly onshore ($u < 0.3$m/s) at the surface, and weakly offshore below 13m depth. This fluid is much less stratified, sheared and turbulent ($\varepsilon < 10^{-7}$W/kg) than within the plume.

The aggregate structure of these regimes portrays a plume structure that is in many ways similar to the smaller scale plumes described by LI87 (see their Figure 2), *Garvine* (1974b), and *Marmorino and Trump* (2000) in which an offshore

propagating front with a "turbulent core" in its head wave, is fed by a 2-layer surface flow that exceeds the front speed. In addition, we identify a transitional region associated with the thinning of highly sheared and stratified fluid that was recently interacting with the bottom, similar to (*Garvine*, 1984)'s supercritical "steady flow" regime (inshore of his "trailing front") and (*MacDonald and Geyer*, 2004; *MacDonald et al.*, 2007)'s "liftoff zone". This region may be considered analogous to LI87's "jet" regime.

Some distinctions between the above regimes are elucidated by considering wavespeeds of long first-mode internal waves as computed from the Taylor-Goldstein equation using the full density and velocity profiles in the geographic reference frame (*Drazin and Reid*, 2004). For example, within the liftoff region, the flow is supercritical (i.e., all disturbances propagate offshore). Thus, during peak ebb, information can be transmitted through the liftoff region to the plume, but not the other way around (the estuary controls the plume). In contrast, in the transition and two-layer regions, internal waves may propagate in either direction (phase velocities of offshore propagating waves are $\approx$ 1.5m/s, while those propagating onshore are $\lesssim$ 0.5m/s). At the front, a discontinuity exists; offshore propagating waves behind the front can catch up to it (their wavespeeds exceed the front speed), but can not propagate ahead of it into the ambient where the wavespeed ($<$ 0.4m/s) is lower than the front speed ($\approx$ 1m/s). Thus, at this time, dynamics at both the front and liftoff region can influence the plume between them, but not beyond. At the same time, because these locations act as barriers to internal wave propagation, they are locations where wave energy can build up or dissipate.

The location of plume liftoff appears to be strongly linked to topography, and is consistent with *Jones et al.* (2007)'s transition of a super-critical buoyant discharge to buoyancy driven (plume) dynamics. They define a "jet-to-plume" length scale,

$$L_M = \frac{U_\circ a^{1/4}}{(g'_\circ)^{1/2}} \qquad , \tag{2.5}$$

where a is the cross-sectional area of the mouth, $U_\circ$ the mean velocity through it, and $g'_\circ$ the reduced gravity. Appropriate values for the Columbia River are $a = 60,000\text{m}^2$, $U_\circ = 2\text{m/s}$ (peak ebb) and $g'_\circ = 0.07\text{m/s}^2$ (typical of August 2005). These values give $L_M = O(100\text{m})$. *Jones et al.* (2007) explain that L_M can only be interpreted as the horizontal scale for jet-to-plume transition if,

$$d \geq L_M/3 \qquad . \tag{2.6}$$

Thus, the discharge from the Columbia River mouth should interact strongly with the bottom until the water depth exceeds 30m. Offshore of this the flow is expected to behave as a plume/gravity current (i.e. driven by its buoyancy). Our observation that the flow interacts with the bottom until $x \approx -8\text{km}$ (Figure 2.4) is thus consistent with (2.6), and suggests that the liftoff location is connected to bottom depth variability.

While it is tempting to interpret the basic structure represented in Figure 2.4 as being typical, this is a single pseudo-snapshot (obtained as the ship moved offshore and the flow evolved slightly) of a "simple" plume. In practice, we observe plume evolution to be strongly influenced by 2 factors:

1. Temporal Variability. Nearly all the features of the flow – detachment point, front location, plume thickness, shear/stratification structure, turbulence, and flow direction – are controlled by the tidally variable upstream flow rate (estuary discharge). This causes these variables, and the plume in general, to be highly time dependent and rapidly evolving.

2. Spatial Complexity. In contrast to the distinct front in Figure 2.4 (which propagated through a relatively homogeneous coastal environment) most fronts exhibited a significant amount of spatial complexity. This complexity arises because the composition of plume source water changes in time and coastal waters are often "contaminated" with tidal plume remnants from previous tidal cycles.

In §2.3.3, we describe the time evolution of a simple tidal plume front with initial structure similar to that of Figure 2.4. This is contrasted (§2.3.4) with the evolution of two complex fronts, which, from our limited sampling, are more typical of the norm than the exception.

2.3.3 Plume Evolution I: A simple, distinct front

The evolution of the internal structure of front aug09b is summarized as a sequence of pseudo-snapshots in Figure 2.5. This front, generated by a greater ebb during spring tides and weak winds (Figure 2.2), resulted in a highly-symmetric frontal expansion (Figure 2.3a) with co-located frontal signatures in shipboard radar, density, velocity and TKE dissipation.

In its early stages (prior to column A and $t = -2$hours), the front was over the bar and the four plume regions identified in Figure 2.4 were not distinct. Instead, the plume and its front both strongly interacted with the bottom. In column A, this topographic influence was still evident as rapid thickening and enhanced ϵ at $x - x_f = 4$km, possibly associated with a hydraulic transition. In the following, we focus on the later time period when the plume front is freely propagating.

Initially (A), frontal displacements h_f are small – similar to the plume thickness behind the front. This may result because the front was recently constrained in amplitude by the shallow bar, and has had limited time for growth. As the plume evolved (A→B), h_f grew rapidly to $>$ 30m. However, in just 75 minutes, the front decayed by a factor of 3 to less than 10m (B→C). Based on the observed dissipation rates within the front ($\epsilon \approx 10^{-3}$W/kg) and the mean mechanical energy within the head of 2 J/kg (APE+KE; see *Moum et al.*, 2007, for method used), turbulence dissipation could erode the front in 30 minutes. Thus, NLIW radiation (i.e. *Nash and Moum*, 2005) is not needed to account for the observed decay in h_f. Ultimately, h_f and surface convergence weakened further (C→E), so that shipboard radar no longer resolved the front.

In contrast to h_f, which first grew then decayed in amplitude, plume velocity, u, and thickness, h, – defined as the depth of the 30salinity contour (thick contour in panels II, III, IV) – decreased monotonically. During this time, plume density was relatively constant (8 ± 1kg/m^3 lighter than ambient).

2.3.4 Plume Evolution II: Complex fronts

The frontal evolution of the remaining five plumes was much more complex than the simple structure described in §2.3.2-2.3.3. The front generated by ebb aug22a (Figure 2.6) illustrates many characteristics of complex fronts, which are generally associated with lateral variability of the stratification of the receiving waters (due to the presence of remnant tidal plume fluid). This front was generated by a lesser ebb during spring tides ($\Delta\eta_\circ = 2.1$m) and weak winds.

Initially the front is identified as the region of strong surface convergence and intense top-to-bottom turbulence (Figure 2.6A). At this time the estuary fluid inshore of the front is denser than the "remnant plume" fluid offshore of it. We term this counter-intuitive arrangement a "reverse front". Inshore of the reverse front velocity is maximum at the surface, ≈ 2m/s, and shear is strong throughout the water column. Offshore of it, fluid speeds are maximum below the remnant plume. Thus, the denser water issuing from the estuary is forced to flow beneath the more buoyant remnant plume. Intense dissipation ($\varepsilon = O(10^{-3}\text{W/kg})$) – possibly a result of convective instability – occurs at the frontal discontinuity ($x - x_f = 0$km) where dense surface waters are driven into the buoyant remnants. "Reverse fronts" (in which density decreased in the direction of propagation) were relatively common over the bar region during the initial stages of plume emergence, and were observed during ebbs aug21a, aug21b, aug22a and aug22b.

As the reverse front moved offshore, it detached from the bottom and was supplied with increasingly buoyant fluid from the estuary, thus reducing its density.

Eventually, densities onshore and offshore of the front became similar so that the cross-front surface density gradient was essentially non-existent (Figure 2.6B). However, a subsurface velocity maximum still persisted ahead of the front (B,C). In panel C, this feature is associated with downward displacement of isopycnals and elevated turbulence ($\varepsilon = O(10^{-5}\mathrm{W/kg})$).

As the front moved into denser, less stratified water (Figure 2.6C,D) it became a "proper" front, with surface density increasing in the direction of propagation (offshore). In column D multiple zones of surface density change and convergence exist. Two such features are identified: (1) the original "primary front" (filled triangle), and (2) a disturbance further offshore (open triangle). The latter is the lead wave in a train of NLIWs, identified primarily using velocity (Figure 2.6D, row III) and acoustic backscatter. Based on their location and speed, they could have been generated near the bar as ebb began (having propagated ahead of the primary front on the elevated ambient stratification). However, they were not observed earlier, possibly due to the complexity near the bar.

A band of elevated radar intensity (D, row I) coincides with a zone of elevated surface convergence (D, row II) 1km offshore of the primary front (inshore of the internal wave train). Between this feature and the primary front is a region of complex, wave filled, internal structure and intermediate density fluid.

At first glance this appears to be a second front. In column E, however, the primary front has overtaken the intermediate density fluid (causing its density gradient to sharpen). The waves, on the other hand, have continued to propagate offshore ahead of the primary front, as indicated by parallel bands of elevated radar

backscatter, $O(5-10\text{m})$ isopycnal displacements, wave shaped pulses of offshore flow and elevated ε. Back in the plume, the rapid change in thickness 3.5km inshore of the front (E) is reminiscent of Garvine's "trailing front" (see his Figure 4).

Tidal plume aug25b provides an alternate example of a complex front (Figure 2.7). This ebb was rather weak and occurred during a period of sustained upwelling winds (Figure 2.2). In this example a train of short-wavelength boluses formed ahead of the primary front (the lead disturbance is marked by an open triangle), visible in the acoustics but unresolved in the in-situ profiles.

As this front moved offshore, the sequence of boluses transformed into NLIWs with both larger amplitude and wavelength. It is unclear whether individual boluses grew to become waves or whether the entire packet transformed. Regardless of this distinction, in the final transect (column F) two large NLIWs are apparent and the high-wavenumber boluses are missing.

2.4 The front as a gravity current

In the preceding section a considerable amount of variability in plume internal structure was described, especially near the river mouth. Part of the complexity is associated with strong bottom interactions that occur in the liftoff region that prevent the plume from expanding as a freely-propagating gravity current. In the same region, reverse fronts – saltier water inshore of the front than offshore – were often observed. Ultimately, low-salinity fluid supplied to the front establishes a buoyancy anomaly conducive to an offshore-propagating surface gravity current.

In the following, we focus on the region offshore of liftoff ($x < b \equiv -8$km), where two classes of freely-propagating fronts were observed: simple and complex.

Simple fronts have internal structure of a classical gravity current (e.g. (*Benjamin*, 1968; *Simpson*, 1982)). That is, 1) their is only one front, 2) horizontal velocity and density gradients across it are sharp and coincident, 3) shear and stratification are concentrated in the plume base and 4) it often has a single "head" wave which displaces ambient fluid as much as 3 times the plume thickness. Such fronts occur when estuary fluid is released into quasi-uniform coastal waters.

In complex fronts, maxima in horizontal density gradient and surface velocity convergence were not co-located. Complex fronts were observed when the near-surface ambient stratification was elevated, allowing disturbances to propagate ahead of the primary front at speeds similar to frontal propagation. This is consistent with the modeling studies of *Stashchuk and Vlasenko* (2009), who showed that NLIW packets are more likely to form during periods of high near-surface ambient stratification.

Elevated stratification sets up conditions for both reverse and complex fronts. The presence of this fluid is related to surface winds. During ebbs aug21a and aug21b winds were weak and it is possible that remnant fluid was retained in this region by a "bulge" circulation (*Yankovsky and Chapman*, 1997; *Horner-Devine*, 2009). Alternatively, during ebbs aug22a and aug22b winds had reversed to upwelling and it seems possible that remnant fluid that had moved north in a coastal current was pushed south toward the estuary mouth where it interfered with these plumes.

Regardless of their differences, we observe that all fronts (both simple and complex) exhibit similar characteristics once they have detached from the bar region. In particular, they all freely propagate as buoyant gravity currents. In the following, we summarize the intra-ebb evolution of all fronts and investigate inter-ebb differences to characterize the source of the variability.

2.4.1 Front timing and NLIW emergence

The spatial evolution of each front is summarized in Figure 2.8a. Over the "bottom interaction" region ($x_f > b$) the fronts generated by lesser ebbs (aug21a and aug22a) propagated slowly, $U_f^* < 0.5$m/s (Figure 2.8b). As a result, t_b (the time the front crossed b) was $\approx$ 2hours later than that of greater ebbs. Variability in t_b is not strongly correlated with $\Delta\eta_\circ$, but is instead correlated with the diurnal inequality (see §2.4.5). Also note that these ebbs encountered strong surface stratification over the bar region and resulted in complex fronts.

Offshore of the bar ($-15\text{km} < x < b$, labeled "steady") the trajectories of primary fronts (solid lines in Figure 2.8a) exhibited similar character, producing relatively constant U_f^* between 0.8 and 1.2m/s (Figure 2.8b). At some point between $x = -15$ and -20km ("relaxation"), front speeds decreased approximately linearly, except for aug21b, which encountered strong ambient currents (see section 2.4.3). The location of initial deceleration varied from ebb to ebb (Figure 2.8b), with weaker ebbs generally decelerating inshore of larger ones. Front deceleration continued until front speed was $\approx$ 0.5m/s, after which time fronts were no longer

a clearly identifiable feature in the measurements.

Fronts aug21a, aug21b, aug22a, aug22b and aug25b each generated NLIWs that propagated through stratified ambient waters ahead of the primary front (Figure 2.8). Of these, only two NLIW packets (aug21b and aug22b) were clearly identified as having emerged from the deceleration of the primary plume front to below the NLIW wavespeed (the generation mechanism previously observed by *Nash and Moum* (2005) and modeled by *White and Helfrich* (2008)). Coincidentally, these were formed during the largest ebb pulses we sampled ($\Delta\eta_\circ = 2.8$ and 2.5 m).

In contrast, during the lesser ebbs on these same two days, wave packets were not linked to rapid frontal deceleration. For example, the lead NLIW generated during ebb aug21a was first observed ahead of the primary front at $x \approx b$, a time when it had been propagating relatively slowly. Similarly, NLIWs during aug22a were first identified more than 3km from the primary front (Figure 2.6D). It is possible that both of these packets were generated from shocks ahead of reverse fronts in the bar region; however, details of this process were not resolved by our sampling. Waves generated during aug25b appeared during the breakdown of short-wavelength boluses. A common theme in the above examples is that wave radiation is connected with frontal propagation through remnant plume waters. Moreover, these observations also suggest the mechanism documented by *Nash and Moum* (2005) is not the exclusive means of NLIW generation in the Columbia River tidal plume system. The simple front of aug09b decelerated without radiating NLIWs, apparently due to the fact that it propagated into more

weakly-stratified ambient fluid that, unlike the above examples, presumably could not support NLIW radiation (*Stashchuk and Vlasenko*, 2009).

In addition to waves excited ahead of the primary front, wave-like disturbances were also observed within the tidal plume itself. A secondary front during aug22b followed a similar trajectory to – but 2km inshore of – the primary front (Figure 2.8a). Secondary fronts have been documented in many previous studies of spreading flows (e.g. *Scarpace and Green III* (1973), *McClimans* (1978), LI87). LI87 hypothesized that multiple fronts were caused by perturbations of the estuary discharge inshore of the initial front. These perturbations then formed frontal features of their own that propagated offshore on the coat-tails of the ebb. Alternatively, *Garvine* (1984) suggested that multiple fronts can arise even within quasi-steady forcing since the system is nonlinear and susceptible to shear instability. Both lab (e.g. *Rottman and Simpson* (1983)) and numerical (e.g. *Ungarish and Huppert* (2004)) studies confirm that spreading plumes often become undulating and produce multiple fronts.

2.4.2 Plume thickness and density

The evolution and variability of the plume's dynamically important properties are shown in Figure 2.9. Plume thickness, h, is defined as the depth of the 30salinity contour. Plume density, ρ_p, is then estimated as the mean density over $0 > z > -h$.

With this, plume density anomaly,

$$\Delta\rho = \rho_\circ - \rho_p \qquad , \tag{2.7}$$

can be computed ($\rho_\circ = 1026.3\mathrm{kg/m^3}$). Two-layer wavespeed is computed as,

$$c_{2l} = \sqrt{g' \frac{h(d-h)}{d}} \qquad , \tag{2.8}$$

where d is the water depth and $g' = \rho_\circ^{-1} g \Delta\rho$ is the reduced gravity. The 1^{st}-mode long-wavespeed within the plume, c, is computed numerically from N^2 profiles (no shear) (*Drazin and Reid*, 2004).

While somewhat arbitrary, our definition of h is used for the purpose of estimating the vertical scale of tidal-plume fluid, and not for dynamical calculations. Nevertheless, there is general agreement between c and c_{2l} (c_{2l} is systematically biased 10% high; see Figure 2.9d) supporting h as an appropriate measure of plume thickness. c is used throughout the remainder of this work for dynamical interpretations.

As discussed in §2.3.2, the flow interacts strongly with the bottom over the shallow bar region where $d < L_m/3$ (Figure 2.9a). Sudden increases in h (Figure 2.9b) inshore of b are caused by the sudden arrival of buoyant fluid from upstream. However, this only weakly influences c and c_{2l} because these variables depend more strongly on d than h (Figure 2.9d). As the water depth increases offshore of this region ($x < b$) wavespeeds increase (d) and the plume no longer interacts with the bottom ($h \ll d$).

Offshore of b, plumes aug09b, aug21a and aug25b thinned monotonically from $h \approx 10$m (17m for aug21a) at $x \approx -10$km to $h \approx 5$m by $x \approx -20$km (Figure 2.9b). Plumes aug22a and aug22b deviate from this monotonic pattern by thickening briefly near $x \approx -17$ and -20km, respectively. Plume aug21b was observed to thicken dramatically near $x = -18$km, the details of which are explored in section 2.4.3.

Intriguingly, $\Delta\rho$ tended to increase between $x = b$ and -20km (Figure 2.9c). Since large x_f corresponds to later time, this result indicates that the ratio of advective buoyancy flux (supplied from upstream) to turbulent buoyancy flux (out of the plume, across its base) increases as time evolves. Considering that turbulent flux (integrated along the plume base) is unlikely to decrease as the plume expands and thins, the increase of $\Delta\rho$ offshore indicates that buoyancy supplied from upstream increases with time (consistent with (*Nash et al.*, 2009, Figure 8c)). This strongly contrasts the expected composition of a steady-state river discharge, where entrainment must act to reduce plume $\Delta\rho$ with distance from the source, and highlights the importance of the time dependent discharge strength and composition to plume evolution.

While there is considerable ebb-to-ebb variability in both h and $\Delta\rho$ (figures 2.9b,c), these combine to produce plumes with remarkably consistent patterns of wavespeed, $c(x_f)$. Thicker plumes were generally associated with reduced $\Delta\rho$, so that c remained constant. This is consistent with h and $\Delta\rho$ variability being dominated by mixing, and is further supported by the fact that the thickest plumes occurred during spring tides, consistent with enhanced upstream mixing during

these periods (*Nash et al.*, 2009).

The plume Froude number ($F_p = u_p/c$, where u_p is the mean velocity within plume fluid behind the front ($0 > z > -h$); Figure 2.9e) is a measure of flow criticality within the plume waters. Near $x = b$, F_p is highly supercritical, due to a combination of strong plume velocities and weak c during the initial phase of the ebb. This suggests that information (i.e., from the plume front) is unable to propagate up-estuary past the bar. Further offshore, the flow is approximately critical ($F_p = 1$).

To summarize, the temporal increases in density combine with reduced h to produce a region of frontal propagation with remarkably constant c ($5 - 10$km offshore of the bar). Only offshore of ≈ -15km do h and $\Delta\rho$ decrease together, leading to reduced c and c_{2l}. This reduction in c is attributed to plume thinning which we propose is linked to shutoff of the river discharge as ebb ends (section 2.5.3).

2.4.3 Front speed

We define the front's propagation speed,

$$U_f = U_f^* - u_a \qquad , \tag{2.9}$$

relative to the motion of the ambient fluid u_a (Figure 2.10a) through which it propagates (*Benjamin*, 1968; *Simpson*, 1982). Relative front speeds (Figure 2.10b)

generally exhibit less inter-ebb variability than U_f^* (Figure 2.8b). We compute u_a as the front-normal surface velocity 0.2 to 1.5km offshore of the lead disturbance and averaged over the plume thickness ($0 > z > \langle -h \rangle$).

Due to flow complexities, reliable estimates of u_a were not obtained over the bar ($x > b$), in some complex fronts (aug21a and aug22a), and when the ship did not transit offshore of the lead disturbance. In these cases, we assume $u_a = 0$ and plot U_f and F as open symbols (Figures 2.10b,c). We believe this to be reasonable considering that u_a was generally small compared with U_f^* (except during ebb aug21b). At $x \approx -11$km, during ebb aug21b, because the flow structure ahead of the front was complex over a large region ahead of the front, this u_a estimate is likely to be an overestimate of that quantity. In this instance we assign a subjective lower-bound (0.3m/s) that accounts for the notably high variability of the flow ahead of this front at this location.

Offshore of b, all fronts begin with $0.8 < U_f < 1.1$m/s. Fronts generated during greater ebbs maintain $U_f > 0.7$m/s to $x \approx -20$km before decelerating; during lesser ebbs (aug21a, aug22a) fronts decelerate farther inshore (at $x \approx -10$ to -15km). Plots of U_f versus t (not shown) are roughly linear, indicating that once deceleration begins it is constant. This is not inconsistent with the result of *McCabe et al.* (2008), in which drifter velocities released during max ebb show initially large, followed by weaker, deceleration. Front and drifter speeds are very different quantities. Drifters were released inshore of the front and decelerated rapidly prior to reaching the front. After reaching the front, a major component of drifter speed was along-front and therefore obscures front deceleration.

One front strongly influenced by u_a was aug21b, which was the largest ebb sampled. It initially emerged in the presence of a strong offshore flow (near $x = -11$km), then encountered a strong onshore flow near $x = -19$km. Farther offshore the ambient velocity dropped to zero ($x = -24$km) and reversed to offshore again ($x = -23$km). Figure 2.10b shows that when this ambient velocity is accounted for, the evolution of ebb aug21b's front speed is similar to other fronts. This indicates that the earth-frame deceleration of that front near $x = -18$km (Figure 2.8b) is due to the strong onshore current (Figure 2.10a) that opposed the front's propagation. In the presence of this retarding u_a, and with the estuary discharge continuing to feed into it, the plume was forced to thicken (Figure 2.9b) through conservation of mass. Note also that front aug21b's $\Delta\rho$ was less than any other sampled, suggesting that enhanced mixing both within the plume and in the upstream estuary (*Nash et al.*, 2009) play some role in its thickness, since it was the strongest spring tide sampled. At $x \approx -24$km the onshore flow stopped and the plume thinned abruptly to < 5m. The evolution of u_a (Figure 2.10a) and h (Figure 2.9b) suggest that front aug22b may undergo a similar, though weaker, process.

Because we're concerned with rates of frontal propagation we define the frontal Froude number,

$$F = \frac{U_f}{\langle c \rangle} \quad , \tag{2.10}$$

with respect to the wavespeed, c, within the plume (*Benjamin*, 1968). This contrasts the definition used by *Nash and Moum* (2005) and *Stashchuk and Vlasenko*

(2009) who showed that a Froude number based on wavespeeds ahead of the front indicates whether internal waves were released from the front. Though poorly defined over the bar region (due to ambiguity in u_a and small c), F is initially (out to $x_f \approx -15$km) in the range $1 < F < \sqrt{2}$. This range suggests that the front is propagating as an inertial gravity current (*Benjamin*, 1968; *Britter and Simpson*, 1978; *Marmorino and Trump*, 2000; *Shin et al.*, 2004) and therefore that plume c controls U_f. As the fronts move offshore and weakens, F drops below 1, suggesting that the fronts motion is no longer driven by inertia-gravity balance (*Simpson*, 1982).

The ratio of F_p (Figure 2.9e) to F (Figure 2.10), which is equivalent to u_p/U_f, is larger near and over the bar than farther offshore ($x \approx b$), indicating that fluid supply to the front exceeds its propagation speed. This provides evidence for mixing and the rotor-like frontal circulation patterns described by LI87. Further from the bar this ratio approaches unity, possibly suggesting a decay in frontal turbulence further from the bar, consistent with the observed decrease in dissipation rate as the fronts decay (Figures 2.5 and 2.6).

2.4.4 Front curvature and virtual origin

Following LI87, we estimate the front's radius, R, and center (virtual origin), $(x_\circ, y_\circ)$, of curvature. These were computed using circle fits (*Gander et al.*, 1994) to traces of front position from the radar (Figure 2.11, inset). In order to reduce noise inherent in fitting a circle to an arc, a 1hour running-median filter was applied

to these estimates. Figure 2.11 shows $x_\circ$ and R, of five fronts as they propagated offshore. Fronts aug21a and aug22a have been excluded because the radar did not resolve the evolution of their curvature (see §2.3.1). The virtual origin of most fronts was close to the x-axis ($y_\circ \ll R$) and so we have not plotted $y_\circ$ here; aug25b is an exception with $y_\circ = O(-10\text{km})$.

We identify two phases of front curvature evolution. During the initial "translation" phase, the virtual-origin moved offshore from $x_\circ = 0$ to roughly -8km at approximately 0.7 m/s, while R increased from 3 to 7km at a rate of approximately 0.3 m/s. In the second "spreading" phase, the virtual origin is fixed near $x_\circ = -8$km (-11km for aug09b) and $dR/dt \approx 0.5 - 1.0$m/s is roughly equal to U_f^* (Figure 2.8) so that R increases one-to-one with x_f. These results are consistent with the model results of *Hetland and MacDonald* (2008), in which plume spreading was shown to increase with distance from the mouth of the Merrimack River.

The spatial evolution of the Columbia River plume's expansion differs from the smaller-scale plume described by LI87. Specifically, LI87 showed that R and $x_\circ$ of the Koombana Bay plume both increased at similar, constant rates (each $\approx 0.11 - 0.16$m/s). In contrast, the Columbia is characterized by an early regime of rapid translation and weak spreading, followed by a period of more rapid radial expansion and slow to nonexistent translation of the plume's virtual origin.

Some of these differences may be attributed to the influence of the Columbia River's shallow bar, which extends to 8 km, approximately the location of the plume's final spreading center. Over the bar, the outflow is constrained by the

bottom (eqn. (2.6) and Figure 2.4), which prevents liftoff and hence free propagation as a gravity current. Instead, the transition to buoyant plume dynamics is delayed to the end of the bar ($x = b$), at which point approximately radial spreading occurs. Unlike LI87, the spreading center does not move offshore at this time because the bar becomes the transition point and source for the radially-spreading plume.

2.4.5 Estuary Discharge

In section 2.4.1, we suggested the extent and timing of spatial expansion (Figure 2.8) to be linked to variability in the tidal forcing $\eta(t)$. Following LI87 and *Chen* (1980), we anticipate these dynamics to be related to the time dependence of the estuary discharge, $Q(t)$. ADCP derived velocity from north-south transects across the river mouth at $x \approx -5$km (lines 0 and 1 in Figure 2.1) were used to estimate estuary discharge,

$$Q = -\iint u(y, z, t)\, \mathrm{d}y\, \mathrm{d}z \qquad , \tag{2.11}$$

at each transect's mean time. Note that these transects occurred during different time periods than our front experiments (Figure 2.2), so we are unable to determine $Q(t)$ for the ebbs discussed so far. Instead, we use $Q(t)$ to understand the temporal evolution of the forcing, and how it varies with $\eta(t)$, which can be quantified for all time periods.

During the period of increasing ebb flow ($-6 < t < -1$hours) Q increases linearly in time (Figure 2.12), similar to the result of LI87's discharge from Leschenault Estuary. $Q(t)$ peaks near $t = -1$hours, then sharply decreases as the ebb weakens; this evolution is non-sinusoidal. At $t = 2$hours $Q = 0$ after which the volume flux is into the estuary (negative Q) for the remainder of the tidal cycle.

Straight line fits through the period of increasing ebb flow (Figure 2.12),

$$Q_{fit}(t) = \dot{q}(t - t_Q) \qquad , \tag{2.12}$$

were used to estimate the volume flux rate of change, $\dot{q}$, and onset time, t_Q, of offshore flow at $x \approx -5$km. $\dot{q} = 4.8 \pm 0.3\text{m}^3/\text{s}^2$ for all ebbs except aug12b during which $\dot{q} = 3.6\text{m}^3/\text{s}^2$ (Figure 2.12).

We initially believed that the time that the front crossed $x = b = -8$km (t_b) and the time of ebb onset (t_Q) would be related to $\Delta\eta_\circ$, but we found these to be only weakly correlated. Instead, t_b and t_Q each show a much stronger correlation with the diurnal inequality (Figure 2.13). Both t_Q and t_b occur earlier for greater ebbs ($\Delta\eta_\circ > \Delta\eta_{-1}$). The similar magnitude of the dependence of these variables on $\Delta\eta_\circ - \Delta\eta_{-1}$ indicates that earlier ebbs – caused by larger tides – create fronts that emerge earlier. A good explanation why these vary more strongly with $\Delta\eta_\circ - \Delta\eta_{-1}$ than with $\Delta\eta_\circ$ is currently lacking. One possibility is that $\Delta\eta_\circ - \Delta\eta_{-1}$ is a measure of the salt content of the estuary (i.e., the salt influx during the previous flood), and thus affects timing of plume emergence, but this has not been confirmed.

2.5 Plume dynamics

In section 4, we showed that Columbia River tidal plumes expanded with remarkable consistency, despite their complex internal structure. Here we highlight four aspects of the plume system which are important to our generalization of frontal evolution:

1. offshore of the bar ($x < -8$km), plumes propagated with constant U_f for $5 - 10$km during a steady phase, after which U_f decreased slowly during a period of relaxation,

2. spatial patterns in U_f are tracked in c, leading to a constant frontal Froude number F,

3. plume front timing (relative to low tide) was related to the magnitude of the diurnal inequality $\Delta\eta_o - \Delta\eta_{-1}$

4. the tidal discharge near the river mouth $Q(t)$ exhibits a sawtooth evolution, in which it increases approximately linearly in time.

In the following, we combine the above attributes to formulate a model for plume spreading offshore of the bar region. Specifically, we wish to explain why fronts initially propagate with relatively constant U_f. Front deceleration was weakest just after liftoff, then increases farther offshore. This contrasts the results of spreading plume models with steady $Q(t)$ in which front deceleration is highest near the mouth, and decreases offshore (*Garvine*, 1984; *Jay et al.*, 2010).

2.5.1 A time-dependent spreading model

We follow LI87 and use *Chen* (1980)'s kinematic spreading plume model to include the time dependence of the source discharge in interpreting these observations. This contrasts the methodologies used by *Garvine* (1984) and *Jay et al.* (2010) which represent the plume dynamically but implicitly assume a time-invariant discharge. Our goal is to show the spatial dependence of U_f (Figures 2.8c) can be explained by Chen's simple kinematic model when fed by a time-variable discharge, $Q(t)$. For the purposes of this model we assume h can be considered spatially uniform inshore of the front (e.g. isopycnals are roughly horizontal in Figure 2.5B) and that, for a given ebb, $\Delta\rho$ is constant in time and space (Figure 2.9c).

In making these assumptions we suggest that the time-dependence of Q is more important to frontal evolution than mixing across the plume base. This is an alternate approach to several recent studies that suggest mixing is important to plume dynamics, particularly with respect to its influence on lateral spreading (*MacDonald et al.*, 2007; *Hetland and MacDonald*, 2008; *Hetland*, 2010). We justify our approach in two ways: (1) Q exhibits O(1) variability (i.e., from 0 to max(Q)), and (2) we argue that this front propagates in gravity-inertia balance (opposed to gravity-viscous balance, which may be the case for smaller plumes (*Hoult*, 1972; *Chen*, 1980)). The latter point implies, to first order, that frontal propagation is controlled by plume internal wavespeed (*Benjamin*, 1968), which is essentially unaffected by mixing (since $c^2 \propto h\Delta\rho$ remains constant as a layer thickens due to mixing). This assumption has both dynamic consequences, because $c \approx 0.7$m/s is

roughly constant over 10km of frontal propagation (Figure 2.9d), and kinematic consequences, as the vertically-integrated freshwater (and its transport) is also constant in space. Both of these attributes are preserved in our simplified plume geometry. Thus, while mixing is clearly important to the nearfield plume composition (*Nash et al.*, 2009), we propose the basic plume geometry is set by the time-dependent characteristics of the source.

This model begins with a kinematic representation of the plume, which spreads with density $\rho_\circ - \Delta\rho$ as a pie-shaped wedge into a semi-infinite ($d \to \infty$), motionless ambient of density $\rho_\circ$ (Figure 2.14). The thickness, h, angle, θ (in radians), and radius, $R(t)$, give a plume volume,

$$V(t) = \theta h R^2/2 \qquad . \tag{2.13}$$

Direct estimates of θ were not made; for simplicity, we assume $\theta = 2$ ($= 115°$). However, since variables that involve θ are estimates of scale, this choice does not alter interpretation. With the assumption of no entrainment, volume conservation is

$$Q(t) = \frac{\mathrm{d}V}{\mathrm{d}t} \qquad . \tag{2.14}$$

The front velocity is defined as,

$$U_f = \frac{\mathrm{d}R}{\mathrm{d}t} \qquad . \tag{2.15}$$

With $Q(t)$ and $\Delta\rho$ known, h and R are the undetermined variables of interest. As has been pointed out in many previous works (e.g. *Hoult* (1972)), volume conservation alone does not uniquely determine the plume depicted by Figure 2.14. An expression that relates U_f to h is required. Following previous gravity current studies (*Benjamin*, 1968; *Hoult*, 1972; *Chen*, 1980; *Didden and Maxworthy*, 1982; *Garvine*, 1984; *Shin et al.*, 2004), and in agreement with our own results (Figure 2.10c), we employ the frontal Froude number condition,

$$F_{2l} = \frac{U_f}{c_{2l}} = \text{Constant} \qquad . \tag{2.16}$$

In this model, in which we assume $d \to \infty$ (no bottom interaction), (2.8) becomes $c_{2l} = \sqrt{g'h}$.

Combining (2.13) with this frontal condition, employing (2.14), (2.15) and assuming that front acceleration is small ($dU_f/dt \ll U_f^2/R$), it is straightforward to show that,

$$U_f = F_{2l}c_{2l} = \left(\frac{F_{2l}^2 Q' g'}{t}\right)^{1/4} \qquad . \tag{2.17}$$

Here $Q' = Q/\theta$ is the per-radian volume source flux. U_f ($\propto c_{2l}$) and h are fully determined by $Q(t)$ according to (2.17), as originally derived by *Chen* (1980) (also (*Didden and Maxworthy*, 1982)).

2.5.2 Two limits of model U_f

Based on the observed time evolution of estuary discharge (Figure 2.12), we explore two limits of (2.17). In the first limit, we assume $Q'(t)$ increases linearly in time, $Q'(t) = \dot{q}'t$, where $\dot{q}'$ is a constant. This is consistent with the observed behavior of $Q(t)$ over the period of increasing ebb flow ($-5 < t < -1$hours). In this limit (which was also considered by LI87) the time dependence of (2.17) disappears so that

$$U_f = F_{2l}c_{2l} \approx (F_{2l}^2 g' \dot{q}')^{1/4} \qquad . \tag{2.18}$$

Thus, within the framework of this model, U_f = constant is a consequence of linearly increasing $Q(t)$.

During the second half of ebb, Q was found to abruptly decrease (Figure 2.12). As an approximation to this, we consider a second limit to (2.17) in which $Q = 0$, corresponding to the spreading of a fixed volume V of buoyant fluid. In this limit, we may rewrite (2.17) in terms of $V' = V/\theta$ to yield

$$U_f = F_{2l}c_{2l} \approx F_{2l}(V'g')^{1/2}R^{-1} \qquad . \tag{2.19}$$

Hence, $U_f \propto 1/R$ for a fixed volume of fluid ($Q = 0$).

Based on the above limits, we expect $U_f \propto \mathrm{d}Q/\mathrm{d}t$ = constant during the period of linearly increasing ebb flow. After Q ceases to increase, we expect U_f to decrease in space, scaling like $1/R$, with this decay set by $\int Q dt$. We use the observed $Q(t)$

to explore these limits in the following sections.

2.5.3 Plume size and front timing

The length scale L_{tidal} separating the two anticipated limits of (2.17) depends on the evolution of $Q(t)$ and its integral $V_{\text{tidal}} = \int_{\text{ebb}} Q\,\mathrm{d}t$ over the period of positive ebb discharge, such that

$$L_{\text{tidal}} = \sqrt{\frac{2V_{\text{tidal}}}{\theta h}} \qquad . \tag{2.20}$$

Because the ebbs in Figure 2.12 are not the same as those that were front-tracked, we parameterize V_{tidal} in terms of $\Delta\eta_\circ$. However, our sampling did not resolve a large dynamic range of $\Delta\eta_\circ$ so we use ROMS model output of the Columbia River estuary and near-field to parametrize V_{tidal} in terms of $\Delta\eta_\circ$ (*MacCready et al.*, 2002). A linear fit of model V_{tidal} (from model Q through line 0) to model $\Delta\eta_\circ$ (at 124.126W,46.24N) produces the empirical relationship,

$$V_{\text{tidal}} = \left(3.2\text{m}^{-1}\Delta\eta_\circ + 1.9\right) 10^8\text{m}^3 \qquad . \tag{2.21}$$

This relationship explains 91% of the variance in model V_{tidal} over a range of $\Delta\eta_\circ$ from 0.25 to 3.3m. It also holds for estimates of V_{tidal} based on observed $Q(t)$ (Figure 2.12)

In order to isolate the influence of V_{tidal} on L_{tidal} in (2.20), $h = 8$m was used for all fronts. This methodology produced estimates of L_{tidal} that ranged from 8.2km

(aug25b) to 11.6km (aug21b).

Section 2.4.4 indicates that the spreading origin can be considered stationary near $x = b$. For convenience, we define front position offshore of this,

$$r_f = b - x_f \qquad . \tag{2.22}$$

Because x_f is the intersection of the front with $y = 0$, r_f may be considered a radial coordinate from the plume's presumed spreading center at $(x, y) = (b, 0)$. Throughout the remainder of this work $b = -8$km except during ebb aug09b during which $b = -11$km.

When front timing is non-dimensionalized as $(t - t_b)c_\circ/L_{\text{tidal}}$ and position as r_f/L_{tidal}, front timing versus position curves are similar for all fronts (Figure 2.15). Here, $c_\circ$ is the mean value of $\langle c \rangle$ in the range $-20 < x_f < -10$km for each front. The slope of the best fit (black line) to the data between $0 < r_f < L_{\text{tidal}}$ is the Froude number, $U_f/c_\circ \approx \sqrt{2}$.

Inshore of the bar ($r_f < 0$) several fronts propagated slowly (i.e., aug21a and aug22a), which we attribute to interaction with the bottom. Further offshore, linear and similar trajectories during the "steady" stage indicate that fronts are propagating with constant U_f and similar F. Frontal deceleration near $r_f/L_{\text{tidal}} = 1$ (where the plume volume reaches V_{tidal}) indicates the beginning of the "relaxation" stage. The fact that this deceleration occurs as the plume reaches its maximum volume indicates that the evolution of U_f is closely tied to $Q(t)$.

As fronts aug21b, aug22b and aug25b decelerate near $r_f/L_{\text{tidal}} = 1$, they radiate

NLIWs. This indicates that the deceleration which brings about NLIW radiation (*Nash and Moum*, 2005), occurs as the estuary discharge subsides and the plume volume approaches V_{tidal}. This suggests that the location of NLIW radiation may occur at the scale of the total estuary discharge, L_{tidal}, in other tidal plume systems as well. Note that internal waves were also generated near the bar region during aug21a, aug22a (not shown).

2.5.4 Steady propagation

During the steady stage of propagation ($r_f/L_{\text{tidal}} < 1$), U_f reaches a maximum value of 0.9 to 1.1m/s and c is roughly constant at 0.7 ± 0.1m/s (Figure 2.16a,b). Combining the observed value of $\dot{q}' = \dot{q}/\theta = 2.5\text{m}^3/\text{s}^2$ (§2.4.5) with $g' = 0.07\text{m}/\text{s}^2$ and assuming $F_{2l} = \sqrt{2}$ gives $U_f \approx 0.8$ and $c_{2l} \approx 0.6$ (Figures 2.16a,b, $r_f < L_{\text{tidal}}$, black lines). Considering the highly idealized geometry (Figure 2.14), the level of approximation associated with (2.17) and the error in estimates of $\dot{q}$, the agreement of these values to observed initial speeds is reasonable. This suggests that the linear increase in $Q(t)$ forces the relatively constant (i.e. "steady") U_f and c observed between $0 < r_f/L_{\text{tidal}} < 1$ (Figure 2.16a,b). Note also that fronts expand nearly radially through the latter half of the steady stage (Figure 2.16d). Agreement between front curvature data and the black $r_f = R$ line in Figure 2.16d indicates that these fronts are spreading from a roughly fixed virtual origin near $(x, y) = (b, 0)$. The better agreement of the red dots, compared to the thin red line, with the black line indicates that $b = -11$km is appropriate for front aug09b.

2.5.5 Relaxation and geostrophic adjustment

As ebb ends and the estuary discharge weakens, the relaxation stage ($r_f/L_{\text{tidal}} > 1$) begins. c decreases during this period as the plume continues to spread and thin. The evolution of U_f mirrors c, consistent with roughly constant F. This is consistent with (2.19), in which U_f and c decrease like R^{-1} as the fixed volume thins due to spreading (black curve, $r_f > L_{\text{tidal}}$, Figure 2.16).

Eventually, offshore of $r_f/L_{\text{tidal}} = 1$, R approaches a limiting value of 1.1 to $1.5L_{\text{tidal}}$. At first glance this might suggest that L_{tidal} is not only the significant scale for plume front expansion, but also its final curvature. However, though *Chen* (1980)'s theory predicts that the front will decelerate, it allows the plume to thin and expand indefinitely (Figure 2.16d, black line). With this in mind, we propose that the plume's expansion is limited by the Rossby radius,

$$L_{\text{R}} = \frac{c}{f} \qquad , \tag{2.23}$$

where f is the Coriolis parameter. Taking $c \approx 0.7$m/s gives $L_{\text{R}} \approx 7$km. This value is remarkably similar to $L_{\text{tidal}} \approx 10$km. This suggests that as the plume volume approaches V_{tidal} its dynamics are increasingly influenced by the Earth's rotation. As fluid parcels are deflected to the right surface convergence at the front will decrease. This being the case the plume front loses its buoyancy supply and will thin and decelerate. This suggests that the Coriolis effect is a second mechanism for frontal deceleration.

The similarity between L_{tidal} and L_{R} is not a coincidence. Rewriting L_{tidal} in

terms of the timescale of the estuary discharge, $\Delta t = (V_{\text{tidal}}/\dot{q})^{1/2}$, gives $L_{\text{tidal}} = Fc\Delta t$. Therefore the ratio of L_{tidal} to L_{R} is $F\Delta t/f$, which is independent of c. Instead, it is simply a ratio of the estuary (tidal) timescale, $\Delta t = O(6\text{hours})$, to the inertial timescale, $1/f = O(4\text{hours})$, which depends only on latitude. Thus, for mid- and high-latitude river plumes, we expect $L_{\text{tidal}}/L_{\text{R}}$ to be $O(1)$.

Ungarish and Huppert (1998) consider the effect of rotation on a finite volume lock release. The initial radius of the released fluid (stationary in the rotating frame) is $r_\circ$ and its initial Rossby radius is L_{R}. They find the radius of the "steady lens" solution to be,

$$r_{\text{SL}} = r_\circ \left(1 + L_{\text{R}}/r_\circ\right) \qquad . \tag{2.24}$$

Yankovsky and Chapman (1997) formulate a similar theory, but for a buoyant discharge with initial Froude number $F_\circ$ rather than a lock release, and find the steady lens solution,

$$r_{\text{SL}} = L_{\text{R}} \frac{3 + F_\circ^2}{\left(2 + F_\circ^2\right)^{1/2}} \qquad . \tag{2.25}$$

If we assume $L_{\text{tidal}} \approx 10\text{km}$ to be a good approximation of $r_\circ$, and $F_\circ \approx 2$ (Figure 2.9e, near $x = b$) then (2.24) and (2.25) give $r_{\text{SL}} \approx 17$ and 20km, respectively.

Agreement between these predictions of r_{SL} and the observed maximum radius of curvature, $R_{max} \approx 1.4 L_{\text{tidal}} \approx 14\text{km}$, suggests that the final expansion of the plume is influenced by the earth's rotation. This being the case, this fluid has become a part of the "bulge" circulation (*Horner-Devine*, 2009) or one of the

other far-field plume regimes (*Yankovsky and Chapman*, 1997; *Hickey et al.*, 2005), depending on wind conditions.

We therefore propose that the front's deceleration is driven by both the limited plume volume, V_{tidal}, and the effect of rotation. The former is likely to play a larger role as the front begins to decelerate and the latter apparently sets R_{max}. These results are consistent with *McCabe et al.* (2009)'s numerical model results, in which the plume momentum balance is initially dominated by advective and pressure gradient terms, but eventually the Coriolis effect causes plume water to turn anticyclonically. While we expect these results are generally applicable to other tidal plume systems large enough to be considered inviscid, for systems with smaller river discharge it is possible that mixing will play a larger role in the tidal plume's dynamics (*Hetland*, 2010).

2.6 Conclusions

The internal structure and three-dimensional expansion of tidal plume fronts that formed near the Columbia River mouth have been presented. Of seven fronts explored in detail, only two propagated as a single uncomplicated front (i.e., figures 2.4 and 2.5), similar to that of a classical gravity current flowing through an unstratified or uniformly stratified fluid (i.e., LI87, *Britter and Simpson*, 1978; *Garvine and Monk*, 1974; *Marmorino and Trump*, 2000)]. Instead, the majority of plumes had complex, non-classical internal structures that produced multiple fronts (Figures 2.6 and 2.7), similar to those observed by *McClimans* (1978),

Garvine (1984) and LI87, or radiated nonlinear internal waves (NLIWs), as observed by *Nash and Moum* (2005). Close to the river mouth, many fronts formed strong velocity convergences that did not coincide with horizontal density gradients. In many cases, the initial expansion was that of salty, dense fluid colliding with fresher, lighter receiving waters, producing what we term a reverse-front. This complex behavior arises because (1) the estuary has strong temporal variability in both composition ($\rho(t)$) and flow rate $Q(t)$, (2) its discharge is constrained by shallow bathymetry, and (3) freshwater plume remnants are common in the vicinity of the river mouth. This work focuses primarily on the region offshore of the shallow bar ($x < -8$km) where the plume evolves as a freely-propagating gravity current.

Even offshore of the bar, plume remnants from previous tidal cycles produce regions with strong horizontal variability in stratification through which new plume waters propagate. This remnant fluid more readily supports NLIW radiation (i.e., as modeled by *Stashchuk and Vlasenko*, 2009) because internal wavespeeds and plume front propagation speeds are more similar. Five of seven fronts supported NLIWs that propagated at a similar speed to, and offshore of, the primary front. One example exhibited a secondary front within the plume itself.

Regardless of the internal complexity of the fronts, the intrinsic wavespeed, c, and propagation speed, U_f, (relative to the ambient) had surprisingly similar spatial structure offshore of the bar, consistent from front to front (Figures 2.10b, 2.9d). Because these variables co-vary, their ratio, F, is roughly constant and in the range $1 < F < \sqrt{2}$ (Figure 2.10c), consistent with that expected for gravity current flows (*Shin et al.*, 2004; *Didden and Maxworthy*, 1982; *Marmorino et al.*,

2004) and observed by LI87. This provides strong additional support for the use of front condition (2.16) as a constraint to predict the relationship between U_f and c as the plume expands (i.e. LI87; *Chen*, 1980; *Garvine*, 1984).

We have identified 3 periods of distinct dynamics that affect frontal evolution $U_f(t)$ (characterized in Figure 2.15),

- Bottom-interaction: as the plume emerges, it is initially strongly influenced by the shallow bar and is connected to the bottom over its first $\approx$ 8km (i.e., $d < L_M/3$, equation (2.6); *Jones et al.*, 2007),

- Steady phase: offshore of liftoff, the front propagates freely as a gravity current with constant U_f; timing of plume front emergence scales with the diurnal inequality.

- Relaxation: as ebb weakens, U_f decays. The location of deceleration is controlled by the total discharge volume V_{tidal} of each ebb, which sets the length scale L_{tidal} at which frontal deceleration occurs. L_{tidal} scales with the Rossby radius L_{R}, so that the tendency for the front to decelerate according to (2.19) is reinforced by a transition towards geostrophy.

This classification of the Columbia River plume differs from that in Leschenault Estuary (LI87), which did not contain an extensive bottom-interacting region, nor did their analysis include the relaxation phase. However, in both cases, temporal variability of the estuary volume flux $Q(t)$ appears to control frontal expansion during the steady phase.

Following LI87, we use the kinematic model of *Chen* (1980) to determine the evolution of U_f based on the time variability of Q. Conveniently, $Q(t)$ is observed to increase approximately linearly in time (in the Columbia and Leschenault estuaries). Chen's simplified geometry produces the result that U_f = constant during the linearly increasing discharge period, consistent with our observations. As ebb ends and $Q(t)$ begins to decrease, the plume evolution may be thought of as a spreading fixed volume (V_{tidal}) of buoyant fluid. This also represents a limit of Chen's model, yielding the solution that $U_f \propto 1/R$ in the relaxation phase, which begins at $R \sim L_{\text{tidal}}$.

The similar magnitude of L_{R} and L_{tidal} suggests that as the plume volume approaches V_{tidal} the effect of the earth's rotation begins to play a significant role. Agreement of the plume's final radius of curvature, R_{max}, with simple spreading lens models encourages this idea. These results suggest that the Columbia River tidal plume front is initially driven by the linear increase in $Q(t)$, and as it expands beyond L_{tidal} it spreads like a fixed volume of fluid that becomes increasingly influenced by the earth's rotation.

Our interpretation is fundamentally different from models of *Garvine* (1984) and *Jay et al.* (2010), which more accurately represent plume dynamics, but are limited to steady state applications. Those models typically predict initial front speed to decrease rapidly (strong deceleration) followed by weaker deceleration. In contrast, the model we employ assumes the time-dependence of the source is more important for a radially spreading tidal plume than accurately representing the time variability of $\Delta\rho$ (*Jay et al.*, 2010) or the spatial variability of h (*Garvine*,

1984). Following *Chen* (1980) and LI87, only the dynamics of the plume front are retained. However, the agreement with observed U_f validates these assumptions.

In summary,

1. offshore of the bar, the plume front expands at a constant U_f, which arises because of the time dependence of the estuary discharge flux. During this period, the plume flows as a gravity current with $1 < F < \sqrt{2}$.

2. the ultimate plume extent scales with L_{tidal}. Since L_{tidal} is proportional to L_{R}, this also represents the transition towards geostrophic balance, at which point the front becomes subcritical ($F < 1$);

3. wind forcing alters the three dimensional plume shape and curvature of the plume front (Figure 2.3), but has only secondary effects on U_f.

4. ambient currents alter propagation speed in the Earth's frame; the thickening of front aug21b as it flowed into an onshore current is an instructive example (§2.4.3).

This provides a synoptic understanding of tidal plume front evolution, from liftoff toward geostrophic adjustment, in terms of the time dependent estuary discharge.

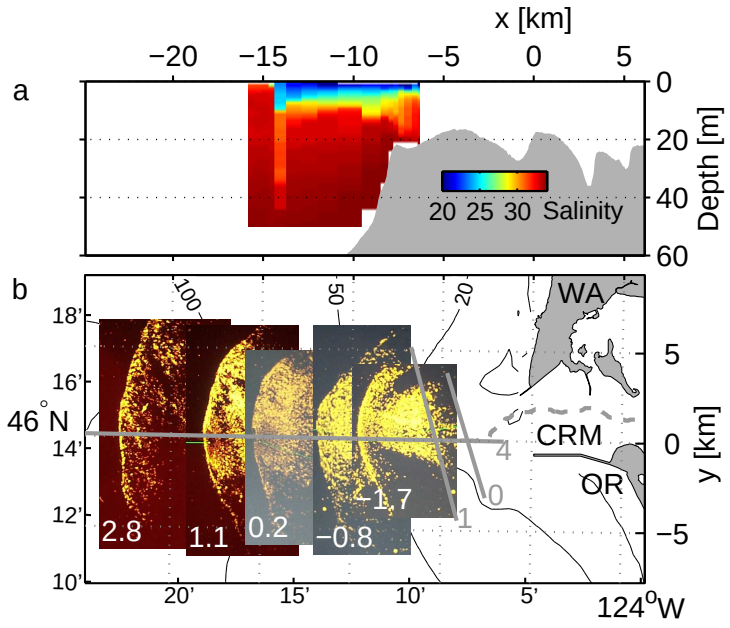

Figure 2.1: Setting at the Columbia River mouth (CRM). (a) Water depth and plume salinity at low tide ($t = 0$) during the second ebb of August 9$^{\text{th}}$ (aug09b). (b) Images of the ship's X-band radar – white numbers indicate time relative to low-tide (t) in hours – show the propagation of the front in (a). Also shown are depth contours (black; m) and transect lines (solid gray); the axes indicate the x, y coordinate system. In (a), water depth follows line 4 for $x < -4$km and the shipping channel (dashed line in (b)) for $x > -4$km.

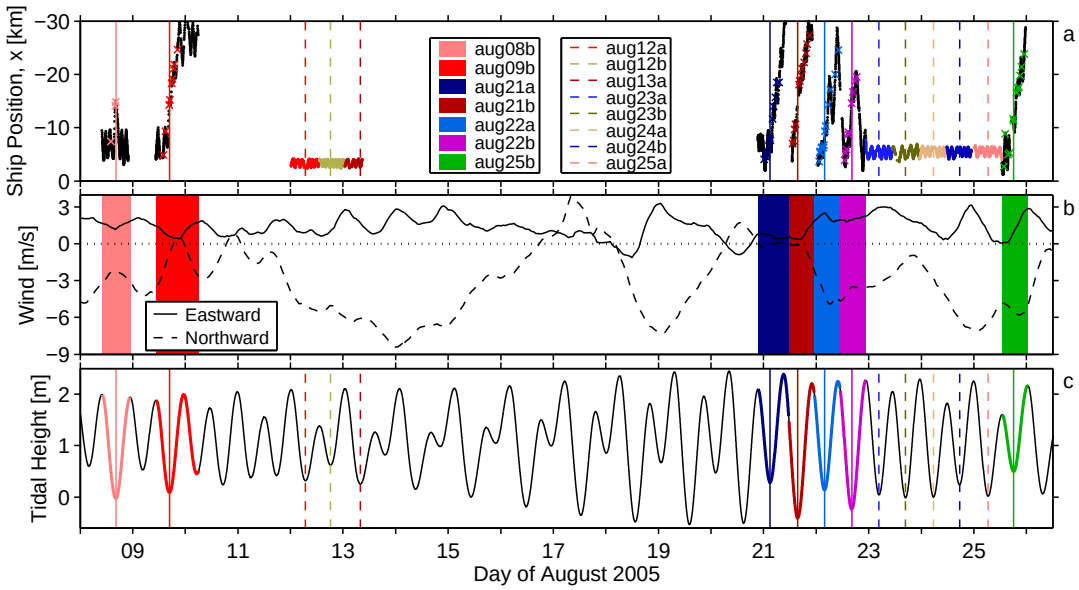

Figure 2.2: (a) Cross-shore location of Chameleon sampling (black) and plume-fronts (color ×'s; left legend). Colored lines represent cross-mouth sampling (right legend). (b) 10-hour low passed wind speed from NDBC buoy 46029 (Columbia River Bar). (c) Tidal height from xtide with time periods of each front tracking experiment in color. Vertical lines in (a) and (c) – solid for front tracking, dashed for cross-mouth sampling – indicate the reference time (t_{low}) of the tidal cycle.

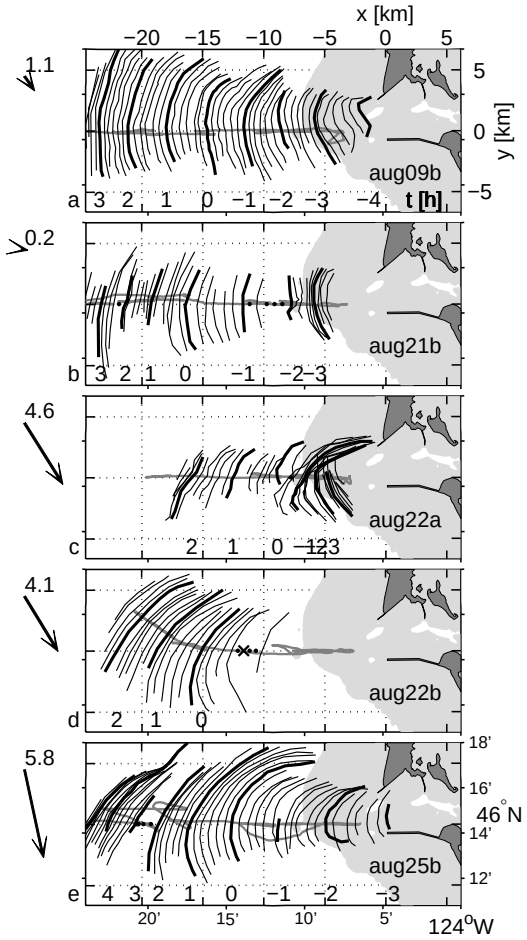

Figure 2.3:
Traces of front location from radar images during five ebbs (ebb ID: lower right corner). Numbers along the bottom of each panel indicate the hour – relative to low-tide (t) – of thick-line traces. Thin lines are traces every ten minutes. Where there are gaps in trace data, missing thin lines are marked by dots and thick lines by $\times$'s. The coordinate system is labeled at upper right (inward ticks, grid). In each panel the coastline is shaded dark and depths shallower than 23m are lightly shaded. A gray line shows the ship's track. Mean wind, during each period, from buoy 46029 is indicated by the arrow at left (numbers indicate magnitude in m/s).

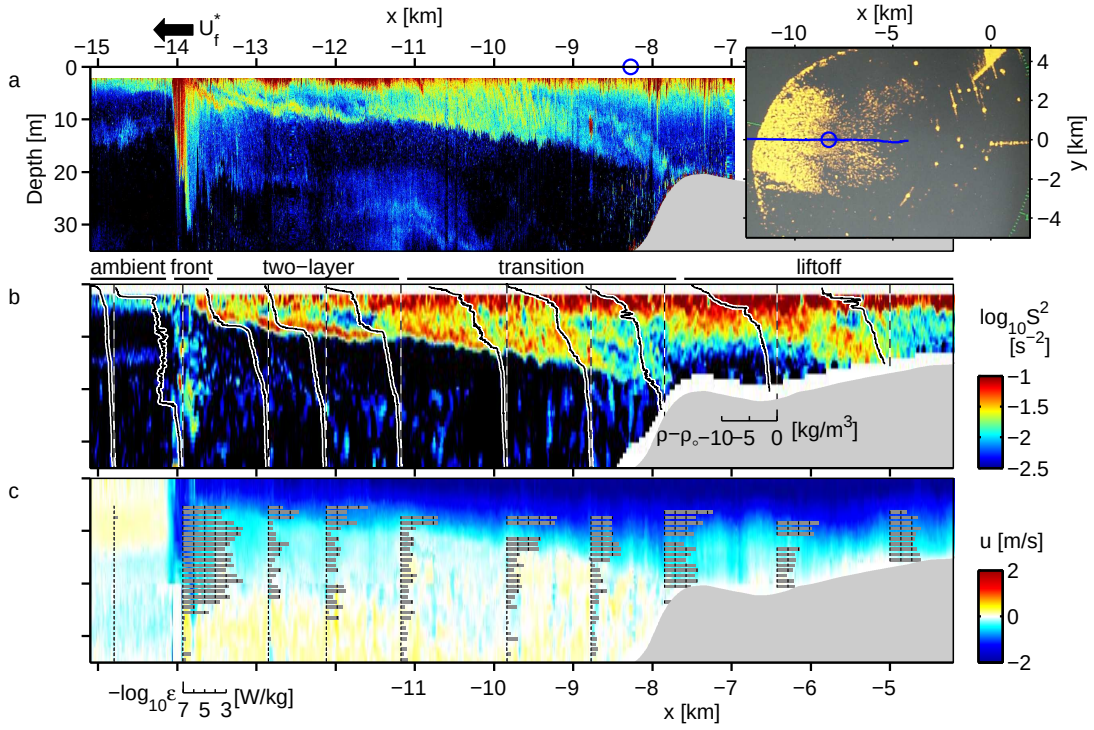

Figure 2.4: Internal plume structure for a moderate ebb near low tide (aug08b; $\Delta\eta_\circ = 2.0$m and $t = -0.3$h at frontal crossing). (a) 120khz acoustic backscatter. (b) Log of shear squared (color) and vertical profiles of density deficit $\rho - \rho_\circ$ (black lines; $\rho_\circ = 1026.3\text{kg/m}^3$). (c) Eastward velocity (color) and $\log_{10}\epsilon$ (gray bars; ticks indicate decades above 10^{-7}W/kg). Roughly 1 in 5 vertical profiles are shown. An X-band radar image (inset) shows plume extent when the ship was at $x = -8.3$km (circle); blue line indicates ship track. This transect was acquired over the one hour period 15:08-16:10 08-August-2005 as the ship traveled west at 6 knots.

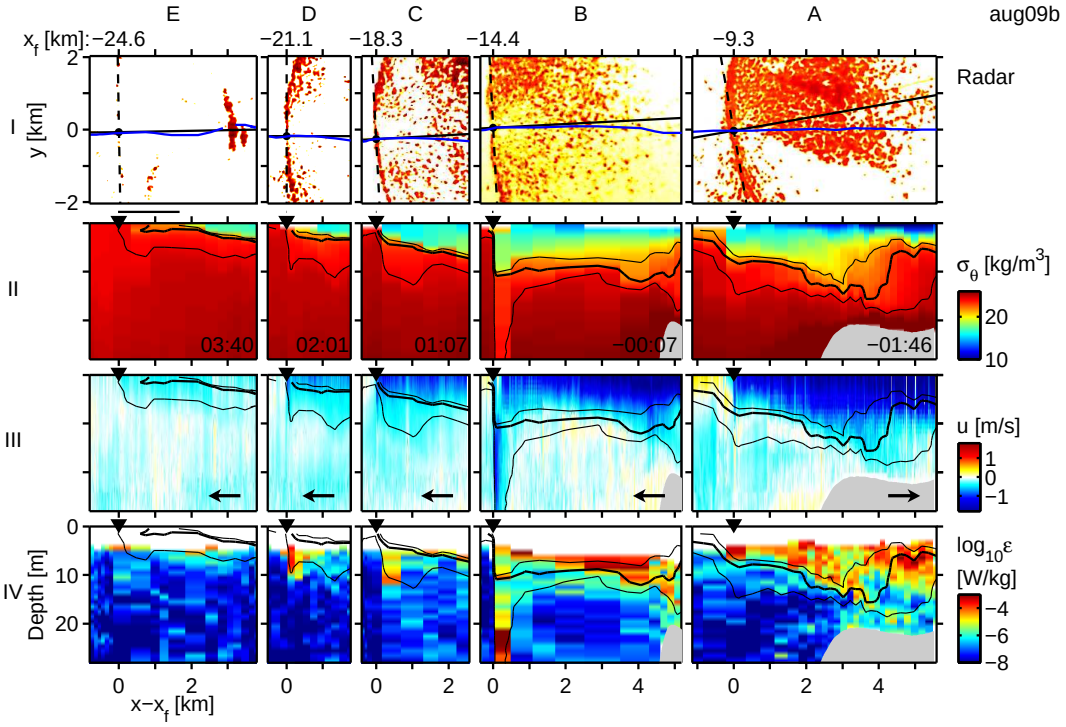

Figure 2.5: A time sequence of east/west transects along line 4 through the front generated during the second ebb of August 9$^{\text{th}}$ (aug09b). Columns are in reverse chronological order and move progressively offshore from right to left. Horizontal axes have been corrected for Doppler shifting, so preserve distance relative to the moving front (but distort distances relative to topography). I) Radar image intensity, cross-hairs indicate front orientation. The blue line indicates the ship's track. II) Potential density. III) Eastward velocity. Arrow: direction of ship travel. IV) TKE dissipation. Front location, x_f, and time, t, of frontal crossing (relative to low tide) are indicated in I and II. In rows II, III, and IV, the 28, 30 (thick) and 32 salinity contours are shown. Black triangles and line segments (above triangles in II) indicate frontal location and its position ambiguity.

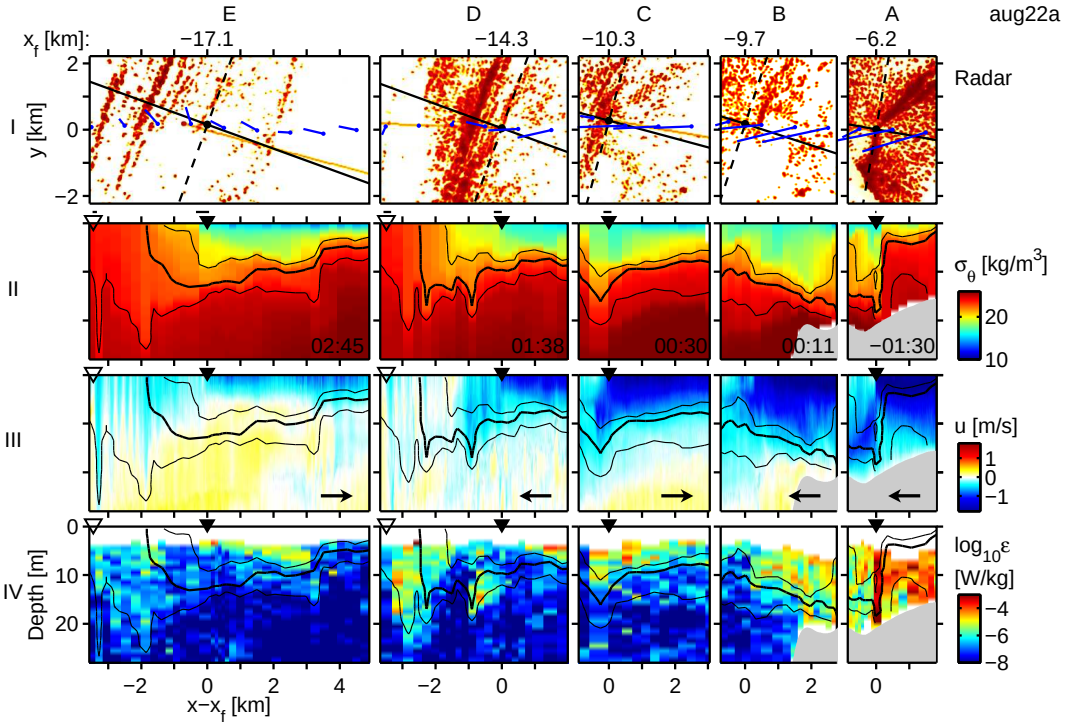

Figure 2.6: Transects across front aug22a. Blue surface velocity arrows are plotted over the radar images (1km = 1m/s). An open triangle marks the location of the lead wave in a NLIW train. All other panels and notation are as in Figure 2.5.

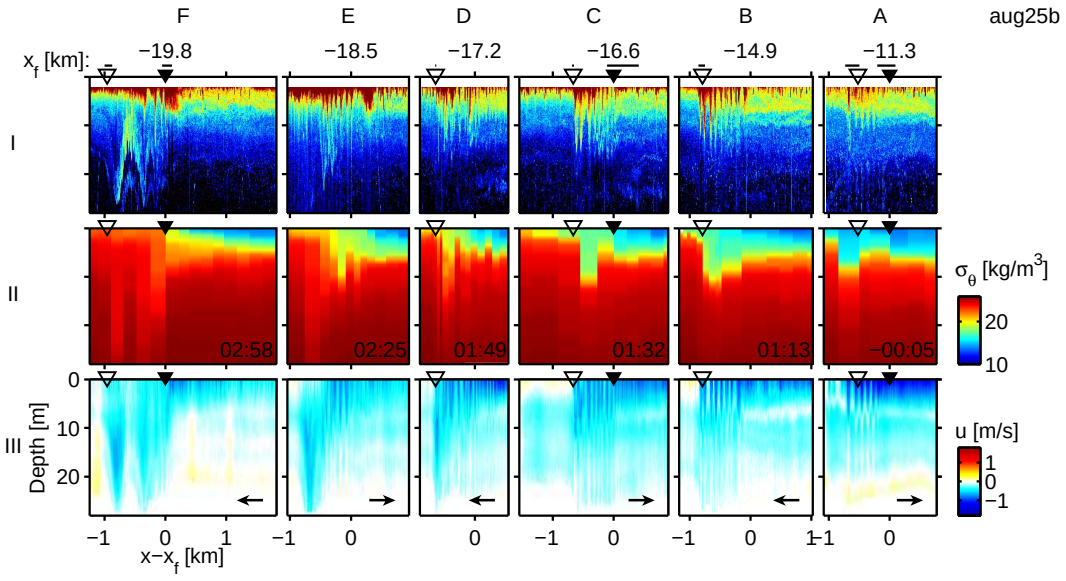

Figure 2.7: Transects across front aug25b. I) Log of acoustic backscatter from the 120kHz Biosonics^{TM} echosounder. Front position ambiguity is indicated above this panel. Density contours have been excluded. All other panels and notation are as in Figure 2.6.

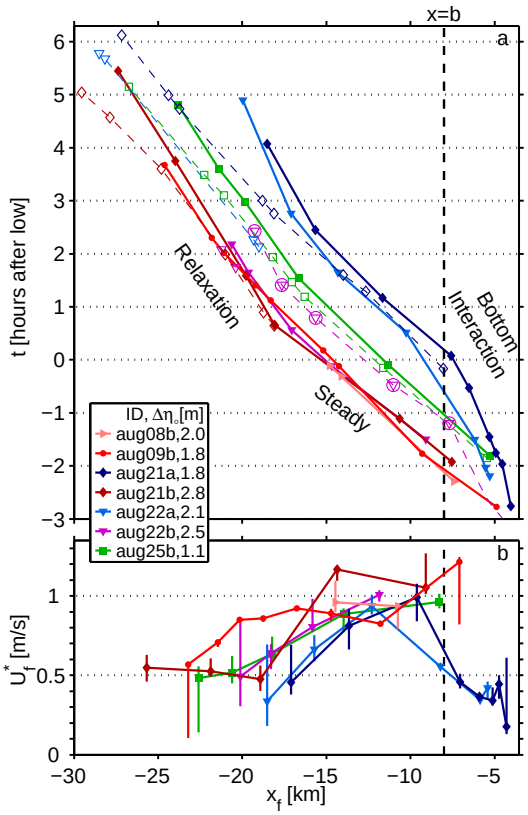

Figure 2.8: (a) Position, x_f and (b) speed U_f^* (with error bars) for seven fronts. Solid lines and filled symbols indicate primary fronts; dashed lines and open symbols indicate the lead wave of the farthest offshore disturbance (NLIW) captured. One exception is the magenta dashed line with open circles and triangles that marks a secondary disturbance that trailed behind the primary aug22b front. A vertical dashed line at $b \equiv -8$km marks the end of the shallow bar region (30m isobath).

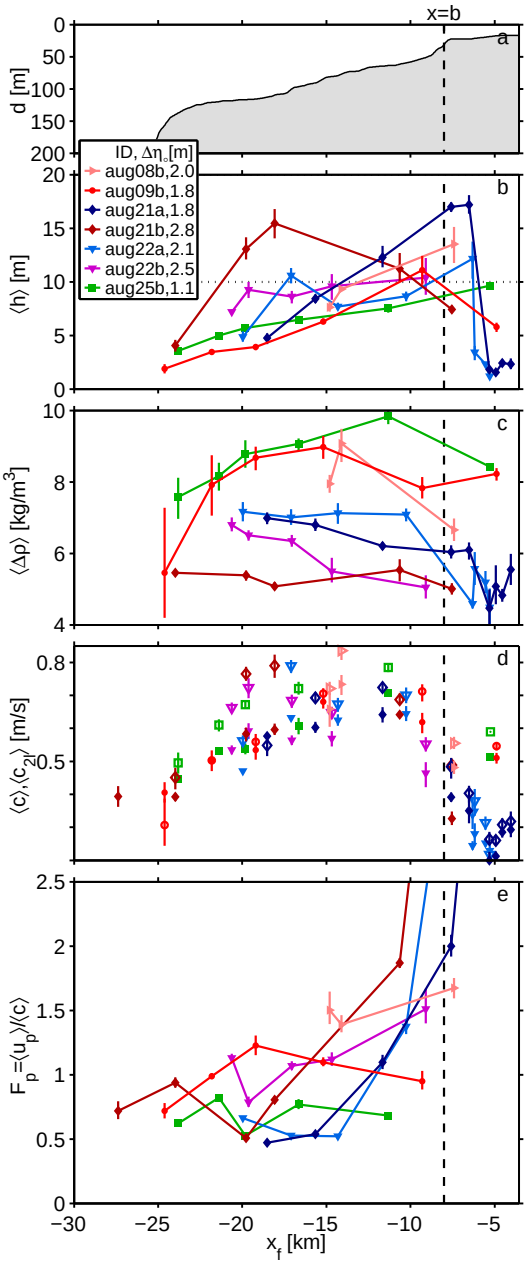

Figure 2.9: Spatial structure of plume properties behind the primary front. (a) Water depth, (b) plume thickness, h (c) density anomaly, $\Delta\rho$, and (d) two-layer c_{2l} (open symbols) and 1st-mode wavespeed, c, (filled symbols). (e) Plume Froude number F_p based on the local fluid velocity. $\langle\ \rangle$ denotes an ensemble average of profiles 0.5 to 3km inshore of the front and are plotted versus the corresponding front location x_f. Error bars represent 95% bootstraps of each ensemble mean.

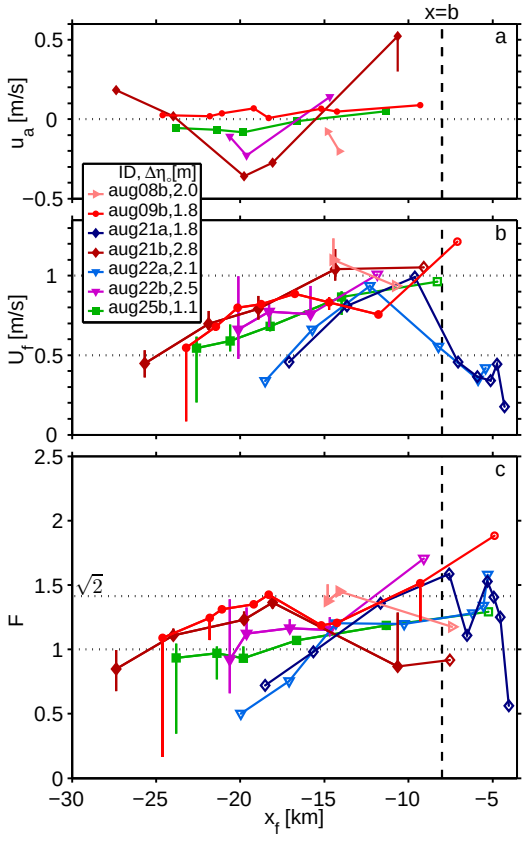

Figure 2.10: a) Cross-front ambient velocity, u_a (negative opposes front motion), b) Primary front speed relative to the fluid ahead of it, U_f, with error bars. c) Frontal Froude number. Open symbols are used for points in which we assume $u_a = 0$ and error bars could not be estimated.

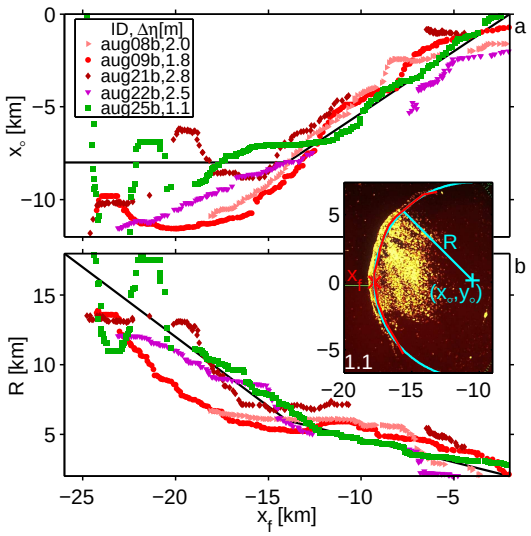

Figure 2.11: Front virtual origin, $x_\circ$, and radius, R, vs. plume front position x_f for five fronts. An inset radar image, 1.1hours after low tide aug09b, shows an example trace of front position (red line) and circle fit (cyan), all shifted to the right by 0.3km. x_f, the point where the front crosses the x axis, is marked by a red x. The fit variables, $(x_\circ, y_\circ)$, R are labeled. The solid black line is a schematic representation of the data; see text for details.

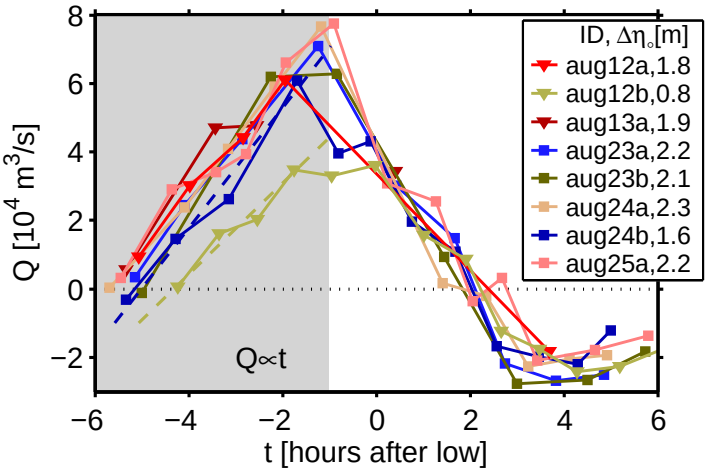

Figure 2.12: Tidal discharge Q as a function of t for eight ebbs (color). Triangles are from data collected along line 0, and squares from line 1 (Figure 2.1). Dashed lines are example linear fits over the period of increasing ebb flow (shaded region) for ebbs aug12b and aug24b.

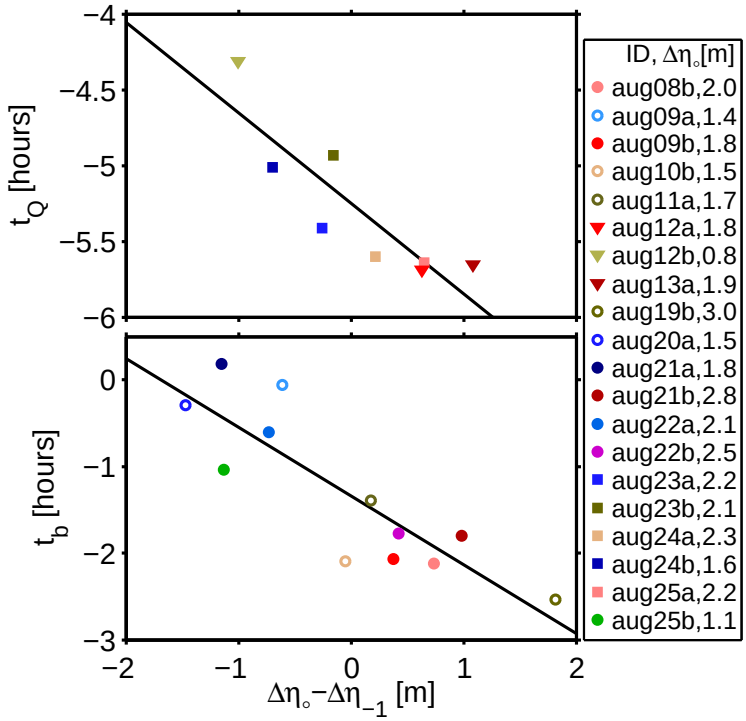

Figure 2.13: (a) Onset time t_Q of ebb flow at $x = -5$km and (b) time of front crossing ($x_f = b$) vs. diurnal inequality, $\Delta\eta_\circ - \Delta\eta_{-1}$. Squares and triangles are computed from $Q(t)$ along lines 0 and 1 respectively (Figure 2.12). Filled circles represent t_b for the primary fronts in Figure 2.8; open circles represent fronts that were not tracked offshore but for which t_b could be estimated from radar images.

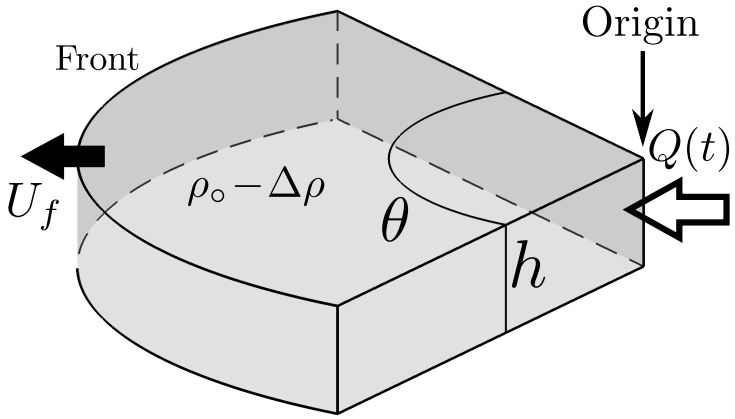

Figure 2.14: Perspective view of idealized geometry of *Chen* (1980)'s radially spreading plume model with time-dependent source volume flux, $Q(t)$.

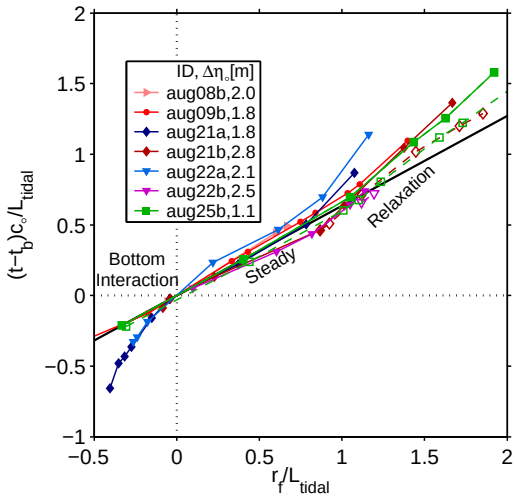

Figure 2.15: Non-dimensional plume front timing of all fronts observed. Note that the offshore direction is now to the right (increasing r_f). Dashed lines and open symbols mark NLIWs radiated from the fronts near $r_f/L_{\text{tidal}} = 1$.

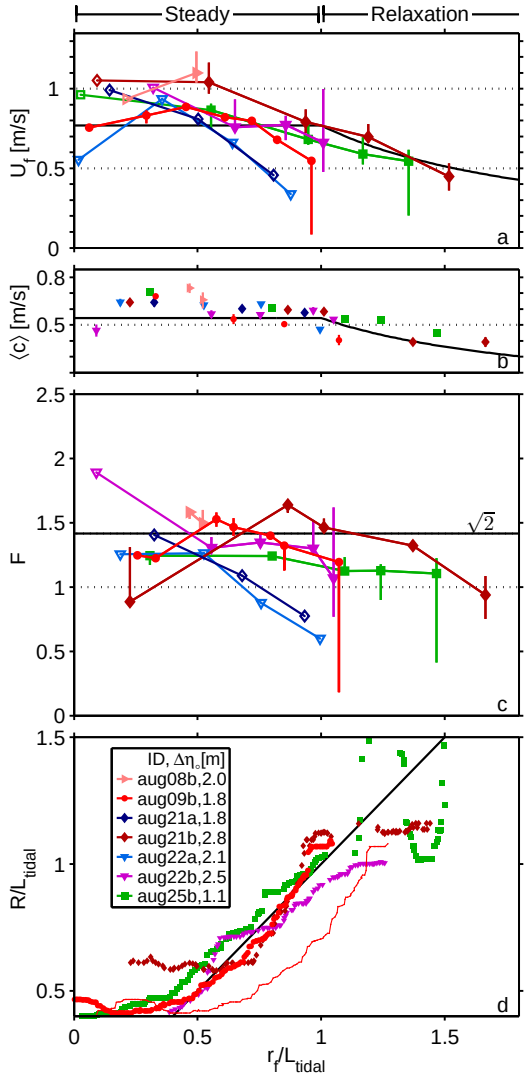

Figure 2.16: Front speed (a), plume 1st-mode wavespeed (b), frontal Froude number (c) and R/L_{tidal} (d) versus non-dimensional position, r_f/L_{tidal} for seven different fronts (color). Open symbols in (a) and (c) indicate points for which we assume $u_a = 0$, and error bars could not be estimated. In (d), red dots mark aug09b with $b = -11$km, a thin red line is for aug09b with $b = -8$km. All others, $b = -8$km. Front aug08b has been excluded from (d) because it was not resolved long enough to observe a period of expansion. Solid black lines indicate (*Chen*, 1980)'s solution.

Chapter 3 – The role of turbulent stress in the dynamics of the Columbia River outflow

Levi F. Kilcher, Jonathan D. Nash and James N. Moum

Abstract

Turbulent exchanges in river outflows determine the composition of source water to river plumes. Turbulent stress, τ, is understood to play a crucial in decelerating these outflows. This paper uses microstructure estimates of τ to investigate the dynamics of the Columbia River outflow in terms of ten varied-amplitude tidal cycles and during high and low river flow. Two contrasting momentum balances are found to be related to the barotropic tidal amplitude: 1) a high τ balance, in which turbulent stress divergence balances plume deceleration, and 2) a low τ balance, in which stress divergence and the surface pressure gradient are similar magnitude, and too weak to significantly decelerate the plume. High stress occurs during large ebbs, and low stress during smaller ones. Agreement between in-situ estimates of τ and a parameterization based on the shear-squared (S^2) in excess of four times the buoyancy frequency-squared ($4N^2$) indicates that shear instability is the dominant mechanism of turbulence generation. While the essential distinction between high and low stress is controlled by tidal amplitude during both river flow conditions, increased river flow augments this by raising N^2, decreasing plume thickness and raising S^2, causing higher stress-divergence during high τ ebbs. These results connect the dynamically significant turbulent stress at the plume base to the external forcing by tides and changes in river flow.

3.1 Introduction

Buoyant plumes form at the mouths of the world's rivers (e.g. *Wright and Coleman*, 1971; *Garvine*, 1974a; *De Ruijter et al.*, 1997; *Geyer et al.*, 2000; *MacDonald and Geyer*, 2004; *Houghton et al.*, 2004; *MacDonald et al.*, 2007; *Chant et al.*, 2008). Fed by the discharge through the mouth, these plumes disperse momentum, buoyancy, nutrients, toxins and organisms into the coastal ocean. The influence of these freshwater sources on coastal ecosystems is an issue of growing public concern (*Halpern et al.*, 2008). This being the case, a clearer understanding of the dynamics and mixing processes of these plumes is an increasingly active area of research.

Buoyant plumes can be divided into two classes based on the value of the Kelvin number, $K = L/L_{\mathrm{R}}$, which is the ratio of the plume length scale (L) to its Rossby radius (L_{R}) (*Garvine*, 1995). Based on this, Garvine describes a different set of features and dynamic balances for "small-scale" ($K < 1$), versus "large-scale" plumes ($K > 1$). While Garvine used K to classify plumes of different rivers, it is also applicable to distinct flow patterns (of particular L) within a single river's plume system. In particular, many recent plume studies define a "near-field" region just outside the river mouth, where outflow inertia is significantly larger than its buoyancy (the flow is super-critical) (e.g. *Hetland*, 2005). Garvine's description of small-scale plumes share many characteristics with the "near-field" region of large-scale river plumes.

Along these lines, *Horner-Devine et al.* (2009) have described the Columbia

River plume as a set of dynamic plume regimes within a single, broadly defined "river plume" system. A similar interpretation is likely to apply to other large-scale plumes with strongly tidal estuaries; i.e. partially or well mixed (*Hansen and Rattray, Jr.*, 1966). The near-field region is of particular importance because it is the site of a significant amount of mixing, thus creating the source waters for the large-scale "far-field" plume (*Hetland*, 2010).

3.1.1 Mixing in small-scale plumes

Small-scale buoyant plumes have been an active area of research for over 40 years. *Garvine* (1974a) documented large tidally-modulated variability in the location and thickness of the $\approx$ 3m thick Connecticut River plume. *Garvine and Monk* (1974) described a sharp frontal feature with strong surface velocity convergence at the offshore edge of the plume. A series of efforts to numerically model plumes with fronts (e.g. *Garvine*, 1982, 1984) eventually culminated with *O'Donnell* (1990), in which much of the *Garvine* (1974a) variability was reproduced. *Jay et al.* (2010) use Lagrangian frontal equations to investigate the role of various entrainment parameterizations on frontal dynamics.

Notably, these models only include mixing in the plume front. While frontal mixing is clearly important (*Luketina and Imberger*, 1989; *Orton and Jay*, 2005; *Kilcher and Nash*, 2010), and neglecting plume base mixing was a useful idealization, this approach contrasts observational studies that show that plume-base vertical mixing is an important component of the plume momentum and mass

budgets. *Wright and Coleman* (1971) reasoned that vertical mixing – rather than entrainment along the lateral boundaries – was the primary mechanism of dilution and deceleration of a spreading outflow in the Mississippi River delta. More recently, *Chen and MacDonald* (2006) found that vertical mixing is an important term in the heat budget of a thermally buoyant industrial plume. In the Columbia River plume, increasing salinity at surface drifters as they transit the plume, and "end-member" studies of passive chemical tracers clearly indicate mixing (*McCabe et al.*, 2008; *Bruland et al.*, 2008). Furthermore, *Nash et al.* (2009) showed that strong mixing within the estuary – controlled by the competition between vertical turbulent and horizontal freshwater fluxes – creates the source waters of the tidal plume.

While it is clear that vertical mixing plays an important role in buoyant plume dynamics, the relationship between the mean-flow properties that set this mixing (e.g. velocity, buoyancy, spreading, plume thickness) and the mixing itself are complex and poorly understood. For example, *Hetland* (2010) has shown that larger entrainment velocity near the mouth brings about less total dilution. This is due to the inverse relationship between entrainment and the area over which it occurs. Given this complexity, direct observations of mixing in buoyant plumes is likely to aid progress in this topic.

The majority of previous studies estimate mixing in plumes from changes in buoyancy or momentum (e.g. *Wright and Coleman*, 1971; *Chen and MacDonald*, 2006). There are two exceptions, in which direct estimates of turbulent quantities were made. *Luketina and Imberger* (1989) made the earliest microstructure ob-

servations of buoyant estuary discharges using high-frequency thermistors on an upward-rising vertical profiler. They identified three layers in the $\approx$ 4m thick outflowing plume: a surface wind-mixed layer, an intermediate stably stratified layer, and an unstably sheared mixing layer at the plume base (just above the ambient waters). More recently, *MacDonald et al.* (2007) compared TKE dissipation rate, ϵ, estimates from shear probes mounted at the nose of an autonomous underwater vehicle (AUV) with ϵ estimates from a control-volume analysis. That study found reasonable agreement between ϵ estimates from a control-volume analysis and the AUV-based microstructure measurements. A similar comparison, in this case using stress estimates from vertical microstructure profiles, is made here and different conclusions are deduced.

3.1.2 Dynamics of small-scale plumes

McCabe et al. (2009) described the surface momentum balance throughout ebb of the Columbia River outflow using a numerical model with realistic bathymetry, river flow, and surface and tidal forcing. They found that internal stress and the surface pressure gradient decelerated offshore flowing fluid inshore of the front. At peak ebb, this deceleration was dominated by the internal stress, but as ebb progressed the surface pressure gradient played an increasingly significant role. To our knowledge, no other study has described the momentum balance of near-field river outflows.

3.1.3 Outline

In the Columbia River near-field, strong ebb discharge through the mouth forms a rapidly expanding volume of buoyant fluid, the "tidal plume" (*Horner-Devine et al.*, 2009). *Kilcher and Nash* (2010) (hereafter KN10) described the structure and propagation of the front that formed at the leading edge of this plume. This front was found to propagate steadily, until the tidal plume had expanded beyond its own Rossby radius and ebb discharge began to weaken. At this time, the front decayed and the plume presumably became a part of the bulge, or "re-circulating plume", described by *Horner-Devine* (2009).

The work described in this paper compliments KN10 by investigating the flow in the plume base, inshore of the plume front. The objectives of this paper are to: 1) describe the structure of ebb discharge in this plume during periods of low and high river flow (section 3.3), 2) quantify the momentum budget of the plume using observed velocity and density fields (section 3.4), and 3) investigate the mean flow energy sources that power turbulence, thereby causing ϵ and turbulent stress (section 3.5). Section 3.6 summarizes results and discusses implications. Sampling and data collection methods are described in section 3.2.

3.2 Setting and Data

Located in the Northwestern United States, the Columbia River discharges into the Eastern Pacific Ocean between the states of Washington and Oregon (Figure 3.1). The bathymetry within 8km of the river mouth is relatively flat, shallow (water

depth, $d \approx 20$m) and roughly radially symmetric around the tip of the north jetty. A 20m deep shipping channel, which runs from the river mouth to the southwest, is the primary exception to this symmetry. Offshore of 8km the water depth increases rapidly from 20m to > 60m in only 2km (Figure 3.1a).

The origin of our chosen coordinate system is at 46.24° N, 124.08° W, with the positive x, u and y, v directions eastward and northward respectively (Figure 3.1). This coordinate system is approximately aligned with mean river discharge, perpendicular to the north-south coast, and its origin is just north of the tip of the south jetty. z is defined as positive upward from the ocean surface.

3.2.1 Sampling

The evolution of the outflow throughout each tidal period was captured by sampling continuously while transiting across or along the plume axis. The work presented here is focused on the "along-axis" structure of the outflow, which was captured by sampling along the line shown in Figure 3.1. Transects were made at ship speeds of 4-6knots through the water (2-10knots over land).

The data presented here were obtained during field studies in August 2005 and May 2006. The primary difference in environmental forcing between these periods is the difference in daily-mean river flow, $\overline{Q_f}$. During August 2005, $\overline{Q_f} \approx 4,000\text{m}^3\text{s}^{-1}$ was near the mean annual cycle low. The May 2006 study took place during the spring freshet when the river flow was a factor of 3 larger, $\overline{Q_f} \approx 12,000\text{m}^3\text{s}^{-1}$ (*Hickey et al.*, 2010).

Six "along-axis" tidal periods were sampled in August 2005 and four in May 2006 (Figure 3.2). Tidal amplitudes had similar variability during these periods, often exhibiting large diurnal inequality. Each tidal period is assigned a "tidal ID", which is composed of a three-letter month prefix ('aug'/'may') followed by its numeric day of that month and an 'a' or 'b' to denote the first or second ebb of that day, respectively. These data resolve both spring and neap conditions (e.g. aug19b vs. aug11a). All told, tidal amplitudes varied from $\Delta\eta < 1$m to ≈ 3m, where $\Delta\eta = \eta_{high} - \eta_{low}$ is the tidal elevation drop from the given ebbs preceding high tide (η_{high}) to its low (η_{low}). Tidal surface elevation, η, is taken from "xtide" tidal height estimates at the "Columbia River N. Jetty" site (*Flater*, 2008).

Wind velocity, $\vec{W}$, from NDBC buoy 46029 (measured at 5m above the surface and extrapolated to 10m) is shown in Figure 3.2b. Winds were generally light to moderate ($|\vec{W}| < 8\mathrm{m\,s^{-1}}$) and upwelling favorable, except during May 22-25, 2006 when the winds were stronger ($|\vec{W}| \approx 11\mathrm{m\,s^{-1}}$) and downwelling favorable (Figure 3.2b). We show that these winds were too weak to play a significant role in the nearfield dynamics of the outflow.

3.2.2 Data

This work combines microstructure profiles and shipboard acoustic Doppler current profiler (ADCP) measurements. Horizontal velocity estimates $(u(z), v(z))$ were obtained from a 1200kHz ADCP mounted on a pole alongside the ship 1m below the surface. This instrument measured water velocity in 0.5m bins from 2.2 to

24.2m depth. Because velocity profiles between the plume base and 2.2m were quite straight, we use a linear fit to velocity data between 2.2 and 4.7m to extrapolate velocity data to the surface. Near the bottom, where ADCP estimates are invalid due to side-lobe interference with the bottom (below 85% of the water depth), velocity was linearly interpolated from the last resolved bin to 0 at the bottom.

High-frequency noise in ADCP-derived velocity was removed using a 3-bin by 5-bin (1.5m vertically by 7.5s in time) running-median filter. Eastward, $\partial u/\partial z$, and northward, $\partial v/\partial z$, shear were computed from these screened data and horizontal shear squared was computed,

$$S^2 = \left(\frac{\partial u}{\partial z}\right)^2 + \left(\frac{\partial v}{\partial z}\right)^2 \qquad . \tag{3.1}$$

This was then smoothed using a 1.5m by 7.5s Bartlett filter. This methodology resulted in S^2 estimates with a noise floor of $10^{-3}\mathrm{s}^{-2}$. S^2 is computed only where the ADCP resolved the water column. From this we estimate the inverse gradient Richardson number, $Ri^{-1} = S^2/N^2$, when either S^2 or N^2 exceeds the S^2 noise level.

The Chameleon microstructure profiler, deployed ship-side to minimize contamination from the ship's wake, obtained highly resolved profiles of salinity, s, temperature, T, and vertical shear of small-scale horizontal velocity, $\partial u'/\partial z$. The buoyancy frequency, $N^2 = g/\rho_\circ \partial \rho_\theta/\partial z$, was estimated from potential density, ρ_θ, profiles with background density $\rho_\circ = 1024\mathrm{kg\,m}^{-3}$ and gravitational acceleration, $g = 9.81\mathrm{m\,s}^{-2}$. We define the plume freshwater fraction $j = (s_\circ - s)/s_\circ$ using a

background salinity of $s_\circ = 34.2$psu.

Turbulent kinetic energy (TKE) dissipation rate, ϵ, was estimated in 1-m bins by fitting $\partial u'/\partial z$ spectra measured by Chameleon's shear probes to theoretical turbulent shear spectra (*Moum et al.*, 1995). ϵ estimates can generally not be made above 4m depth where the profiler was accelerating and changing orientation. Furthermore, contaminated ϵ data were identified up to 9m depth when the ship's orientation and water-column shear combined to place the profiler in the ship's wake. Because this form of contamination occurred when the ship was traveling westward, we have restricted the analysis of turbulent quantities to eastward transects. Further details of the deployment of this instrument can be found in *Nash et al.* (2009) and KN10.

Vertical eddy viscosity, $K_{\rm v}$, and mass diffusivity, K_ρ were estimated by assuming a constant flux Richardson number of 0.17 (*Moum*, 1990),

$$K_{\rm v} = \frac{1}{1-R_f}\frac{\epsilon}{S^2} \tag{3.2}$$

$$K_\rho = \frac{R_f}{1-R_f}\frac{\epsilon}{N^2} \quad . \tag{3.3}$$

Eddy viscosity estimates were then combined with shear to estimate the x-z component of stress,

$$\tau = -K_{\rm v}\frac{\partial u}{\partial z} \quad . \tag{3.4}$$

In order to simplify the notation, we define τ as stress per unit mass (units of

$m^2 s^{-2}$), rather than the more conventional unit of stress per unit volume.

Bottom stress, τ_b, is estimated as $\tau_b = \langle \kappa z_b \epsilon \rangle_{ml}^{2/3}$, where $\kappa \approx 0.41$ is von Kármán's constant, z_b is the height above the bottom and $\langle\,\rangle_{ml}$ denotes an average over the bottom mixed layer (*Dewey and Crawford*, 1988). Surface wind-stress estimates, τ_s, are estimated using a quadratic drag law, $\tau_s = \rho_{air} C_d |\vec{W}|^2 / \rho_\circ$, where $\rho_{air} = 1.3 kg\, m^{-3}$ is the density of air, and $C_d = 0.0012$ is the drag coefficient (*Large and Pond*, 1981).

The plume front location, x_f, is the location of maximum horizontal velocity convergence at $z = -2.35$m (identified only in transects in which the front appeared, KN10). Throughout this work, time is relative to the time at which the front crossed the mid-point of the sampling region ($x = -7$km). This is extrapolated from the actual time and location the front is identified assuming the front propagates at $U_f = 1 m\, s^{-1}$ [KN10]. The plume depth, h_p, is arbitrarily defined as the depth where the velocity is 1/4 its surface value; i.e.,

$$h_p = -z(u(z) = u(0)/4) \qquad . \tag{3.5}$$

Offshore of the front, $x < x_f$, h_p is undefined.

The following notation is used to denote three averages: 1) $\langle\,\rangle$ denotes an average between $-9 < x < -5$km; 2) $\langle\,\rangle_p$ denotes an average within the plume over the same range; and 3) $\langle\,\rangle_\epsilon$ is the same as $\langle\,\rangle_p$ but only includes regions where ϵ estimates are valid (i.e., below 3.5m).

3.3 Plume structure and evolution

The flow through the Columbia River mouth is tidally forced. During flood, the river flow is choked off by the rising tide and the estuary fills with salty coastal water, mixing it with fresher river water. During ebb, the tide drops and the estuary discharges mixed water through the mouth. In this section we describe and compare the evolution and structure of ebb discharge under low and high $\overline{Q_f}$.

3.3.1 Ebb evolution: low $\overline{Q_f}$

The second ebb of August 20$^{\text{th}}$ (aug20b) was the larger ebb of the day during spring tides ($\Delta\eta = 3.0$m), low $\overline{Q_f} \approx 4,000\text{m}^3\text{s}^{-1}$ and mildly upwelling winds (Figure 3.2). Below, we describe this ebb's evolution in terms of five stages: pre-front, front, peak-ebb, ebb and late-eb b (Figure 3.3).

3.3.1.1 Pre-front

During the pre-front stage, a thin layer (2m) of low density ($\approx 1021\text{kg}\,\text{m}^{-3}$) fluid was present at the surface (Figure 3.3a), presumably remnants of the previous ebb's discharge. S^2 was mildly elevated above 5m (d), but not strong enough to cause super-critical $Ri^{-1} > 4$ (e). A narrow band of low S^2 and N^2 existed in the range $-10 < z < -5$m (c,d), and throughout the upper 10m $\epsilon < O(10^{-6}\text{W}\,\text{kg}^{-1})$ was weak (f).

In the lower half of the water column, a thin band of elevated $4N^2$ and S^2

marked an intrusion layer of 1025.7 density water (dashed isopycnal) that flowed over the top of a well-mixed bottom boundary layer (BBL) before flowing offshore over the end of the bar (b,c,d). The core of this intrusion layer had a low Ri^{-1} core where $\partial u/\partial z$ changes sign (e). ϵ was elevated along the top edge of the intrusion and near the bottom in the BBL (f).

At the end of the bar ($x \approx -7.7$km) the intrusion thinned to < 5m, suggesting that it accelerates as it flows down-slope and offshore (*Farmer and Armi*, 1986, Figure 8f). Elevated ϵ at this location and leveling of the isopycnal suggests the presence of a hydraulic jump (e.g. *Nash and Moum*, 2001).

3.3.1.2 Front

We subjectively identify a "frontal region" based on isopycnal displacement and velocity structure (Figure 3.3, magenta bar in "front" column). Offshore of the frontal region, surface fluid moved at $< 0.5\mathrm{m\,s^{-1}}$. Onshore of it, surface fluid moved offshore at $> 2\mathrm{m\,s^{-1}}$. This velocity difference, and the convergence it represents, caused $O(0.04\mathrm{m\,s^{-1}})$ downwelling velocities and large isopycnal displacement ($1024\mathrm{kg\,m^{-3}}$ isopycnal displaced > 10m). Within the frontal region, N^2 was low and fluid from the surface to near the bottom moved offshore at $\approx 1\mathrm{m\,s^{-1}}$.

This provides an additional example of the complex, bottom-interacting fronts described by KN10. In this example the frontal region was wider than KN10's Figure 6a, and surface fluid inshore of the front was slightly less dense than offshore of it ($2\mathrm{kg\,m^{-3}}$). The negative surface density gradient contrasts KN10's "reverse

front", in which surface density offshore of the front was lower than inshore of it. In both cases, however, the front's propagation must be driven by inertia (since it can not be driven by buoyancy). In this example, the cross-front buoyancy gradient is too weak, while in KN10's reverse fronts it had the wrong sign. *McCabe et al.* (2009) indicated that the low buoyancy fluid just inshore of the front is fluid that was pulled into the estuary during late flood. As flow through the mouth reversed to ebb, this fluid was at the leading edge of the outflow, without having had time for its buoyancy to increase by mixing with fresher estuary fluid.

Intense ϵ is observed at the bottom within the frontal region. Along the leading edge of the front ϵ ($= O(10^{-6}\mathrm{W\,kg^{-1}})$) is elevated compared to background levels ahead of the front, but is lower than along the trailing edge of the front, or in the plume base. Further investigation of the dynamics of the flow in this front is left for future work.

The thick grey line indicates the plume depth. Surface fluid within the plume flowed offshore at $> 2.5\mathrm{m\,s^{-1}}$. The entire water column was highly sheared and Ri^{-1} was super-critical, which drove intense TKE dissipation, $\epsilon \geq O(10^{-4}\mathrm{W\,kg^{-1}})$. Just offshore of the front a dense, thin BBL is recognizable and associated with elevated ϵ.

3.3.1.3 Peak-ebb

During peak ebb, surface fluid speed exceeded $2\mathrm{m\,s^{-1}}$ (Figure 3.5b). Within the plume $S^2 > 10^{-2}\mathrm{s^{-2}}$ is intense, and drives super-critical Ri^{-1} throughout the

water column (d,e). This super-critical S^2 drove instabilities that powered intense turbulence ($\epsilon = 10^{-4}\mathrm{W\,kg^{-1}}$ within the plume, and $10^{-5}\mathrm{W\,kg^{-1}}$ below it), mixing fresher estuary water near the surface with saltier fluid below (f). The $1020\mathrm{kg\,m^{-3}}$ isopycnal shoals from the bottom at the onshore end of the transect to the surface at the offshore end. Though turbulence is intense, it is not strong enough to account for the slope of this shoaling isopycnal. Instead, this isopycnal must have been advected to this location by the mean flow. This flow interacts strongly with the bottom, as indicated by two bands of S^2 that extend to the bottom near $x = -6.8$ and -6km [similar structure was seen in KN10, Figure 4].

3.3.1.4 Mid-ebb

Two hours after the passage of the front, the plume buoyancy had increased, resulting in higher stratification in the plume and its base (a,c). Plume thinning increased S^2 so that Ri^{-1} remained super-critical (d,e). Below the plume, patchy Ri^{-1} was well-correlated with ϵ, suggesting that shear instability drove turbulence below the plume base as well (f). As ebb continued to weaken (second mid-ebb column, 3.1hours after front), the plume thinned and Ri^{-1} decreased to critical. Below the plume Ri^{-1} was sub-critical, except for a region of low S^2 and N^2 near $x = -6.1$km. Because the plume thinned to < 5m, our profiler resolved little of its turbulence. However, decreased Ri^{-1} suggests that turbulence may have weakened. Below plume $\epsilon \leq O(10^{-6}\mathrm{W\,kg^{-1}})$ was two orders of magnitude lower than it had been two hours earlier.

3.3.1.5 Late-ebb

Four and a half hours after front passage, plume fluid still moved offshore, but S^2 had weakened and Ri^{-1} was sub-critical. Below the plume, onshore flow indicated that the salt wedge had begun moving back upstream as the tidal flow through the mouth drew salty fluid back into the estuary. Below the plume $\epsilon < 10^{-6}\mathrm{W\,kg^{-1}}$ was low.

3.3.2 Ebb evolution: high $\overline{Q_f}$

The high $\overline{Q_f} \approx 12,000\mathrm{m^3 s^{-1}}$ present during ebb may29b (Figure 3.4) contrasts the low $\overline{Q_f}$ present during aug20b (Figure 3.3). Otherwise, these two ebbs occurred under similar environmental conditions: both were during weak winds, were greater ebbs, and had similar tidal amplitude ($\Delta\eta = 2.8\mathrm{m}$). The transect length during ebb aug20b was longer, resulting in longer time between successive transects.

The influence of high $\overline{Q_f}$ is apparent in the relatively low density of both surface and ambient waters compared to aug20b. Surface fluid was roughly $6\mathrm{kg\,m^{-3}}$ lighter, and ambient was $\approx 1\mathrm{kg\,m^{-3}}$ lighter than during low $\overline{Q_f}$. This results in a roughly 50% larger $\langle \Delta\rho \rangle_\mathrm{p}$ during this ebb, compared to aug20b.

3.3.2.1 Pre-front

Two and a half hours prior to the arrival of the front, a $\approx 2\mathrm{m}$ thick layer of low density fluid was present at the surface ($\sigma_\theta(z=0)$ was as low as $10\mathrm{kg\,m^{-3}}$), creating

a highly stratified surface layer (Figure 3.4a,c). Because velocity was unresolved by our measurements at this depth, it is possible that extrapolated velocity obscures the presence of stronger fluid speeds in this layer.

A mid-depth ($-13 < z < -7$m) region of low N^2, S^2 and $\epsilon = O(10^{-8}\mathrm{W\,kg^{-1}})$ separates the surface layer from a $5 - 10$m thick BBL (c,d,f). As was the case in the pre-front BBL of aug20b (Figure 3.3c), the BBL height is most clearly seen here as a band of elevated $N^2 = O(10^{-3})$ (Figure 3.4c). It is noteworthy that N^2 at the top of this BBL is lower than during aug20b (in contrast to higher N^2 in this surface layer). Within the BBL the fluid was relatively well mixed so that moderate S^2 drove super-critical Ri^{-1}, and thus caused $\epsilon = O(10^{-5}\mathrm{W\,kg^{-1}})$ to be two orders of magnitude larger than at mid-depth (f). As was the case for aug20b, the thinning, turbulent flow over the end of the bar suggests the presence of super-critical down-slope flow.

Based on these observations, we identify three distinct vertical levels: 1) a turbulent highly stratified and sheared surface layer ($z > -2$m), 2) a mid-depth region of low S^2, N^2 and ϵ, and 3) a low N^2 turbulent BBL that is capped by a moderately stratified layer near $z = -15$m.

3.3.2.2 Front

The most apparent difference between this front and that of aug20b was the much smaller vertical displacement (Figure 3.4). Isopycnal displacements in this front were only $\approx$ 2m, nearly an order of magnitude smaller than the $>$ 10m displace-

ments observed during aug20b. Furthermore, this front was highly buoyant and stratified, while aug20b was notably unstratified. As in aug20b, TKE dissipation increased from ambient levels at the leading edge to $\epsilon = O(10^{-6}\mathrm{W\,kg^{-1}})$ at the onshore end of the frontal zone (f). This suggests the growth of a sub-plume layer formed by the mixing in "the collapsed wake from billows" generated at the front (*Britter and Simpson*, 1978).

Another noteworthy feature of this flow is that h_p is smallest just inshore of the front (at x_f). Isopycnals in the front curve downward in the front (around the head wave) and up again near x_f. This agrees with *Britter and Simpson* (1978)'s observation that a laboratory gravity current was thinnest just inshore of the front's head.

Within the plume (inshore of x_f), Ri^{-1} was super-critical and $\epsilon = O(10^{-5}\mathrm{W\,kg^{-1}})$ intense. High N^2 in the plume just behind the front contrasted that of aug20b, where N^2 was low and Ri^{-1} was highly super-critical. Furthermore, the three-layered structure of the water column persisted, even beneath the front. ϵ in the bottom boundary layer remained high, while at mid-depth S^2, N^2 and ϵ were low. This is yet another contrast to aug20b, where the large frontal amplitude extended throughout the water column and wiped out the bottom boundary layer.

The presence of a hydraulic jump is suggested where the $1024\mathrm{kg\,m^{-3}}$ isopycnal slopes down over the end of the bar, rebounds upward 10m at $x = -8.1$km, then returns to $z \approx -22$m farther offshore. Elevated ϵ below the apex of the isopycnal encourages the notion that this is a hydraulic jump, but better estimates of near-bottom velocity would be required to confirm it.

3.3.2.3 Peak-ebb

Two hours later, during peak-ebb, very low density ($\approx 1005\mathrm{kg\,m^{-3}}$) surface fluid moved offshore at $> 2.5\mathrm{m\,s^{-1}}$. Plume S^2 is super-critical ($Ri^{-1} > 4$) and highly energetic ($S^2 \gtrsim 10^{-1}\mathrm{s^{-2}}$), driving intense TKE dissipation, $\epsilon = O(10^{-3}\mathrm{W\,kg^{-1}})$. The sub-plume layer is a region of weaker S^2, but similar Ri^{-1}, extending below the plume base drives moderate turbulence ($\epsilon > O(10^{-5}\mathrm{W\,kg^{-1}})$). Below this, the low Ri^{-1}, low S^2, low ϵ mid-depth region persists as a thin layer between the plume and the BBL.

This suggests the presence of four layers: 1) the plume replaced the buoyant, remnant plume surface layer of the pre-front stage; 2) a sub-plume layer of decreasing S^2 and N^2, but high Ri^{-1} and ϵ; 3) the mid-depth quiescent layer, which had become quite thin; and 4) the BBL, whose $\epsilon < O(10^{-5}\mathrm{w\,kg^{-1}})$ weakened as near-bottom flow reversed to onshore. The presence of the quiescent mid-depth layer indicates that, throughout peak ebb, this plume remained separated from the bottom, in contrast to aug20b.

3.3.2.4 Mid-ebb

As ebb weakened during mid-ebb, the plume thinned ($h_\mathrm{p} \approx 4.5\mathrm{m}$), surface density increased and velocity decreased. Thinning maintained super-critical Ri^{-1} but the plume became too thin for our profiler to resolve ϵ. In the sub-plume layer, Ri^{-1} was super-critical and $\epsilon = O(10^{-5}\mathrm{W\,kg^{-1}})$ was elevated.

Below $z = -8\mathrm{m}$ the flow onshore flow appeared to have brought dense fluid

over the bar (the 1024kg m^{-3} isopycnal was farther from the bottom than during front passage or peak-ebb). N^2, S^2 and Ri^{-1} are patchy and do not show a clear BBL as in earlier transects. ϵ continues to weaken and is well correlated with Ri^{-1}.

3.3.2.5 Late-ebb

Six hours after the front passed (late-ebb), the plume had thinned to $h_\mathrm{p} \approx 3$m and was still strongly stratified and sheared (c,d). Below the plume, flood weakened as high tide approached (b). $S^2 \leq O(10^{-3}\mathrm{s}^{-2})$ and $\epsilon = O(10^{-7}\mathrm{W\,kg}^{-1})$ were weak throughout the water column (c,f). It is noteworthy that during this high river flow period, the offshore flow of buoyant estuary fluid persisted throughout the tidal cycle. This contrasts low-flow where surface velocity reversed during flood (not shown).

3.3.3 Vertical structure

Figure 3.5 presents vertical profiles of various quantities during low (aug20b, top) and high (may29b, bottom) $\overline{Q_f}$ during pre-front, front, peak-ebb and late-ebb stages (as labeled in Figures 3.3 and 3.4). In both cases, water-column velocity increases abruptly as the front passes, then decreases after peak-ebb. After the front passes, surface density decreases monotonically in time (b). The surface density of ebb may29b was lower, and plume N^2 and S^2 were higher during each stage.

The vertical structure of the pre-front stage for ebbs aug20b, and may29b are remarkably similar. Both have a low speed, low density, high N^2 surface layer roughly 3m thick, above a low N^2 layer centered near $z = -7$ and -8m. Below this, during aug20b, an offshore-flowing intrusive layer centered at $z = -15$m is apparent in the velocity profile. Ri^{-1} was critical along the top and bottom edges of this layer, and $\epsilon = 4{\times}10^{-6}$ was highest along the top edge. Rather than an intrusive layer, may29b had an offshore-flowing 9m-thick BBL. N^2 was elevated along the top of this layer, and dropped by an order of magnitude near the bottom. Along the top of the BBL where S^2 was resolved, Ri^{-1} was super-critical and ϵ was elevated within the BBL ($O(10^{-5}\mathrm{W\,kg^{-1}})$.

Therefore, though not as clear in Figure 3.3a as in 3.4a, we have observed a similar layered structure for ebb aug20b as described for may29b in section 3.3.1.1. The distinction between BBL and intrusive layer is interesting, but minor. In fact, in the transect between Figures 3.3a and b (not shown), a BBL had formed, the remains of which are seen just offshore of the front in Figure 3.3b.

While the pre-front stage of ebbs aug20b and may29b may have been similar, the same is not true for the "front" and "peak-ebb" stages. Reduced density water was present near the bottom during the "front" and "peak-ebb" stages of aug20b (by 2-3$\mathrm{kg\,m^{-3}}$). By late ebb, near-bottom density had returned to its background value. This contrasts ebb may29b, during which near-bottom density was relatively constant. Furthermore, velocity profiles are quite straight in comparison to the hockey-stick structure of may29b and late-ebb of aug20b. The curvature in u profiles that does exist corresponds to a factor of 10 decrease in S^2 (d). This is

modest compared with other S^2 profiles, which varied by at least 50 (late-ebb of may29b varied by 500). The high S^2 of aug20b caused highly super-critical Ri^{-1} throughout the water column, particularly behind the front and below the plume where plume shear was encountering relatively unstratified water (aug20b panel e, blue line, below $z = -13$m). We interpret the low-density near-bottom water, nearly linear velocity profiles, and top-to-bottom super-critical Ri^{-1} as indications of bottom interaction during the "front" and "peak-ebb" stages of ebb aug20b.

In contrast to the bottom-interacting single layer during peak-ebb of aug20b, we identify four vertical layers during the front and peak-ebb stages of may29b: 1) the plume, 2) the sub-plume layer, 3) a mid-depth layer, and 4) a BBL. Within the plume layer (marked by ticks on the profiles), density and velocity profiles were remarkably straight (a,b). Surface density was low ($1005\mathrm{kg\,m^{-3}}$) and velocity swift ($\approx 3\mathrm{m\,s^{-1}}$), leading to strong and nearly uniform $4N^2$ and S^2, both of which were $O(10^{-1}\mathrm{s^{-2}})$ (c,d). Ri^{-1} was super-critical within the plume, and $\epsilon = O(10^{-4}\mathrm{W\,kg^{-1}})$ was high behind the front, and higher yet during peak-ebb, $\epsilon = O(10^{-3}\mathrm{W\,kg^{-1}})$ (e,f).

The sub-plume layer was characterized by decreasing N^2, S^2 and ϵ with depth, but persistently super-critical Ri^{-1}. This is similar to the intermediate mixing layer of *Britter and Simpson* (1978) (in their Figure 3, this layer is defined to have thickness h_3). In that study, the surface layer (bottom layer, in their case) had constant ρ and u (low S^2,N^2), and density and velocity changed in the intermediate layer (higher N^2 and S^2). This contrasts our results, in which density and velocity change continuously throughout the plume to background levels at the base. Thus,

N^2 and S^2 profiles in this work appear to be analogous to $\Delta\rho$ and u in *Britter and Simpson* (1978): high and constant within the plume and decreasing in the intermediate layer.

In the mid-depth layer ($z \approx -12$m), S^2, N^2 and ϵ are low and Ri^{-1} drops to critical. Below this is the BBL, in which N^2 decreases toward the bottom, Ri^{-1} is super-critical and $\epsilon \approx 6{\times}10^{-6}\,\mathrm{W\,kg^{-1}}$ is elevated.

The late-ebb stage of may29b showed similar structure to peak-ebb, but the plume and intermediate mixing layers were significantly thinner and the mid-depth low Ri^{-1} layer filled the majority of the water column. From peak-ebb to late-ebb, velocity below the plume was weakly onshore ($\lesssim 0.1\mathrm{m\,s^{-1}}$), indicating that this plume was not interacting with the bottom (τ_b has the wrong sign). Ri^{-1} was super-critical in the lower half of the water column and $\epsilon \approx 3{\times}10^{-6}\,\mathrm{W\,kg^{-1}}$ was elevated above that at mid-depth. However, increasing N^2 near the bottom suggests that a BBL was not present at this time.

3.3.4 Evolution

Sections 3.3.1 and 3.3.2 described the internal structure of the outflow along the plume axis during low and high $\overline{Q_f}$, respectively. Section 3.3.3 compared the vertical structure of those ebbs. In this section we present and compare the evolution of plume-averaged quantities.

Initially, plume aug20b is thicker and saltier than may29b (Figure 3.6a,b). During both ebbs, the passage of the front is marked by a sharp increase in surface

layer velocity from 0.4 to $\approx 1.5\mathrm{m\,s^{-1}}$ (c). This causes the S^2 to exceed $4N^2$ in a bulk sense, so that the plume averaged Ri^{-1} becomes super-critical and TKE dissipation increases by more than an order of magnitude (d,e,f).

During the first three hours after the front passes fluid velocities within the plume change only moderately: aug20b decelerates gradually to $\approx 1.2\mathrm{m\,s^{-1}}$ and plume may29b increases to $1.9\mathrm{m\,s^{-1}}$. During this time both plumes thin and their freshness (buoyancy) increases. These processes cause S^2 and $4N^2$ to increase in parallel so that each plume maintains super-critical Ri^{-1}. This super-critical S^2 drives intense TKE dissipation and internal stress (h). Finally, more than 4 hours after the front, plume velocity and S^2 decrease, resulting in a decrease in Ri^{-1} and a drop in ϵ.

Looking at each ebb separately, the highest values of Ri^{-1} are associated with the largest values of ϵ. However, comparing these quantities between ebbs reveals a contrasting story. The largest Ri^{-1} estimate occurs during low $\overline{Q_f}$ conditions (aug20b), while the largest ϵ estimates occurs in high $\overline{Q_f}$ (may29b). This discrepancy can be partially explained by the much larger S^2 (and therefore energy) present during high $\overline{Q_f}$. We therefore anticipate that a proper scaling of ϵ will involve both Ri^{-1} and S^2 (e.g. *Kunze et al.*, 1990, eqn. 9), and we test this in section 3.5.

3.3.5 Summary of outflow evolution and structure

The Columbia river outflow is strongly tidally forced. Here we have focused on the ebb stage of evolution, when buoyant estuary fluid is discharged from the mouth

and flows offshore across the ocean surface. The evolution and internal structure of the plume was resolved in terms of multiple repeat transects along its.

The evolution of two large-amplitude tidal cycles (both had $\Delta\eta \approx 3$m) during contrasting river flow states were presented in terms of five ebb stages: pre-front, front, peak-ebb, mid-ebb and late-ebb. Weak offshore flow begins during the the pre-front stage. Shortly thereafter, the front, a region of strong surface velocity convergence and internal turbulence, passed through the domain. The dynamics of frontal propagation were investigated in *Kilcher and Nash* (2010). During the peak-ebb stage, u, S^2 and ϵ were high. Throughout mid-ebb, the plume thinned as its buoyancy increased. This caused S^2 and N^2 to increase. In these examples, S^2 maintained a slightly higher value than $4N^2$, so that Ri^{-1} was unstable to Kelvin-Helmholtz billowing throughout peak- and mid-ebb, which drove vigorous ϵ. Not including the front stage, τ was highest during peak-ebb.

3.4 Plume Momentum

Our goal is to determine the relative contributions of the viscid (i.e. turbulent stress) and inviscid terms (i.e., pressure gradient, Coriolis effect) in the momentum balance of a fluid parcel transiting the near-field during ebb. Applying the Boussinesq approximation and assuming that vertical turbulent fluxes are larger than horizontal, the along-axis momentum equation is,

$$\frac{\partial u}{\partial t} + \vec{u} \cdot \vec{\nabla} u - fv + \frac{\partial P}{\partial x} + \frac{\partial \tau}{\partial z} = 0 \qquad . \tag{3.6}$$

Here, P is the reduced pressure, which can be written in terms of its baroclinic (P_{bc}) and barotropic (P_η) components assuming a hydrostatic balance:

$$\begin{aligned} P = & \underbrace{\frac{g}{\rho_\circ}\int_z^0 \rho \mathrm{d}z'}_{} + \underbrace{g\eta}_{} \\ = & \quad P_{\mathrm{bc}} \quad + \quad P_\eta \end{aligned} \quad , \tag{3.7}$$

where $\rho_\circ = 1024.6\,\mathrm{kg\,m^{-3}}$ is the reference density.

Our observations directly resolve most of the terms in (3.6), which are detailed in Figure 3.7. The local acceleration, $\partial u/\partial t$, is computed from the observed change in velocity between consecutive transects. The Coriolis acceleration, $-fv$, is computed directly from the observed northward velocity. The baroclinic pressure gradient, $\partial P_{\mathrm{bc}}/\partial x$, is estimated from the observed density field (details in appendix B). The stress profile is estimated from the measured shear and ϵ according to (3.4).

The advective term, $\vec{u}\cdot\vec{\nabla}u$, has three parts, $u\frac{\partial u}{\partial x} + v\frac{\partial u}{\partial y} + w\frac{\partial u}{\partial z}$. The first of these is measured directly by our observations, but the latter two are not. In a spreading and thinning flow such as this, these parts are similar magnitude to the first. We use a control-volume method similar to that of *MacDonald and Geyer* (2004) (hereafter MG04) to estimate them. This involves estimating lateral spreading (the rate at which plume width b increases with $-x$; i.e., db/dx), by conserving freshwater flux along the transect. The vertical structure of spreading (db/dx) is unknown and so is assumed to be invariant with depth. As detailed in the appendix, db/dx is used in a volume conservation equation to obtain an

estimate of the vertical velocity, w and $\partial u/\partial y$ terms, allowing all terms in $\vec{u} \cdot \vec{\nabla} u$ to be estimated.

The remaining term in (3.6) is the surface pressure gradient, $\partial P_\eta/\partial x$. This term is also not measured directly. We estimate it so that it balances the depth-integrated form of (3.6), with τ_s and τ_b used as upper and lower boundary conditions, respectively (see Appendix B).

Throughout this section the scaled depth coordinate is,

$$z^* = \frac{z}{h_{\mathrm{p}}(x)} \qquad . \tag{3.8}$$

In order to highlight the plume and plume base, henceforth we limit our attention to the depth range $0 > z^* > -1.6$.

In the following we investigate the momentum balance of a single, example transect which highlights the importance of turbulent stress. We then examine the momentum balance for multiple ebb pulses, specifically highlighting two subsets of the data: 1) where stress clearly controls plume deceleration, and 2) where both stress, surface pressure gradient and the Coriolis effect are likely important.

3.4.1 Example momentum balance: a greater ebb during low $\overline{Q_f}$ (August 2005)

This section presents the momentum balance during peak ebb of aug20b. This was a greater ebb during low $\overline{Q_f}$ and weak winds. The transect was made one hour

after the front passed. At this time the plume was thick and isopycnal slopes were high (Figure 3.3c). Flow was offshore throughout the water column with shear increasing toward the surface (Figure 3.8a, solid line).

3.4.1.1 Acceleration

At peak ebb, the local acceleration, $\partial u/\partial t$, is positive throughout the water column, indicating that offshore flow speed is decreasing in time (Figure 3.8b, magenta). We note that $\partial u/\partial t$ is largely barotropic in this example, suggesting that it is associated with time dependence of the barotropic tide, and not specifically deceleration of the plume, which is surface-intensified. However, having examined dozens of transects in detail, we note that the variability of $\partial u/\partial t$ from transect to transect is generally substantial, often $0.5{\times}10^{-4}\,\mathrm{m\,s^{-2}}$ or greater, and does not vary smoothly in time. While primarily $\partial u/\partial t$ is barotropic (as in this example), there are often periods where it exhibits significant baroclinicity.

Momentum advection, $\vec{u}\cdot\vec{\nabla}u$, is positive near the surface, indicating that more offshore momentum is being fluxed in the onshore side (or bottom) of the control-volume than out the offshore end (Figure 3.8b, blue). Over the range $-0.25 > z^* > -1$ this term is negative but smaller magnitude than the local acceleration. Therefore, the total acceleration,

$$\frac{Du}{Dt} = \frac{\partial u}{\partial t} + \vec{u}\cdot\vec{\nabla}u \qquad , \tag{3.9}$$

is positive throughout the plume (i.e. $z^* > -1$), indicating that the speed of offshore-flowing plume fluid is decreasing (Figure 3.8c, purple). Because we are concerned with offshore-flowing parcels, throughout the remainder of this work we refer to positive Du/Dt as "deceleration".

Since Du/Dt is the sum of two large terms of opposing sign, caution is necessary where its magnitude is small compared to error in the constituent terms. Specifically, internal waves and other sources of short timescale or short wavelength motions are included in both $\partial u/\partial t$ and $\vec{u}\cdot\vec{\nabla}u$, and introduce variability in Du/Dt, which may be balanced by wave stresses that have been implicitly neglected in this analysis. In summary, we have some confidence in individual estimates of Du/Dt within the plume, but require averages over multiple ebbs to gain insight in the weaker region below the plume. We search now for the force term(s) in (3.6) which balance the observed near-surface plume deceleration.

3.4.1.2 Coriolis acceleration

Upwelling favorable winds during Aug 2005 produced a weak southward flow along the Washington coast, resulting in a small contribution from the Coriolis term (Figure 3.8). This term is smaller but the same sign as Du/Dt, suggesting that it too requires a force directed shoreward to balance it. The finding that the magnitude of fv is relatively small is consistent with model results of *McCabe et al.* (2009) for the Columbia River plume during the August 2005 period.

3.4.1.3 Pressure gradient

The surface pressure gradient, estimated as a residual in the depth-integrated balance, is near zero (Figure 3.8c, green at $z^* = 0$). Therefore the large deceleration of surface fluid is not forced by the surface pressure gradient. The baroclinic pressure gradient, on the other hand, is significant in this example – with a maximum magnitude about half that of the near-surface material deceleration. However, while the total pressure gradient does act to decelerate offshore-flowing fluid, the sense of the baroclinic gradient is to decelerate fluid beneath the plume more than that at the surface, which is opposite to that required to produce the observed Du/Dt. Thus, the baroclinic pressure gradient has the effect of increasing the stress-divergence required to balance the observed Du/Dt, albeit weakly. Note however that, this is the largest baroclinic pressure gradient that we observed (note steep isopycnal shoaling, Figure 3.3c), suggesting that, in general, the baroclinic pressure gradient is not a dominant term in the plume momentum balance.

3.4.1.4 Internal stress

The internal stress, τ, is plotted in Figure 3.8d (red line). Positive stress indicates downward flux of offshore momentum. The surface wind-stress, $\tau_s \approx 3\times10^{-6}\,\mathrm{m}^2/\mathrm{s}^2$, is three orders of magnitude smaller than the nearest-surface microstructure estimate, and does not apply a dynamically significant force on the plume. The rapid change from this low value to the nearest-surface estimate (at $z^* \approx -0.25$) indicates a large internal stress divergence (c,d red dotted line). The bottom stress,

$\tau_b < O(10^{-4}\mathrm{m}^2\mathrm{s}^{-2})$, is an order of magnitude smaller than internal τ. Thus, as with the surface stress, the bottom stress does not play a significant role in the plume dynamics.

In this example, the magnitude and sign of near-surface stress divergence is approximately equal and opposite to Du/Dt (compare purple and red in Figure 3.8c), indicating that the observed deceleration is forced by the stress divergence in the upper plume. Within the middle third of the plume, τ is relatively constant, which agrees with weak deceleration there. At the plume base, τ decreases rapidly, thereby transmitting the momentum lost near the surface into the fluid at the plume base. Momentum is thus transported by turbulence through the plume, decelerating fluid above $z^* = -.5$ and depositing this momentum near $z^* = -1$. However, we note that the control volume does not indicate an acceleration of fluid (Du/Dt) at $z^* = -1$ commensurate with the observed stress divergence.

3.4.1.5 Residual stress

Without direct estimates of internal stress divergence, MG04 estimated it as a residual in the momentum budget,

$$\frac{\partial r_\tau}{\partial z} = -\frac{Du}{Dt} - \frac{\partial P}{\partial x} + fv \qquad . \tag{3.10}$$

We refer to this as the "residual-stress" divergence (Figure 3.8c, dark-red line). It is the force required to balance the control-volume's estimate of acceleration

after accounting for the pressure gradient force and Coriolis effect. Comparison of $\partial r_\tau/\partial z$ with $\partial\tau/\partial z$ is an alternate way to assess the accuracy of the control-volume method. In particular, agreement of the magnitude of $\partial r_\tau/\partial z$ with $\partial\tau/\partial z$ suggests that, in this example, the control-volume method produces a reasonable estimate of plume deceleration. The difference in the near-surface stress divergence is not statistically significant.

At the plume base, however, $\partial r_\tau/\partial z$ does not agree with $\partial\tau/\partial z$. This is the same discrepancy mentioned in the previous section (between plume acceleration and $\partial\tau/\partial z$), now in terms of $\partial r_\tau/\partial z$. Here, it is manifested as $\partial r_\tau/\partial z$ being roughly constant below $z^* = -1$, rather than showing a peak near $z^* = -1$ (as observed in $\partial\tau/\partial z$). This results in a gradually changing r_τ below the plume base (Figure 3.8). Interpreting r_τ as an estimate of stress would suggest that there is a stress divergence below the plume base, when in fact there is none. This discrepancy is most likely due to the depth-invariant spreading assumption. A better understanding of the z-dependence of lateral spreading (db/dx) is likely to ameliorate this issue.

3.4.1.6 Summary of example balance

In summary, during peak ebb of aug20b (Figure 3.3c), the dominant dynamic balance in the upper plume is between deceleration and internal stress divergence. The baroclinic pressure gradient plays a lesser role in the momentum balance, acting to weakly accelerate surface-plume waters relative to those below. Thus

isopycnal shoaling ($\partial P_{\mathrm{bc}}/\partial x$) increases the required stress divergence for a balanced flow (compared to Du/Dt alone). All other terms in (3.6) (surface pressure gradient, Coriolis acceleration, surface and bottom stresses) are relatively small.

The $\partial\tau/\partial z$ profile indicates that internal τ is fluxing momentum from the near-surface waters downward until it is deposited at the plume base. However, at that location, the control-volume method does not indicate there are sufficient terms in (3.6) to balance the stress-divergence. Specifically, fluid is not found to accelerate at that depth, nor is the baroclinic pressure gradient sufficient to balance it. Without an inviscid sink for momentum near $z^* = -1$, the control-volume method implies transmission of momentum far below the plume base. This contrasts our turbulence observations, in which find weak stress (and stress divergence) below the plume base. We attribute this mismatch to accumulated error in the control-volume method, both as a result of the depth-invariant spreading assumption, and errors introduced into Du/Dt associated with the time variability of the flow. We therefore proceed with a focus on understanding the momentum balance within the plume ($z^* > -1$), the region where we have sufficient confidence in all of the terms in (3.6).

3.4.2 Assessing control-volume accuracy: all ebbs

To assess the general applicability of the control-volume method, we diagnose all terms in the momentum balance for each ebb transect of the 10 tidal cycles sampled (Figure 3.2). As a means of evaluating whether the near-surface deceleration is

captured by the measured stress divergence in the upper plume, we compare r_τ to τ, evaluated at the plume base (where both are typically maximum). The comparison is not particularly good (Figure 3.9), and is occasionally even negative, which is non-physical. τ varies by more than two orders of magnitude while r_τ has a much narrower dynamic range. The majority of r_τ estimates are $\approx 10^{-3}\mathrm{m}^2\mathrm{s}^{-2}$. These errors are most likely due to a combination of (1) error in individual transect estimates of $\vec{u} \cdot \vec{\nabla} u$ caused by real high-frequency/wavenumber variability, and (2) possible error or bias associated with plume-spreading assumptions (see Appendix for details).

3.4.3 Mean momentum balance

We now seek to quantify the momentum balance of the ebb outflow from the Columbia River mouth in an average sense. Due to the wide variability in internal stress, and the disagreement between r_τ and τ for low-stress cases, we divide these data into two sets: 1) a "high stress" set in which r_τ and τ are similar magnitude, and 2) a "low-stress" set in which the magnitude of r_τ is generally much larger than τ. In the following we investigate the internal balance for each of these cases.

3.4.3.1 High stress balance (peak ebb)

Figure 3.10 shows average profiles of velocity, acceleration, momentum and stress from the high τ transects (circled in Figure 3.9), which were generally associated

with the initial ebb pulse (i.e., the peak-ebb stage in Figures 3.3 and 3.4). These profiles show that during each of the high stress transects, the dynamic balance is similar to the example in Figure 3.8. The mean velocity profile is almost identical (Figure 3.10a) to that in the previous example (Figure 3.8a). Local deceleration, $\partial u/\partial t$, is positive throughout the water column, and largely barotropic on average (Figure 3.10b, magenta). Within the upper half of the plume ($z^* > 0.5$) more momentum is entering the onshore end of the control volume than exiting the offshore end, leading to positive $\vec{u} \cdot \vec{\nabla} u$ (b, blue). Below the plume, control-volume $\vec{u} \cdot \vec{\nabla} u$ roughly balances $\partial u/\partial t$. This results in a total acceleration profile that indicates parcels are decelerating strongly in the surface, yet negligibly at and below the plume base (Figure 3.10c, purple).

The Coriolis effect is weak compared to plume deceleration (c, black-dashed). As in the aug20b example, isopycnals are shoaling in the average, leading to a baroclinic pressure gradient that weakly accelerates the surface plume relative to the fluid below (c, vertical structure of green curve); however, $\partial P_{\mathrm{bc}}/\partial x$ is relatively weak in the mean. The depth-average pressure gradient is $-0.5\mathrm{m\,s^{-2}}$, which is sufficient to drive the observed barotropic local deceleration ($0.5\mathrm{m\,s^{-2}}$; Figure 3.10b magenta). The surface and bottom stresses are small compared to internal τ (d, red). Overlap of the 95% confidence intervals of r_τ and τ suggests that control-volume deceleration within the plume is accurate for these cases. The stress divergence, $\partial\tau/\partial z$, is the dominant force in the balance (c, red). The internal stress fluxes offshore momentum from the upper two-thirds of the plume downward, where it is deposited at the plume base. As in the example, in sec-

tion 3.4.1, the control-volume method does not capture the input of momentum implied by the observed stress divergence at $z^* = -1$ (c, purple). This results in disagreement between r_τ and τ below the plume base.

3.4.3.2 Low stress balance (mid/late ebb)

In the remainder of the ebb transects, the observed turbulent stress was up to a factor of 10 smaller than that in Figure 3.10d, producing a stress divergence insufficient to close the momentum balance (as quantified by a comparison between τ and r_τ; Figure 3.9). These low-stress transects generally corresponded to the mid- and late-ebb stages, characterized by flows that were thinner and more horizontally-uniform; mean profiles of terms in (3.6) for these cases are shown in Figure 3.11.

The mean velocity has a similar shape but is 25% weaker than that of the high-stress cases (compare Figure 3.11a to 3.10a). As a result, plume advection ($\vec{u} \cdot \vec{\nabla} u$) is almost 50% weaker than in Figure 3.10b. However, the time dependence in the low-stress cases ($\partial u/\partial t \approx 0.8 \mathrm{m\,s^{-2}}$), is larger than in the high stress cases (compare magenta lines in Figures 3.10b and 3.11b). Again, because this deceleration is constant with depth, we associate it with the barotropic tide. The control-volume estimate of the pressure gradient encourages this interpretation; the surface pressure gradient is statistically different from 0, and similar magnitude to $\partial u/\partial t$ (Figure 3.11c, green). That fact that $\partial P/\partial x$ shows little vertical structure indicates that the baroclinic pressure gradient is negligible in the low-stress cases

(i.e. isopycnals are horizontal during mid- and late-ebb).

In contrast to the high-stress balance (Figure 3.10), in these low-stress cases, the stress divergence is too small to balance the observed near-surface deceleration (Figure 3.11c; red versus magenta). This imbalance could be attributed to one of 3 factors: (1) variability associated with unresolved temporal or spatial features could be biasing our estimate of Du/Dt; (2) our depth-independent spreading assumption could be introducing error; or (3) because the plumes in Figure 3.11 tend to be thinner than those in Figure 3.10, it is possible we have failed to capture the strongest dissipation in these cases (or we incorrectly associated those ϵ with shipwake), so that the maximum stress and divergence was underestimated.

The internal stress divergence is still larger than the baroclinic pressure gradient (as seen by a lack of z-dependence in $\partial P/\partial x$, Figure 3.11c), and the surface and bottom stresses are smaller than the internal stress (d). Therefore, once again, these forces are considered to be unimportant in the momentum balance during our sampling.

One important contrast to the high stress balance, however, is that the Coriolis acceleration is now similar magnitude to the captured stress divergence (Figure 3.11c). We therefore suggest one of two balances for these cases. If the true stress was high in the region poorly-sampled by our profiler, then the balance could be the same as in the high-stress case: stress divergence balances deceleration. Alternatively, if the mismatch between control-volume deceleration and observed forces is due to accumulated error in the control volume technique, then numerous terms may be important: Coriolis, surface pressure gradient, and internal stress

divergence.

In either case, these findings indicate that the surface pressure gradient drives a local barotropic deceleration, and the vertical structure of plume deceleration is caused by internal stress (the Coriolis effect acts to weakly accelerate fluid). These results are consistent with mid- and late-ebb numerical model results of the Columbia River tidal plume, in which the surface pressure gradient and internal stress were the dominant causes of deceleration at the surface (*McCabe et al.*, 2009).

3.4.4 Plume deceleration

We now seek to understand the role of turbulent stress in decelerating the tidal plume as a whole. To do so, we compare the advective and stress terms in the momentum equation, (3.6). Scaling the advective term as, $\vec{u} \cdot \vec{\nabla} u \sim u \partial u / \partial x \sim u^2 / L_\tau$, and the stress term as, $\partial \tau / \partial z \sim \tau / h_\mathrm{p}$, we obtain a deceleration length scale due to the turbulent stress,

$$L_\tau = \frac{\langle h_\mathrm{p} \rangle \langle u \rangle_\mathrm{p}^2}{\langle \tau \rangle_\epsilon} \quad . \tag{3.11}$$

This gives an estimate of the length over which the observed stress will bring about a factor of e deceleration of the plume. In spite of the factor of u^2 in the numerator of (3.11), L_τ has an inverse dependence on u^2 (Figure 3.12), suggesting that plumes decelerate more rapidly for larger u^2.

We now compare L_τ to other important length scales of the plume. KN10 showed that the plume's Rossby radius, $L_\mathrm{R} = \langle c \rangle / f$, is similar to the length scale of the tidal discharge, $L_\mathrm{tidal} = (V_\mathrm{tidal} / \langle h_\mathrm{p} \rangle)^{1/2}$. In these expressions, c is the plume first-mode long-wave speed (i.e. Taylor-Goldstien wavespeed in the absence of shear) computed numerically from N^2 profiles (*Drazin and Reid*, 2004), and V_tidal is the total volume discharged from the estuary mouth during ebb. The shaded region in Figure 3.12 indicates the range of these two length scales.

During peak-ebb, plumes tended to be controlled by the high-stress momentum balance. At these times (solid symbols in Figure 12), L_τ estimates are similar to or less than L_tidal and L_R. This shows that internal stress can play a dominant role in decelerating the plume as a whole.

Later in the tidal cycle (mid- and late-ebb), plumes thin and the captured stress weakens. For these cases, L_τ estimates were greater than L_tidal and L_R, suggesting that the internal stress does not play a significant role in decelerate the plume at this time and location. For these periods it is likely that internal stress becomes more significant for these cases farther downstream as the plumes thin, but we have not investigated this.

3.4.5 Summary of momentum balances

We have identified two types of dynamical balances in the Columbia River outflow. These are distinguished by the magnitude of the internal stress at the plume base. In the first, high stress (peak ebb) momentum balance we observe that internal

stress divergence within the plume roughly balances fluid deceleration there. All other terms are weak by comparison (the surface and internal pressure gradients, the Coriolis effect, surface and bottom stresses). The fact the deceleration length scale, L_τ, is smaller or similar magnitude to estimates of plume extent (L_R and L_tidal) indicates that the internal stress divergence plays a major role in decelerating the plume for these high stress cases.

In the second, low stress (mid/late ebb) balance. The mean internal stress profile was an order of magnitude smaller than the high stress case. This resulted in the stress divergence profile being similar magnitude to the other terms in the balance. In this balance the surface pressure gradient is the largest term by a factor of two, but is likely to be biased high by errors in the control-volume method. Therefore, we propose that the low-stress case is likely to involve a balance between four terms: the surface pressure gradient, internal stress, Coriolis acceleration and fluid deceleration. However, the fact that L_τ was much larger than estimates of plume size indicates that none of these forces are exerting a force strong enough to decelerate the plume at this time and location. We hypothesize that as the plume thins turbulent stress divergence will begin to once again play a larger role, as with the Coriolis effect, but this is left for future work.

The barotropic tide is present in both balances. During high-stress (peak-ebb) transects, the offshore component of the barotropic tide (depth average of $-u$) is weakening slightly (Figure 3.10b, magenta). During low-stress (mid/late ebb) cases, this deceleration is larger (Figure 3.11b, magenta).

3.5 Plume turbulence

Having shown that the turbulent stress plays a critical role in decelerating the tidal plume, we now investigate the energy source of this turbulence. In particular, our goal is to determine the outflow conditions that distinguish high stress from low stress cases. We begin with a discussion of two-layer drag laws that have been used in previous studies (section 3.5.1). In section 3.5.2 we discuss a parameterization in continuously sheared and stratified flow.

3.5.1 Two-layer drag laws

Given the simplicity and availability of two-layer drag laws, a number of studies have applied these scalings to continuously sheared and stratified systems such as river outflows. Motivated by the scaling arguments of *Imberger and Ivey* (1991), MG04 suggest that $\tau = 2.4 \times 10^{-3}\, \hat{g}' h_\mathrm{p}$ is a representative scaling for the shear-driven turbulent stress at the mouth of the Fraser River. Here, $\hat{g}' = (\rho(0) - \rho(-h_\mathrm{p}))/\rho_\circ$ is the reduced gravity based on the density change between the surface and the plume-base. While the highest values of τ agree with this scaling in the current data set (Figure 3.13a), the stress measured was as much as 2 orders of magnitude less than that predicted via this scaling. Furthermore, the dynamic range in $\hat{g}' h_\mathrm{p}$ (a factor of 4) is far too small to explain the observed variability in τ and there is effectively no relationship between τ and $\hat{g}' h_\mathrm{p}$. This discrepancy may be attributable to h_p being the incorrect length scale of the turbulence, since the flow is not 2-layer. However, it is important to note that this scaling has not been previously tested

using direct turbulence observations, since MG04 based their results on the control-volume residual r_τ, not τ itself. As a result, their results had almost no dynamic range - needed to verify a relationship. The fact that, in our observations, r_τ has a similarly narrow dynamic range to $\hat{g}'h_\mathrm{p}$ compared to τ suggests that this parameterization may not have wide applicability.

An alternate scaling of plume turbulence based on the plume velocity squared, u^2, is presented in Figure 3.13b. This explains more of the variability in τ than $\hat{g}'h_\mathrm{p}$, but is still unsatisfactory; the dynamic range of u^2 is still too small by more than a factor of 10.

In the continuously sheared and stratified flow we examine here, the horizontal axis of panels a and b in Figure 3.13 are related by the Richardson number (i.e. $\hat{g}'h_\mathrm{p} \propto Ri\,u^2$). Therefore, the fact that there is a difference between these two variables indicates that there is variability in Ri^{-1} (Figure 3.13c). Furthermore, the fact that τ is somewhat related to u^2 (a), and unrelated to $\hat{g}'h_\mathrm{p}$ indicates that the turbulent stress is more strongly controlled by velocity (or shear) than stratification. However, we note that our stress estimates omit the upper 4m of the plume, and it is possible that this has led to some of the disagreement in Figures 3.13a and b.

However, since we find our stress estimates to be highly correlated to Ri^{-1} (Figure 3.13c), it is likely to perform better than either $\hat{g}'h_\mathrm{p}$ or u^2. Perhaps more importantly, the vertical structure of the Columbia River outflow is continuously sheared and stratified, not two-layer (Figure 3.5). We hypothesize that much of the discrepancy between observed and parameterized τ in Figure 3.13 may be resolved

by considering a parameterization based on continuous shear and stratification.

3.5.2 Continuous shear and stratification

In continuously sheared and stratified flows such as these, S^2 and N^2 are the more natural variables of turbulence parameterization. Following *MacKinnon and Gregg* (2003), we explore the variability of ϵ in S^2-N^2 space, with the understanding that τ is related to ϵ. As illustrated in Figure 3.14a, the highest dissipation rates are associated with unstable Ri, consistent with the profiles shown in Figure 3.5, which are often unstable on average. For solibores on the New England Shelf, *MacKinnon and Gregg* (2003) found the kinematic parameterization of *Kunze et al.* (1990) to roughly replicate the observed ϵ in patches where unstable Ri was resolved. Kunze et al's model represents ϵ as the amount of energy released in returning a unstable patch of fluid to $Ri = 0.25$, divided by the timescale for instability:

$$\epsilon_{\mathrm{KWB}} = \delta^2 \frac{(S^2 - 4N^2)(S - 2N)}{96} \tag{3.12}$$

for $S^2 > 4N^2$ and 0 otherwise (Figure 3.14b). In the region of unstable Ri, which represents much of the plume, ϵ_{KWB} has similar magnitude and dependence on excess shear squared $(S^2 - 4N^2)$ as in observed ϵ. A downside of this parameterization is that it is unable to predict ϵ in the Ri-stable regions of the flow, which are still moderately dissipative.

A subtle aspect of this scaling is choosing the appropriate vertical length scale

of instability, δ. *Kunze et al.* (1990) state that δ is the distance over which the flow is unstable ($Ri < .25$) at the time the instability begins to grow. However, obtaining an estimate of this length in a flow that is already turbulent is not straight-forward. As illustrated by Figures 3.3e,3.4e,3.5e, the plume is often unstable over a significant fraction of h_{p}, suggesting this as an upper bound on δ. However, the scales of the resultant instabilities, as defined by a Thorpe or turbulent Ozmidov scale are much smaller, $O(10cm)$ (not shown). As a practical solution, we fit ϵ_{KWB} to observed ϵ, within the plume, and find that $\delta = h_{\mathrm{p}}/2.7$. While we have no dynamical justification for this value of δ, this parameterization provides good agreement with observed ϵ (Figure 3.14).

Given the agreement between ϵ_{KWB} and observed ϵ, we use ϵ_{KWB} in (3.4) to obtain an estimate of stress at the plume base:

$$\tau_{\mathrm{KWB}} = \frac{1}{1 - Ri_f} \frac{\epsilon_{\mathrm{KWB}}}{S} \qquad . \tag{3.13}$$

For each transect, τ_{KWB} was computed and averaged over the region of valid τ (i.e., the region of maximum stress in Figures 3.10 and 3.11). This gives reasonable agreement with observed τ over two orders of magnitude and during both high and low $\overline{Q_f}$ (Figure 3.15). In comparison to the parameterizations based on 2-layer flow (Figure 3.13), the skill of τ_{KWB} is encouraging. This agreement suggests that, 1) it is necessary to consider details of the shear and stratification to be able to predict ϵ or τ, and 2) these quantities scale with the excess shear, $S^2 - 4N^2$. The reasons for such large dynamic range in excess shear is explored next.

3.5.3 External forcing

The dependence of (3.12) on $S^2 - 4N^2$ represents two important components of turbulence generation by Kelvin-Helmholtz instability: 1) its intensity scales with the magnitude of S^2, and 2) unstable $Ri^{-1}(> 4)$. The magnitude of S^2 is important because for a particular unstable value of Ri^{-1} (e.g. 5) τ_{KWB} will increase with increasing S^2. Agreement between τ_{KWB} and τ suggests that S^2 and N^2 are important to turbulence generation in the Columbia River tidal plume system, but it does not indicate the sources of their variability. In particular, we would like to know what factors control these components and cause some ebbs to be high stress and others low stress?

The first component, S^2 magnitude, is partially controlled on long time-scales by changes in river flow, $\overline{Q_f}$. As $\overline{Q_f}$ increases N^2 increases causing the outflow to thin, thereby increasing S^2. Spring-neap variability in estuary mixing can also alter N^2 and S^2 in a similar manner; weaker mixing during neap tides (compared to spring) raises N^2, lowers h_{p}, and raises S^2 of the Columbia River outflow (*Jay and Smith*, 1990a; *Nash et al.*, 2009). On shorter timescales, the strength of shear within each ebb pulse is controlled by the peak tidal velocity; *Nash et al.* (2009) show that maximum u and ϵ depend on the strength of each tidal pulse.

The second component, Ri^{-1}, is observed to have a significant amount of variability and be strongly correlated with τ (Figure 3.13c). In addressing what drives this variability we point out the large variability in tidal amplitude, $\Delta\eta$, at the Columbia River mouth (Figure 3.2b) and hypothesize that higher τ and Ri^{-1} occur

during larger tides. Figure 3.16 shows that larger ebbs have larger Ri^{-1}. This suggests that more excess shear-squared, $S^2 - 4N^2$, is available during large ebbs than smaller ones. Figure 3.16b shows a rather sensitive dependence of internal stress on tidal amplitude: large ebbs ($\Delta\eta \approx 3$m) are all "high stress" ebbs. τ is normalized by c^2 to account for changes in N^2 associated with higher $\overline{Q_f}$. Given that $\Delta\eta$ is independent of plume-base τ, this demonstrates that larger tidal amplitudes force stronger S^2 relative to N^2 and therefore higher τ.

Therefore, from ebb to ebb, $\Delta\eta$ is a proxy for whether the outflow will be high or low stress. On longer timescales, seasonal changes in $\overline{Q_f}$ and spring-neap variability in estuary mixing can alter the value of τ during these high τ ebbs. The interpretation then is that on long timescales, the estuary mixes and adjusts toward a critical value of Ri^{-1}. For each tidal cycle, however, ebb-amplitude controls how super-critical the outflow will be, and therefore how important stress will be in the dynamics. Large ebbs which force more fluid out of the estuary mouth than the estuary stratification can support sub-critically, will be super-critical and τ will play a significant role in their deceleration.

3.6 Conclusion

The internal structure and evolution of the ebb outflow within 9km of the Columbia River mouth has been presented during two periods of distinct $\overline{Q_f}$. This outflow was described in terms of five stages: pre-front, front, peak-ebb, mid-ebb and late-ebb. This paper focused on the peak- and mid-ebb stages. During peak-ebb, u,

h_{p} and ϵ were maximum. As ebb progressed, plumes thinned and became less energetic.

During low river flow (August 2005, $\overline{Q_f} \approx 4000\mathrm{m}^3\mathrm{s}^{-1}$), large estuary discharge velocities in the presence of modest stratification forced super-critical Ri^{-1} and high ϵ throughout the water column. During high river flow (May 2006, $\overline{Q_f} \approx 12,000\mathrm{m}^3\mathrm{s}^{-1}$) plume N^2 was higher, which supported higher S^2, thinner h_{p}, and even higher ϵ. These observations were used to quantify terms in the outflow momentum balance under these two river flow conditions as well as large and small tidal amplitude. Lateral spreading terms that could not be quantified directly from our transects along the plume-axes were estimated using a control-volume method similar to MG04.

We have presented two limiting cases of the plume momentum balance. In the first, high stress (peak ebb) momentum balance, the vertical turbulent stress divergence balanced plume deceleration. Momentum supplied near the surface from upstream was fluxed downward by the turbulent stress and deposited at the plume base. However, while this flow of momentum from near surface to plume base seems clear from our turbulence data, only the near-surface balance could be closed with the control-volume method. At the plume base, no localized acceleration was observed. Instead, the control-volume method distributed this as a residual stress-divergence over a broader depth range, that was balanced by a biased surface pressure gradient. This mismatch is most likely due to error in lateral spreading or misalignment of our transects with the mean flow. In these high stress cases the similarity of the magnitude of the deceleration length scale,

L_τ, and the external length scales, L_R and L_tidal, indicates that internal stress plays a major role in decelerating these plumes. This suggests that inviscid models of plume expansion (e.g. *Garvine*, 1984; *Kilcher and Nash*, 2010; *Jay et al.*, 2010) might be improved by incorporating frictional effects.

In the second, low stress (mid/late ebb) momentum balance, the internal stress divergence, Coriolis acceleration, and surface pressure gradient were all found to be similar magnitude. This agrees with the numerical model results of *McCabe et al.* (2009), who found that internal stress and the surface pressure gradient were the dominant forces decelerating the tidal plume. In the low-stress balance the control-volume estimate of deceleration was an order of magnitude larger than the force terms. This imbalance indicates that the control volume over-predicts plume deceleration. This is due to time-dependence of the outflow that is not included in the control-volume method.

In both balances the internal pressure gradient, as well as the bottom and surface stresses were insignificant terms. In the case of the surface stress, wind speeds were too low to impose a force of similar magnitude to the internal stress, even during the low stress cases. During periods of stronger winds than observed here ($\gtrsim 15\mathrm{m\,s^{-1}}$), it is likely that τ_s will play a significant role in the plume's momentum balance. Furthermore, winds will have an increasingly important role farther offshore where the plume is thinner, wider and less directly influenced by the discharge from the river mouth. Both balances are distinct from a similar analysis in the Columbia River estuary, in which the pressure gradient and internal stress forces were in balance (*Kay and Jay*, 2003).

We compared estimates of τ in the plume base to a pair of drag-law parameterizations of internal stress. The first, suggested by MG04 and motivated by scaling arguments of *Imberger and Ivey* (1991), was that τ should be proportional to $\hat{g}' h_{\mathrm{p}}$. We find this estimate to have no skill in predicting τ. The second parameterization we tested was whether τ was proportional to u^2. This had more skill than the first, but did not result in a constant drag coefficient (ratio of τ to u^2). This suggests that two-layer parameterizations of this sort are ill-equipped for estimating turbulent stress in continuously sheared and stratified plume outflows such as this.

Motivated by *MacKinnon and Gregg* (2003)'s finding that ϵ in solibores could be represented by *Kunze et al.* (1990)'s parameterization if unstable shear is resolved, equations (3.12) and (3.13) were applied to our data to estimate τ_{KWB}. Plume τ is well predicted by τ_{KWB} when the flow is super-critical ($Ri^{-1} > 4$), suggesting the importance of $S^2 - 4N^2$ in controlling plume base turbulence and internal stress. In addition, tidal amplitude, $\Delta\eta$, is a key parameter in controlling whether the flow is super-critical. During large ebbs, increased volume discharge from the mouth forces S^2 to increase above $4N^2$. This drives vigorous turbulence which produces a "high stress" momentum balance in the plume. During weaker ebbs $Ri^{-1} < 4$ and the ebb outflow at this location is stable and largely inviscid. In addition to this control by tidal amplitude, we suggest that $\overline{Q_f}$ can influence the value of τ by altering the magnitude of the excess shear-squared, $S^2 - 4N^2$. This idea is supported by the result that high-stress, high $\overline{Q_f}$ ebbs (may28b, may29b) have larger τ than any low $\overline{Q_f}$ ebb.

A number of recent works have suggested an important link between plume-base turbulence (stress, mixing) and lateral spreading. It has been known for some time that lateral spreading is an important component of the dynamics of river outflows. *Wright and Coleman* (1971) showed that lateral spreading of a buoyant outflow in the Mississippi river delta was related to the wavespeed of that flow. This was also found in the Merrimack River plume (*Hetland and MacDonald*, 2008). *Chen et al.* (2009) found that internal stress played a role in controlling the Merrimack River plume's initial expansion rate. The above results support the idea that lateral spreading and mixing are closely linked. The reasoning behind this concept is that thinning associated with plume spreading causes a plume to become unstable to shear-instability, which drives vertical mixing. This mixing causes a decrease in the plume wavespeed, which, in turn, causes a corresponding decrease in spreading (*Hetland*, 2010).

While these relationships are likely to be important in a complete theory of plume turbulence and spreading, their details are still unclear. This paper adds understanding to these concepts by showing that τ can play a dynamically significant role in the plume and that τ is related to $S^2 - 4N^2$. If spreading is driving $S^2 - 4N^2$ this suggests that it is also driving turbulent stress. The result that τ_{KWB} scales with $\Delta\eta$ might then suggest that plume spreading and thinning is related to tidal amplitude. A detailed analysis of the relationship between τ and spreading would therefore be helpful, and is left for future work.

This paper connects a significant degree of variability in the dynamics of the Columbia River outflow to key forcing parameters of the system. In particular,

we find that: 1) τ often plays an important role in decelerating the tidal plume at this location, 2) this τ is controlled by subtle differences between S^2 and $4N^2$, 3) these subtle changes are related to the amplitude of the tidal drop, $\Delta\eta$. This provides pioneering understanding of the role of turbulent stress in decelerating a tidally dominated estuary outflow.

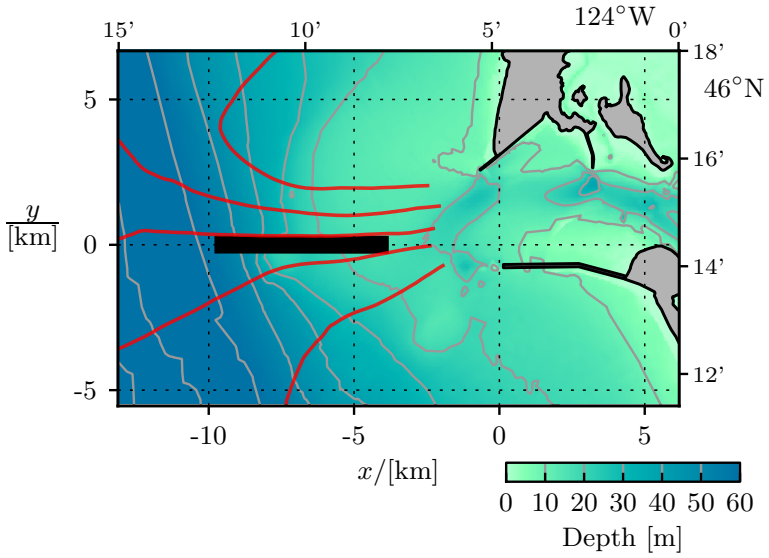

Figure 3.1: Chart of the NE Pacific Ocean at the Columbia River mouth. Depth contours in m. The thick black line indicates the location of "along-axis" sampling. The origin of the chosen coordinate system is just north of the tip of the south jetty. Positive x, u and y, v are eastward and northward (indicated at top and right), respectively. Red lines indicate paths of drifters released during the second ebb of August 9$^{\text{th}}$, 2005 [courtesy Ryan McCabe and Barbara Hickey].

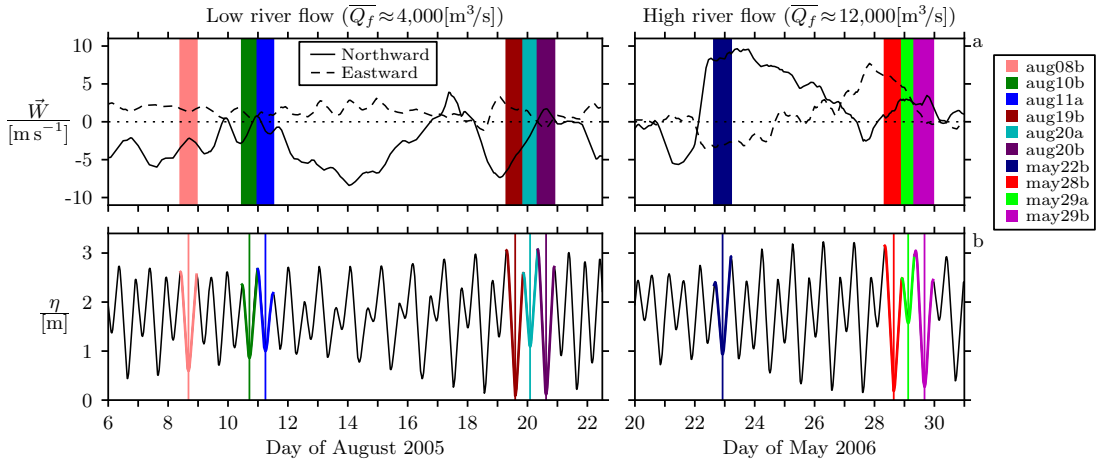

Figure 3.2: Environmental conditions at the Columbia River mouth during August 2005 and late May 2006. Panel (a) shows 10-hour low passed wind velocity from NDBC buoy 46029 (Columbia River bar). Panel (b) shows tidal height from xtide. Ebb time periods of along-axis sampling, in color, are indicated in the legend at right. Days are marked at the start of the UTC day.

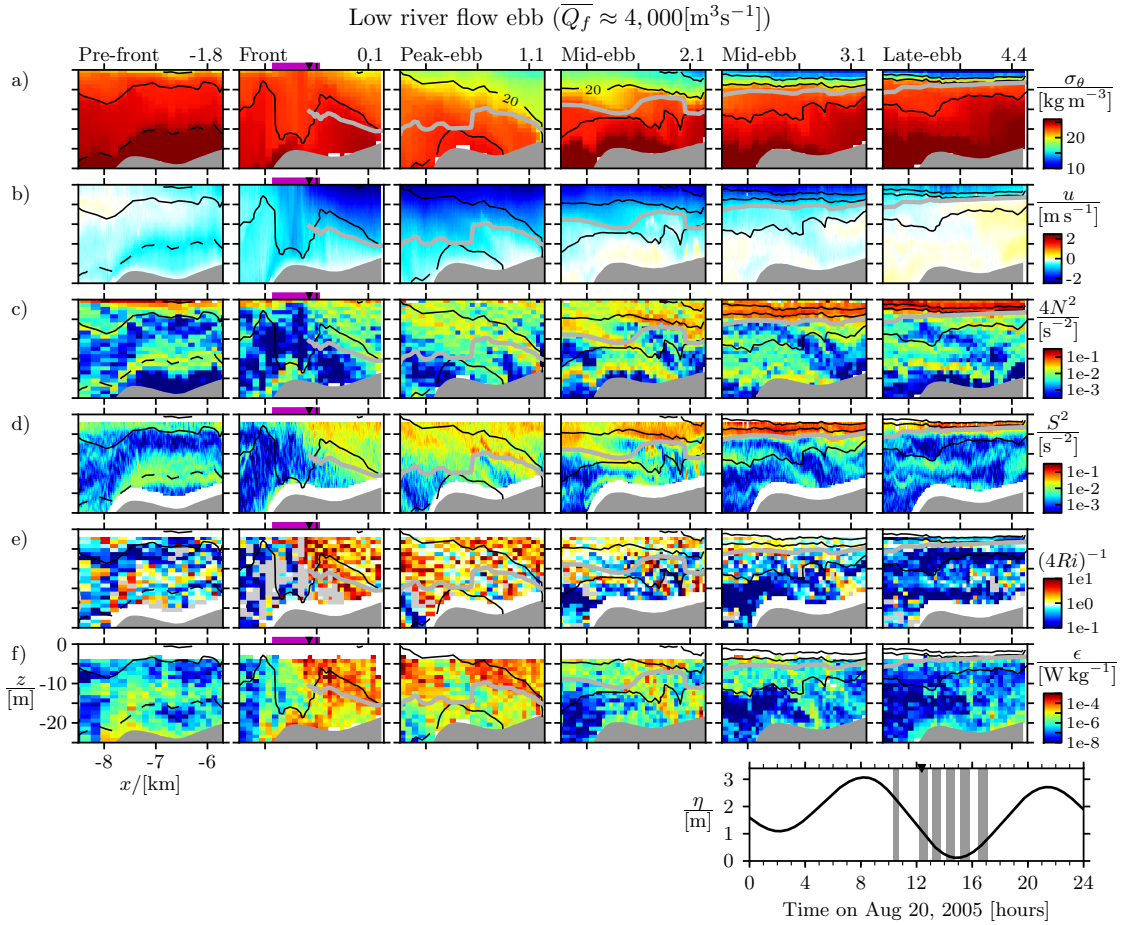

Figure 3.3: Time series of eastward transects through the low $\overline{Q_f}$ ebb aug20b (2005). Each column is a transect with time increasing from left to right. The time, in hours, that the ship crossed $x = -7$km, relative to the time the front crossed this location, is indicated at the top right of each column (transects are mostly 1hour apart). Rows show: a) potential density, b) is eastward velocity, c) squared buoyancy frequency, d) shear-squared, e) inverse Richardson number, and f) TKE dissipation rate. Black contours are 1016, 1020 and 1024kg m^{-3} isopycnals and thick grey lines indicate h_p. The dashed line in the pre-front column is the 1025.7kg m^{-3} isopycnal. The magenta bar and black triangle above panels in the front column mark the "frontal region" and x_f, respectively. In e, regions where N^2 was too low for Ri^{-1} estimates to be reliable are gray. The tidal height for the 32hours around this ebbs low is indicated in the panel at lower right. Grey bars indicate the time of each transect, and the black triangle indicates the time the front crossed $x = -7$km.

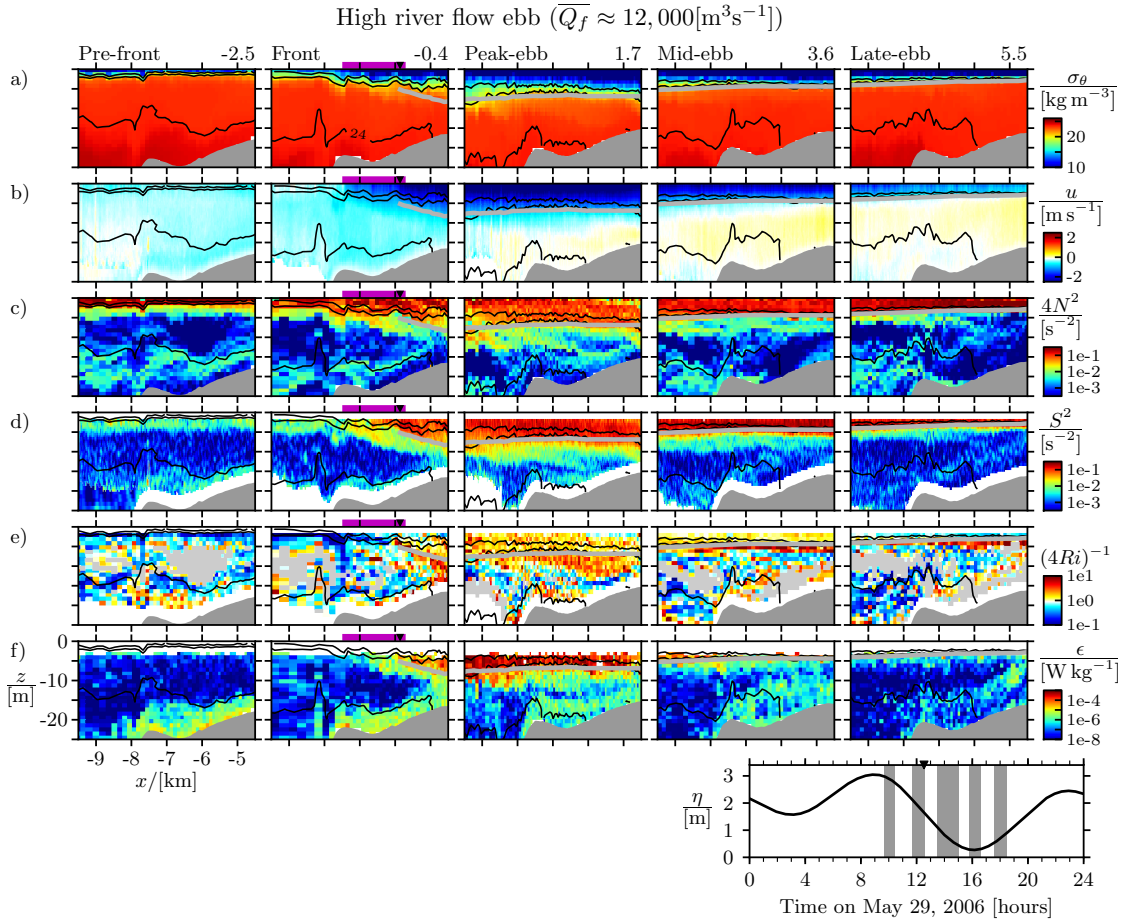

Figure 3.4: Time series of eastward transects through the high $\overline{Q_f}$ ebb may29b (2006). Transects are approximately 2hours apart. All panels and annotations are the same as in Figure 3.3.

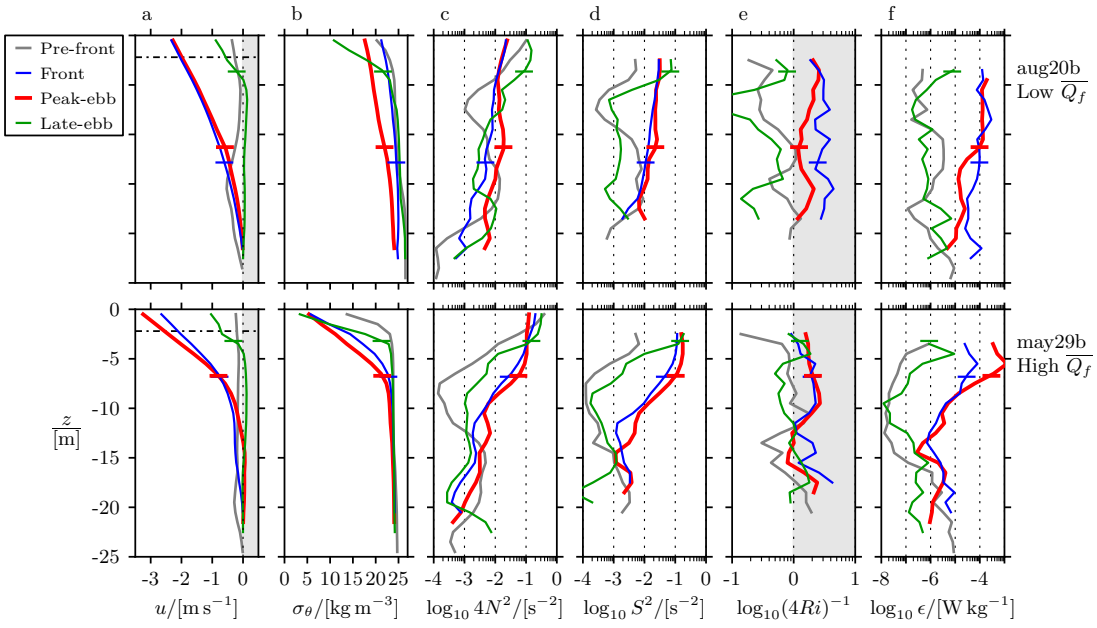

Figure 3.5: Average profiles during ebbs aug20b (low $\overline{Q_f}$, top) and may29b (high $\overline{Q_f}$, bottom). The profiles are taken as the average over the range $-7 < x < -6$km, except for the "front" profiles, in which the average is over the 1km inshore of the frontal region. From left to right, panels show velocity (a), density (b), 4× squared buoyancy frequency (d), squared shear (c), 4× Richardson number (e) and ϵ (f), during ebb aug20b. A horizontal tick across the "Peak-ebb" and "Late-ebb" profiles indicate h_p. In panel (a), the shaded region indicates onshore velocities, and the dash-dot line the depth above which velocity was extrapolated. In (e), the shaded region indicates super-critical Ri.

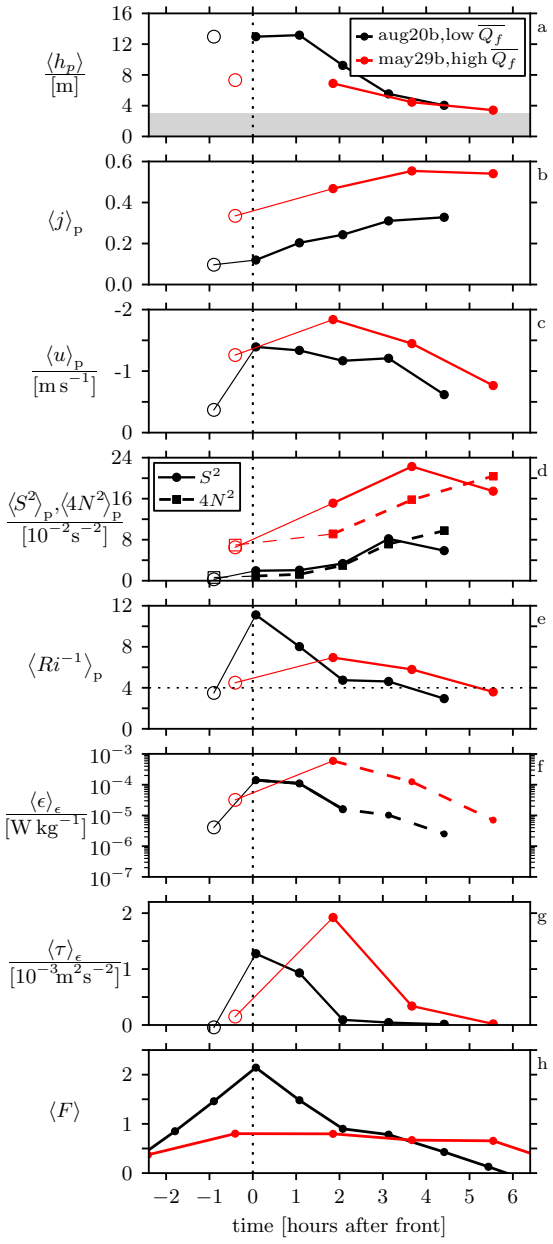

Figure 3.6: Evolution of plume averaged quantities during ebb of aug20b (black) and may29b (red). The panels are: a) plume thickness, b) freshwater fraction, c) fluid velocity, d) S^2 and $4N^2$, e) inverse Richardson number, f) TKE dissipation rate, g) Froude number, and h) internal stress. Open symbols in b-f,h are the average of each quantity over the initial plume thickness (open circle in a). The shaded region in (a) indicates the region where profiler tilt was too high to estimate ϵ. In (f) the line is dashed where ϵ estimates were made in less than 40% of the plume.

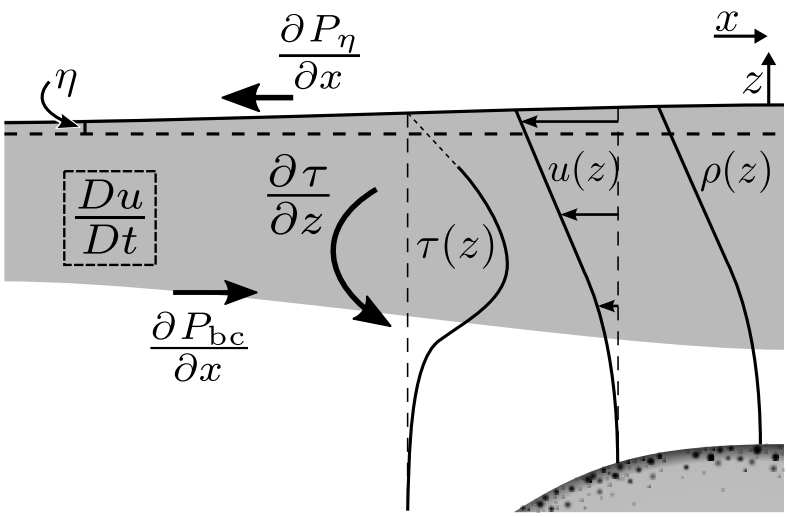

Figure 3.7: Diagram of plume and terms in the plume momentum equation. The grey shaded region represents light plume fluid flowing to the left. The speckle-shaded region marks the bottom. Schematic profiles of turbulent stress, velocity and density are on the right. Forces are indicated by line arrows. Imbalance in the forces will cause acceleration. The Coriolis effect is not indicated in the schematic.

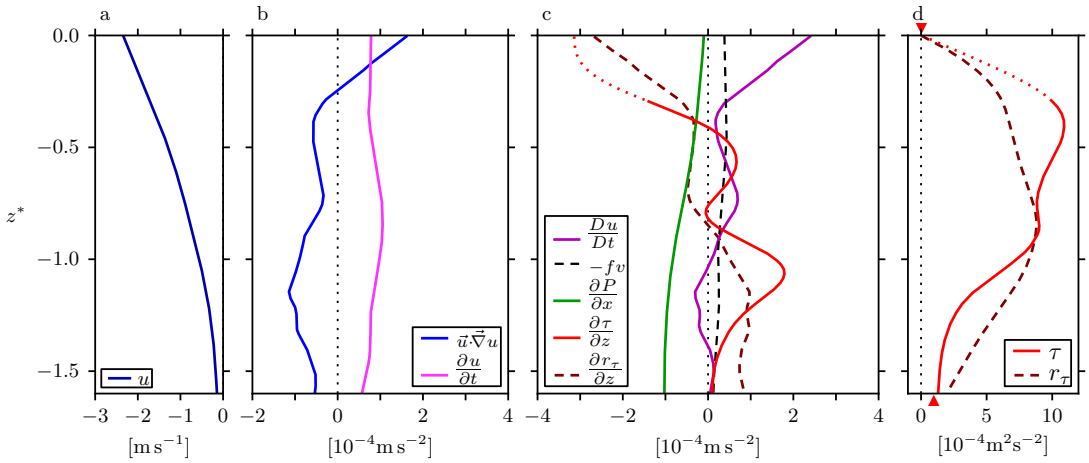

Figure 3.8: The u momentum balance during peak-ebb of aug20b (Figure 3.3c), versus scaled depth. Each profile is an average across the transect. a) Horizontal velocity, u. b) Components of the total cross-shore acceleration. c) Vertical structure of cross-shore momentum balance. d) Internal stress, τ, and control-volume residual-stress, r_τ. Red triangles at the top and bottom of (d) indicate τ_s and τ_b, respectively. In c and d, the dotted red line indicates the region where τ is interpolated between τ_s and the nearest-surface value. The τ profile is smoothed with a 2.5m-half-width triangle filter.

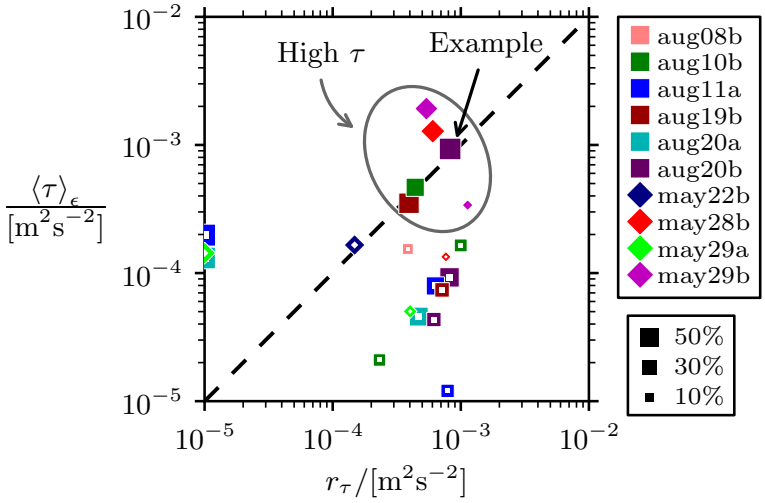

Figure 3.9: Measured turbulent stress versus that required by the control-volume method. Each point is from a single transect during an ebb (upper legend). Marker area is proportional to the fraction of the plume in which ϵ was resolved (lower legend). τ estimates greater than $3{\times}10^{-4}\,\mathrm{m^2 s^{-2}}$ are circled, lower values have a white center. Three data points on the left edge of the plot have negative r_τ. A black arrow marks the point corresponding to the "example" transect of section 3.4.1.

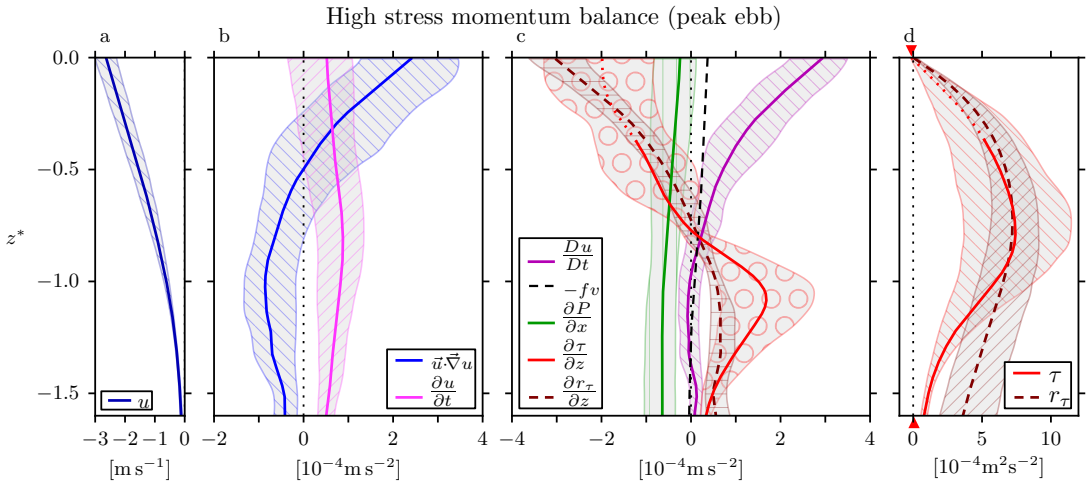

Figure 3.10: Terms in the u momentum balance, ensemble averaged over high τ transects, versus scaled depth. The terms are the same as in Figure 3.8. Shading about each profile indicates the 95% boot-strap confidence interval of the ensemble.

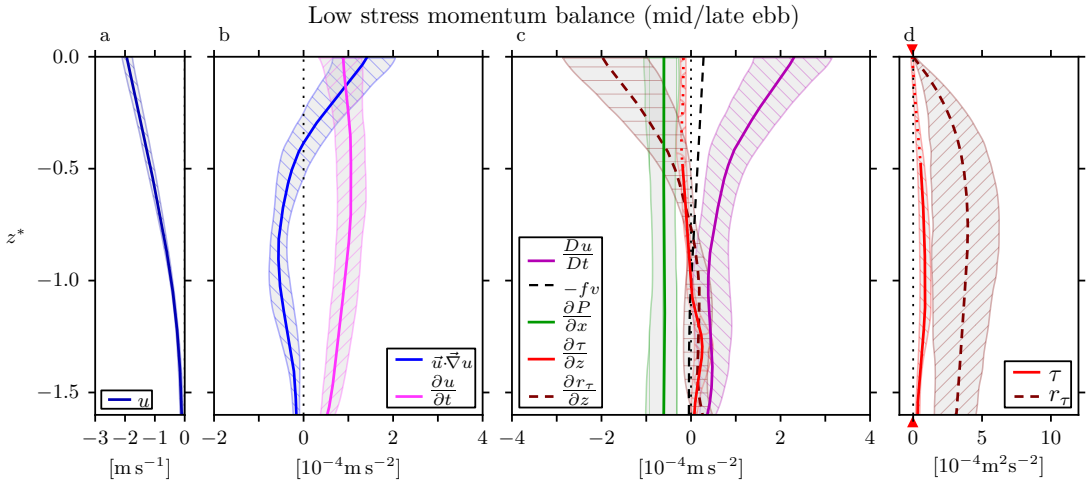

Figure 3.11: Terms in the u momentum balance, ensemble averaged over low τ transects, versus scaled depth. All panels are as in Figure 3.10.

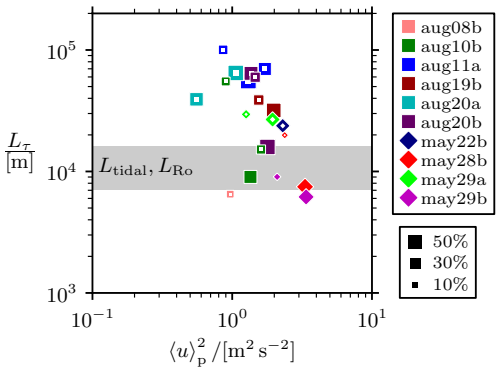

Figure 3.12: Plume deceleration length scale, L_τ vs. u^2. The shaded region indicates the range in the tidal length scale and the Rossby radius. Markers are as in Figure 3.9.

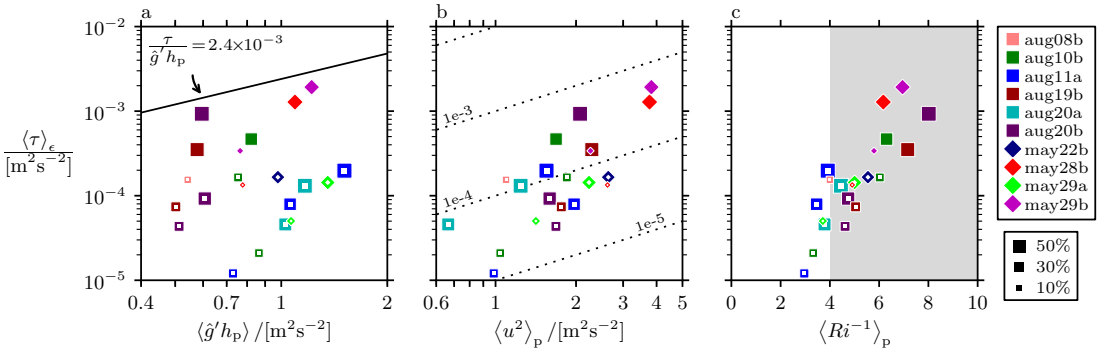

Figure 3.13: Plume averaged τ versus a) $\hat{g}' h_{\mathrm{p}}$, b) u^2, and c) Ri^{-1}. In panel (a), the solid line indicates MG04's estimate. Dotted lines in panel (b) indicate constant ratios of τ to u^2 (drag coefficient). In panel (c), the shaded region indicates unstable Ri^{-1}. The horizontal axis of panels a and b, as well as the vertical axis of all three panels are base-10 logarithmic. Markers are as in Figure 3.9.

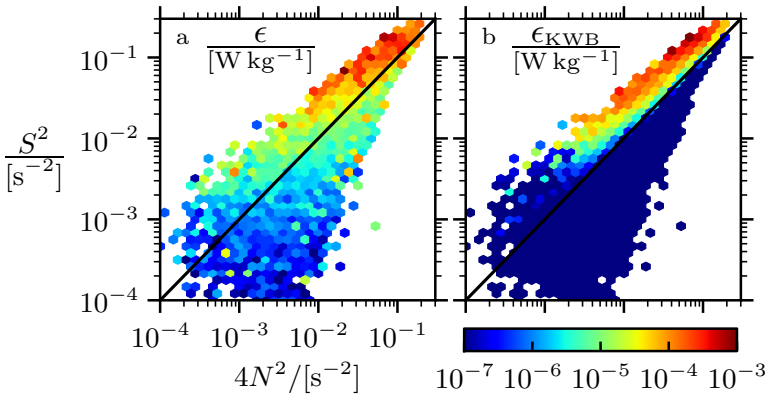

Figure 3.14: Average ϵ (a), and $\epsilon_{\rm KWB}$ (b) in hexagonal, logarithmically spaced, S^2 and $4N^2$ bins (12 bins per decade) for all eastward transects in which $\langle h_{\rm p}\rangle > 4$m. The black diagonal line indicates $Ri = 1/4$. In (b) $\delta = h_{\rm p}/2.7$.

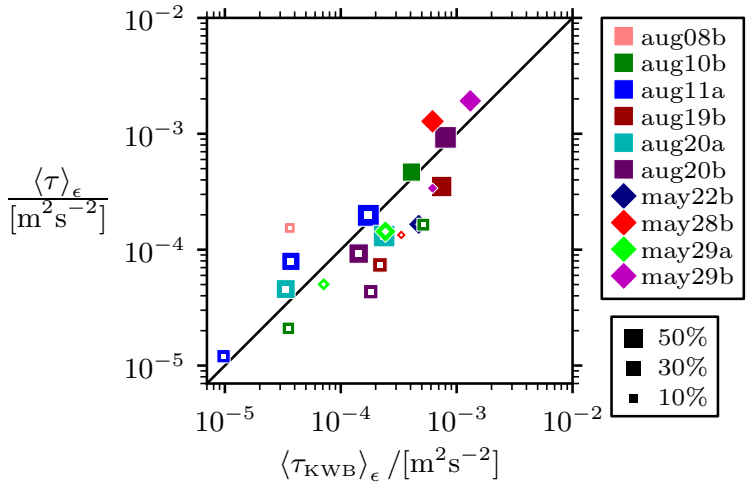

Figure 3.15: Plume averaged τ versus $\tau_{\rm KWB}$. Markers are as in Figure 3.9.

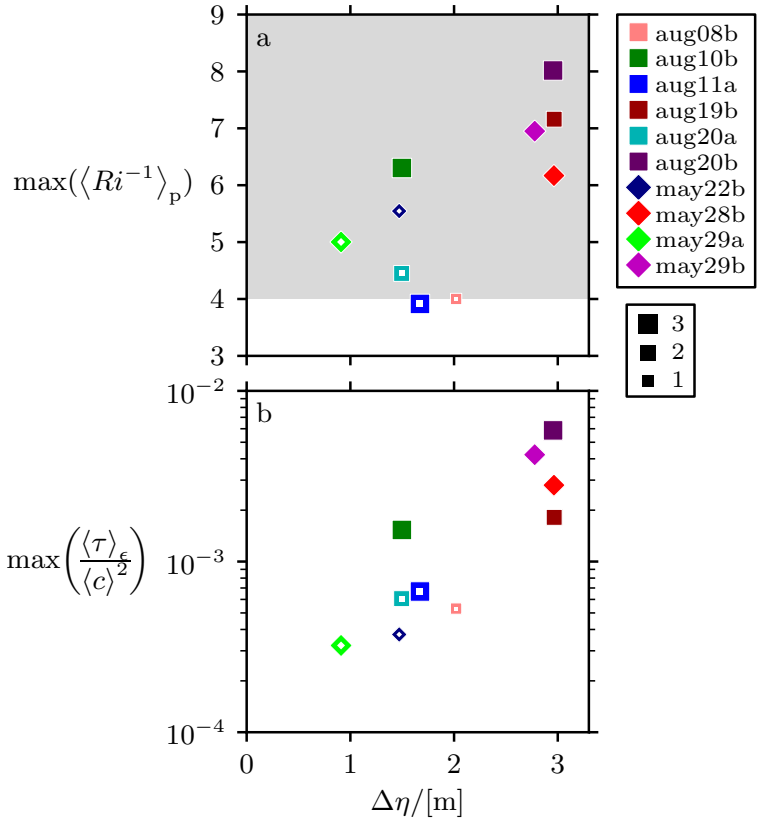

Figure 3.16: Maximum during each ebb of, $\langle Ri^{-1}\rangle_p$ (a), and $\langle\tau\rangle_\epsilon / \langle c^2\rangle$ (b) versus tidal amplitude, $\Delta\eta$. Marker color indicates tidal cycle (upper legend); marker size indicates the number of transects in the maximum operation (lower legend). Markers with white centers were identified as being "low-stress" ebbs.

Chapter 4 – Conclusion

This dissertation has investigated the dynamics of the Columbia River tidal plume and its front. Chapter 2 presented a detailed investigation of the plume front's structure and propagation. Fronts first form near the river mouth where super-critical discharge causes intense surface velocity convergence. As the buoyant discharge strengthens, the plume expands and the front propagates with frontal Froude number (F) in the range $1 < F < \sqrt{2}$, indicating it is a gravity current (*Benjamin*, 1968; *Britter and Simpson*, 1978). In the final stages of the plume's evolution, discharge from the mouth weakens and plume fluid inshore of the front is turned to northward by the Coriolis effect. It then becomes a part of the next regime in the Columbia River plume system: the re-circulating "bulge" (*Horner-Devine*, 2009). This demonstrates that frontal expansion is controlled by the time-dependent discharge through the river mouth.

Chapter 3 described the evolution of the ebb discharge near the river mouth during both high and low river flow, and investigated the momentum balance of the plume. It was found that after the front passes, the plume decelerates continuously. Internal stress was the dominant term in the outflow momentum balance during large ebbs, particularly during high river flow.

In section 4.1 I discuss what might have been different about these results during historical river flow rates (section 4.1). In section 4.2 I suggest how our

results may be applied to other river systems that have similar dynamics to the Columbia River.

4.1 Historical river flow rates

It is interesting to consider what the Columbia River outflow might have looked like prior to flow regulation by dams. As noted in chapter 1, damming has moderated the river flow, $\overline{Q_f}$: spring (peak) $\overline{Q_f}$ is not as high, and summer (low) $\overline{Q_f}$ not as low compared to pre-regulation. Chapter 3 showed that higher $\overline{Q_f}$ causes outflow stratification to increase, resulting in a thinner plume with stronger shear. It seems reasonable to presume that the larger pre-regulation discharge rates would simply amplify these effects.

During pre-regulation spring $\overline{Q_f}$ periods ($\overline{Q_f} \gtrsim 25,000 \mathrm{m}^3/\mathrm{s}$), freshwater velocities would have exceeded tidal velocities and the estuary would have been more strongly stratified (a salt wedge). Our results suggest that this would further thin the plume and raise τ during large ebbs. Given that a factor of three change in $\overline{Q_f}$ caused maximum τ to double in our observations, another factor of two in $\overline{Q_f}$ might raise maximum τ by another 60%. Due to the dependence of increasing max τ (and therefore decreasing minimum Ł$_\tau$) for higher $\overline{Q_f}$ (Figure 3.12), we expect τ would have played an even more important role in decelerating large ebbs during pre-regulation high $\overline{Q_f}$ periods.

4.2 Relevance to other river systems

These results are likely to be relevant to other small-scale river discharges with strong tides. In order to assess the relevance of these results to other systems, it is useful to consider the characteristic properties of the Columbia River outflow. There are four relevant properties: 1) a narrow mouth, 2) super-critical discharge, 3) tidal pulsing, 4) estuary type. While some of these conditions are related, they each deserve a short discussion.

4.2.1 Narrow mouth

In the open ocean, the internal Rossby radius, $L_{\mathrm{R}} = c/f$, is the characteristic length scale of buoyant flows (c is the internal wavespeed of the plume or estuary and f is the Coriolis parameter). L_{R} represents the length scale over which horizontal density gradients can balance Coriolis acceleration. This scale is therefore used for determining the importance of Coriolis acceleration in bays or estuaries.

In coastal-plain estuaries such as the Columbia, the mouth width is often a representative value for the channel width within the estuary. This being the case, the ratio of the mouth width, W, to L_{R} indicates the importance of Coriolis acceleration at the mouth as well as within the estuary. This is the mouth Kelvin number, K_W. For $K_W \ll 1$, the flow upstream of the mouth is constrained by the narrow estuary and Coriolis acceleration is unimportant compared to steering and stirring of the flow by the channel. On the other hand, $K \gg 1$ indicates that Coriolis acceleration is important and a cross-channel density gradient should exist

within the estuary.

The value of K_W, therefore, is used to distinguish dynamically wide estuaries and river discharges from narrow ones. The Columbia Estuary, with $W \approx 3$km and L_R ranging from 6 to 10km (due to seasonal changes in river flow), has a narrow discharge ($K_W = 0.4 \pm 0.1$). Other small-scale river discharges include: the Merrimack (*Geyer et al.*, 2008, $K_W \approx 0.1$), the Fraser (*MacDonald and Geyer*, 2004, $K_W \approx 0.1$), the Connecticut (*Garvine*, 1974a, $K_W \approx 0.4$), the flow through south pass in the Mississippi river delta (*Wright and Coleman*, 1971, $K_W < 0.1$), and the outflow through "the cut" of Leschenault Estuary (*Luketina and Imberger*, 1987, $K_W < 0.1$). Additionally, because the Amazon discharges into the Atlantic Ocean within 1° of the equator it has $f < 2.5{\times}10^{-6}\,\mathrm{s}^{-1}$. Therefore, even though its outflow has similar wavespeed to the Columbia, ($c \approx 1\mathrm{m\,s}^{-1}$), the Amazon outflow L_R is $>$ 400km (*Geyer et al.*, 1991). Therefore, the $\approx$ 150km wide Amazon mouth is considered "small" by this measure ($K_W < 0.4$).

Pulsed discharges from wide mouths, such as the flow through the mouth of Chesapeake Bay, will tend to hug the right coastline (in the Northern hemisphere) (*Marmorino and Trump*, 2000), and are therefore unlikely to spread significantly. The relationship between estuary discharge and frontal propogation we presented in chapter 2 depended strongly on a radially spreading geometry. Our results are therefore unlikely to apply to wide-mouth systems in which spreading is expected to be limited.

4.2.2 Super-critical discharge

Garvine (1995) suggests that the characteristic velocity, u_d, of narrow discharges will often be larger than the wavespeed of the coastal region into which they emerge c_a (i.e. the Froude number, $F_d = u_d/c_a$, is expected to be greater than 1). This strong velocity, combined with the buoyancy of estuary fluid compared to ambient conditions, causes these outflows to expand laterally as they enter the coastal ocean. This expansion, Garvine notes, is a non-linearity in which "strong boundary fronts... will be possible" (*Garvine*, 1995). This helps make small-scale river outflows complex and dynamically interesting regions.

Fronts form where surface velocity convergence is large. At the Columbia River mouth, surface velocity convergence is large for $F_d > 1$. For sub-critical discharge ($F_d < 1$), regions of high surface velocity convergence (i.e. fronts) are unlikely to form because perturbations will disperse by wave propagation into the ambient environment. When $F_d > 1$, the fluid inshore of the convergence zone overtakes waves faster than they propagate, causing energy to accumulate in the front. Understanding that $F_d > 1$ is fundamental to front formation, and that existence of a front is crucial to the results presented in chapter 2, it seems reasonable to conclude that discharges with $F_d < 1$ will have quite different dynamics.

4.2.3 Tidal pulsing

Tidal pulsing is a defining characteristic of the Columbia River tidal plume. The result most dependent on this attribute, presented in chapter 2, was that discharge

time-dependence controls front propagation. The time-dependence of front propagation will therefore be different for estuaries with different estuary-discharge time-evolution.

Discharge buoyancy frequency squared, N^2, and shear-squared, S^2, both increased throughout ebb, and chapter 3 showed that the excess shear-squared, $S^2 - 4N^2$, drove strong turbulence in the plume. Time-dependence and lateral spreading are both likely to influence or control $S^2 - 4N^2$. However, further research is necessary to determine the precise roles of these two factors in controlling plume turbulence (*Hetland*, 2010).

In summary, discharge time-dependence clearly plays a controlling role in frontal propagation. It's role in controlling turbulent stress or mixing in the plume base is not as well understood and warrants further investigation.

4.2.4 Estuary type

Chapter 3 showed that internal stress depends on the magnitude of the excess shear-squared. It also shows that the inverse Richardson number, Ri^{-1}, has a similar range during both high and low river flow, and is strongly related to tidal amplitude, $\Delta\eta$. This compliments the results of *Nash et al.* (2009), in which the stratification, N^2 and thickness of the plume was found to be related to the estuary Richardson number, Ri_E (the ratio of horizontal advective to vertical turbulent fluxes of freshwater within the estuary). During high river flow, N^2 increases and the plume thins, causing larger plume velocity and shear-squared, S^2. This

relationship causes both high and low river flow periods to have super-critical $Ri^{-1} \approx 7$ during large ebbs. Because Ri^{-1} was similar and N^2 was higher, large ebbs had larger $S^2 - 4N^2$ during higher river flow, resulting in larger internal stress. The variability of excess shear-squared and internal stress observed in chapter 3 may be more observable in partially mixed estuaries where N^2 and plume thickness are variable. In salt-wedge estuaries, on the other hand, the magnitude of the stratification at the interface between the upper and lower layers may have less variability. This would suggest that $S^2 - 4N^2$ would have less variability, and therefore so would internal stress.

4.2.5 Summary of relevance to other river systems

The Connecticut River outflow is the most widely studied small-scale river discharge. Its $K_W \approx 0.4$ is also quite similar to that of the Columbia River outflow. A primary distinction between the Connecticut and Columbia River outflows is that cross-mouth tidal velocities at the Connecticut River mouth cause significantly larger plume deflection than we observe for the Columbia river tidal plume. This led Garvine to propose a frontal model which includes cross-mouth flow to maintain steady-state (*Garvine*, 1987). Such a model may not apply to the Columbia River tidal plume because it is not steady, and alongshore coastal currents are overwhelmed by discharge velocities. Instead we find that while frontal expansion can be limited by ambient currents, the tidal plume dynamics are dominated by the estuary discharge.

The Merrimack River discharge also has much in common with the Columbia. It is a narrow mouth estuary, with strongly tidal forcing. Furthermore, the outflow Froude number is super-critical, $F_d > 1$, suggesting that frontal formation is likely. It would be interesting, then, to estimate the time-evolution of the discharge rate through the Merrimack River mouth to see if there is a period of linearly increasing discharge, and if so, whether this corresponds to a period of constant frontal propagation and expansion, as was found for the Columbia (chapter 2), and the cut from Leschenault Estuary (*Luketina and Imberger*, 1987). The Merrimack estuary is much smaller than the Columbia, and it is a salt-wedge type estuary (*Geyer et al.*, 2008). During ebb of high river flow periods, freshwater flushes the entire estuary, until there is no salt water discharged from the mouth *MacDonald et al.* (2007). These differences might change the dynamics of the Merrimack, compared to those presented here for the Columbia River outflow.

Much of chapter 2 was based on a similar analysis of the outflow from "the cut" of Leschenault Estuary (*Luketina and Imberger*, 1987). In both rivers, linearly increasing estuary discharge feeds the expansion of a buoyant, radially spreading, super-critical plume. In agreement with theoretical considerations (*Chen*, 1980), the linearly increasing discharge causes the plume front to propagate at a roughly constant speed. Our findings are a significant addition to those of *Luketina and Imberger* (1987) for two primary reasons. First, it was not obvious a priori that the larger (by an order of magnitude) Columbia River tidal plume would obey similar dynamics to the smaller Koombana Bay plume. That it does indicates that these dynamics may apply to buoyant discharges of multiple scales, given a strongly tidal

estuary and a narrow mouth width (e.g.: the Merrimack River, *MacDonald et al.* (2007); the Fraser River, *MacDonald and Geyer* (2004)). Strongly tidal estuaries and narrow mouths compared to the Rossby radius . Second, we found that as the front's radius of curvature exceeds the plume's Rossby radius, expansion becomes limited by the earth's rotation.

Future studies which investigate the relationship between L_{R} and L would be intriguing. In particular, it would be interesting to know why L_{tidal} and L_{R} are so similar in both "the cut" of Leschenault Estuary and the Columbia River tidal plume, as compared to the Amazon in which L_{tidal} is surely much smaller than $L_{\mathrm{R}} \gtrsim 200\mathrm{km}$.

The primary conditions which are necessary for a system to have similar dynamics to those presented in this dissertation are that the outflow has a narrow mouth ($K < 1$), super-critical discharge ($F_d > 1$), and be tidally pulsed. If all three of these conditions are met, I would expect frontal propagation to be controlled by the time-dependent estuary discharge. If the estuary is also partially mixed, I expect turbulent stress at the plume base would be sensitive to the excess shear-squared, and might be related to tidal amplitude. More work is required to know the applicability of this relationship to salt-wedge type estuaries. In particular, does the mixing in the base of a discharge from a more two-layer (salt-wedge) estuary have similar dependence on excess shear-squared, or is there a limit to the applicability of this relationship?

4.3 Future work

In addition to the work presented here, two other important publications have already been based on the RISE microstructure dataset: *Nash and Moum* (2005) and *Nash et al.* (2009). There are a number of questions raised by this research that might be addressed using this same dataset; other questions will require further data collection. New field studies motivated by this research, as well as studies of the current dataset, are outlined below.

4.3.1 Lateral spreading and mixing

The most obvious and necessary investigation of this dataset that has not yet been undertaken is a study of plume spreading based on transects across the estuary mouth (lines 0 and 1 in Figure 2.1). A number of recent works (e.g. *Hetland and MacDonald*, 2008; *Hetland*, 2010) have suggested an important link between plume spreading and vertical mixing. As a plume thins, S^2 will increase more rapidly than N^2, causing Ri^{-1} to become super-critical so that shear (Kelvin-Helmholtz) instability is possible. On the other hand, turbulent mixing has the potential to reduce Ri^{-1}. Furthermore, plume spreading has been found to be related to the plume internal wavespeed *Wright and Coleman* (1971); *Hetland and MacDonald* (2008), suggesting that mixing also alters the plume spreading rate *Hetland* (2010). These ideas raise important questions about the role of spreading in controlling plume mixing, and vice-versa. However, few observational studies exist which capture both the plume spreading, and the turbulence in spreading

outflows. Some basic investigation of the data from the cross-axis transects might shed help considerably in addressing these questions.

In addition to this work, understanding of the Columbia River outflow momentum balance would benefit greatly from additional field studies that simultaneously captured the along-axis deceleration of the plume (as presented in chapter 3) and a robust estimate of lateral spreading. Two methods of resolving the plume spreading could be useful: 1) using drifters released at the mouth, and 2) from ship transects across the mouth. These two methods share the ability to capture the plume spreading, but have varying advantages and disadvantages. Ideally, a drifter study would release groups of drifters at 5 or more locations across the mouth. The scattering of drifters within each group could then be used to estimate horizontal diffusivity, so that lateral mixing could be compared with vertical mixing. Additionally, if drifters were released continuously throughout ebb (every 40min or so), the time-dependence of plume spreading could be quantified.

The other option, cross-axis transects, has the advantage of resolving not only the time-dependence of plume spreading, but the vertical structure as well. If these are made simultaneously to along-axis transects (from a separate ship), it is likely that the control volume method may work much better in closing the momentum budget of the outflow.

4.3.2 Surface turbulence

A significant improvement to the data collected for this dissertation would be estimates of water velocity and turbulent dissipation nearer to the surface. In particular, nearer-surface turbulence measurements would allow estimation of turbulent stress and mass diffusivity profiles. Such resolution of the stress profile would be useful in comparing the vertical structure of the stress profile during high and low stress periods (as discussed in chapter 3), as well as resolving the stress farther offshore where the plume is thinner. Because it is likely that stress varies significantly as the plume expands, resolving stress in a thinner plume is important to properly assessing its role on the plume as a whole. Such measurements might be made using an apparatus similar to the "measurement array for sensing turbulence" (*Geyer et al.*, 2008).

4.3.3 Far-field dynamics

Another piece of the RISE microstructure dataset worthy of investigation is the time period from May 25$^{\text{th}}$ to 28$^{\text{th}}$ 2006, when cross-shelf transects were made through the Columbia River plume downwelling coastal current. Prior to this time period, winds had been downwelling favorable and a northward geostrophic coastal-current had formed. There was a significant amount of tidal pulsing in the along-shore freshwater flux. We made 21 transects across the coastal current as northward winds relaxed.

The RISE microstructure dataset also includes 19 cross-shelf transects off the

Oregon and Washington coasts at 45.866N and 46.628N, respectively. A total of nine transects were made along the Washington line, and ten along the Oregon line. At least one of the transects in each location extended across the entire shelf, though most of them were made over distances of approximately 20-30km. Because these data include turbulence measurements, they are likely to be useful in assessing the vertical diffusivity in the far-field plume.

4.4 Concluding remarks

Richard W. Garvine spent the majority of his career studying river outflows. In *Garvine* (1995) he proposed a classification system for them "similar in spirit" to estuary classification (e.g. *Hansen and Rattray, Jr.*, 1966). He classified various buoyant flows by their Kelvin number (the ratio of their cross-shore length scale to their Rossby radius). However, his dissatisfaction that this system requires "a priori knowledge of the critical property and length scales" is apparent in his closing remark,

> It would be preferable to have a system that required only bulk properties of the discharge source region, such as initial flow speed and width. But such a system must await our acquiring *greater understanding of buoyant discharge physics, including mixing dynamics*, than is currently available. (*Garvine*, 1995, emphasis added)

This dissertation contributes significantly to our understanding of both mixing dynamics and buoyant discharge physics by relating the dominant flow patterns

of the Columbia River outflow to estuary and tidal forcing. My hope is that these results will contribute to the feasibility of the classification system Garvine sought and thus to a better understanding of river-ocean mixing and the hydrologic cycle.

APPENDICES

Appendix A – Front Identification

Published as Auxiliary, online, material to Chapter 2

Structure and dynamics of the Columbia River tidal plume front

Kilcher, Levi F. (College of Oceanic and Atmospheric Sciences, Oregon State University, Corvallis, OR, USA)

Nash, Jonathan D. (College of Oceanic and Atmospheric Sciences, Oregon State University, Corvallis, OR, USA)

Journal of Geophysical Research, Vol. 115, 2010, doi:10.1029/2009JC006066

Introduction

The auxiliary material listed below contains the methods used to identify the fronts in the above published manuscript. These methods are important to the accurate reproduction of the results therein.

Front Identification

During each transect[1] across a front one of three methods was used to identify its location, x_f. When fronts were simple and distinct these methods produced identical results. However, when frontal structure was complex these methods produce different results. In order to address this issue, ambiguity ranges were assigned subjectively to include all reasonable x_f estimates for each front realization. These ambiguity ranges were then used to estimate front speed error.

This identification scheme produces front location estimates, $x_f(t)$, that are inherently irregularly spaced in time. In some cases two realizations are so closely spaced in time, and their ambiguity so large, that they can not be considered independent estimates of x_f. Where this occurred the point, of the pair, with the larger ambiguity was dropped from the $x_f(t)$ series.

Due to its imprecision and ambiguity, radar backscatter alone was not used to determine x_f. However, in addition to providing estimates of front orientation, radar backscatter was used to validate internal estimates of x_f. When a band of

[1] A transect is defined as a period of time ($>$ 10minutes) during which the ship traveled in a roughly constant direction ($\pm 10°$).

radar backscatter could be unambiguously associated with a realization of x_f, a movie of radar backscatter verified that subsequent realizations of x_f were associated with the same band of backscatter. This increases our confidence in the identification schemes outlined below.

Method 1: velocity convergence maximum (U_x)

This front identification method was based on near-surface velocity convergence, U_x. It is the preferred method due to its 100× higher precision compared to methods 2 and 3.

After transformation into our coordinate system and extrapolation to the surface (see main text), 1200kHz ADCP velocity estimates were filtered using a 7.5s by 1.5m running-median filter (5 bins horizontally by 3 bins vertically). Near surface velocity was taken from the upper-most resolved bin, i.e. $z = 2.35$m. This was then interpolated onto a regularly spaced x-grid, $U(t) \rightarrow U(x)$. In so doing, care was taken to exclude periods where the ship moved slowly (to avoid erroneous convergence peaks). This spatial series was running-median filtered at 200m to remove spikes in the series while preserving the sharp jumps that occur at fronts. Velocity convergence was then computed,

$$U_x = -\frac{\partial U}{\partial x} \qquad ,$$

and filtered using a 60m double-running boxcar (triangle). This produced a spatial-

series of velocity convergence whose maximum could often be identified as the front. In isolated cases, the second, or third largest U_x peak was associated with the front. In other cases, when the 1200kHz instrument malfunctioned, it was necessary to compute U_x from 300kHz ADCP velocity estimates[2]. These exceptions are indicated in Table A.1.

Method 2: salinity gradient maximum (s_x)

This front identification method was based on salinity gradients from near-surface Chameleon salinity, s. The front was identified as the location of maximum

$$s_x = -\frac{\partial s}{\partial x} \quad .$$

The depth bin (0.5 or 1.5m) from which s is taken is indicated in Table A.1.

Method 3: salinity threshold

The third front identification method identified the front at the location where near-surface salinity crossed a threshold value, K_s. These values, along with the Chameleon depth bin from which s is taken, are indicated in Table A.1.

[2] U_x was produced identically from 300kHz estimates as 1200kHz, except that the upper-most bin was centered at 4.57m (i.e $U(t) = u_{300}(z = 4.57\text{m}, t)$).

Secondary front and internal wave identification and other details.

Ebbs aug08b and aug09b had neither a secondary front nor did they radiate internal waves.

Prior to 0230 UTC during ebb aug21a only the primary front was identified (Table A.1). During the transect at 0245 a wave-like feature, offshore of the original front, was apparent where U_x was maximum. The secondary U_x peak was identified as the original front. During the next transect (0310 UTC) the lead wave was unidentifiable. During the next transect, due to malfunction of Chameleon and the 1200kHz ADCP, the lead wave was identified as the location of max(U_x) from the 300kHz instrument. The primary front was identified based on a clear frontal outcrop in the 120kHz Biosonics^{TM} acoustic echosounder (indicated in Table A.1 as "ECHO"). For all transects after 0430 UTC the lead wave was identified as the location of max(U_x).

During ebb aug21b, near 1600 UTC the front radiated a nonlinear internal wave. After this time the location of max(U_x) was identified as the lead wave and the primary front was identified as the location of maximum salinity gradient (Table A.1).

During the transect at 0430, the location of max(U_x) is coincident with surface salinity (0.5m) crossing a threshold value of $K_s = 23.2$. In subsequent transects the salinity threshold method, based on 0.5m salinity and $K_s = 23.2$ is used to identify this front. For transects after 0430, max(U_x) identifies the lead wave in a train of non-linear internal waves.

Ebb aug22b was the only ebb that had a clear secondary front (inshore of the primary front). This front was identified as the farthest onshore location where U_x exceeded 1.1e$-$3s^{-1}.[3] Initially, the primary front is the farther offshore feature identified in this manner. After 1600 UTC the offshore surface convergence peak was associated with an internal wave that the primary front had radiated. After 1400, front identifications were made away from $y = 0$. After front speeds were calculated from these realizations, their position was projected back to the x-axis using front orientation from the radar. Thus, as is the case for all other ebbs, x_f, is front position along $y = 0$.

For the front generated during ebb aug25b the lead disturbance (bolus then wave) was identified as the location of max(U_x).

[3]Except during the transects at 1500 and 1600 UTC, in which cases the U_x threshold was 2e$-$3 and 1.5e$-$3s^{-1}, respectively.

Table A.1: Method used to identify primary front location during each ebb (left column). The median time of the transect on that day (UTC, HHMM) is indicated for each realization. Just below this, the identification method is indicated. U_x indicates fronts identified by maximum surface convergence, and s_x indicates maximum salinity gradient. Numerals indicate the value of K_s used in the salinity threshold method.

aug08b	1400	1545	1715												
		U_x													
aug09b	1415	1515	1615	1700	1745	1815	1840	1915	2030						
	U_x	U_x‡		U_x											
aug21a	0005	0055	0115	0145	0225	0245	0310	0355	0440	0525	0615	0715	0810	0900	
	U_x					U_x†	25*	ECHO	25**						
aug21b	0315	1340	1405	1435	1610	1635	1705	1920	2050						
	U_x					s_x*									
aug21a	0135	0155	0215	0245	0430	0530	0700	0845							
	U_x					23.2*									
aug22b	1500	1555	1655	1745	1910										
	U_x††	U_x		26**											
aug25b	1610	1810	1940	2105	2150	2300									
				s_x**											

† The second U_x peak was identified as the primary front.
†† The third U_x peak was identified as the primary front.
‡ U_x was computed from 300kHz velocity data.
* Salinity was taken from the 0.5m Chameleon bin.
** Salinity was taken from the 1.5m Chameleon bin.

Appendix B – Control volume (accounting for lateral spreading)

As indicated in the text, the primary purpose of the control-volume method is to obtain an estimate of the $\vec{u} \cdot \vec{\nabla} u$ term in (3.6), in the presence of lateral spreading. The surface pressure gradient term depends on the control-volume method only because it is estimated as a remainder of terms that include $\vec{u} \cdot \vec{\nabla} u$. In this appendix we detail the steps for estimating $\vec{u} \cdot \vec{\nabla} u$ and $\partial P_\eta / \partial x$, as well as provide details of how other terms (that do not include spreading) are calculated within the context of the control-volume method.

The control-volume method is a box model in which lateral (i.e. y-direction) fluxes are constrained using a plume width function, b. The plume width is defined as the cross-plume distance between the lateral bounding surfaces of the plume across which fluxes of momentum, salt and mass are defined to be zero. Because the depth and time dependence of plume spreading are unknown and for simplicity, we assume that b does not depend on depth, $b = b(x)$.

The control-volume method involves integrating the freshwater, volume and momentum equations in two directions: 1) the y-direction from $-b(x)/2$ to $b(x)/2$, and 2) in the z direction from the ocean surface down to an arbitrary lower surface. Here we use the scaled depth surfaces, $z^* = \text{Constant}$, as the lower boundary of the control volume. x is left un-integrated so that gradients can be estimated explicitly from the data.

Use of the model requires that data inputs be along the plume's trajectory (the plume axis), and that the plume discharge is steady during the period of sampling. In order to approximate a flow snapshot data for a given transect were interpolated to the median time of each transect using the previous, current and subsequent transects as required. We use data in the range $-9 < x < -5$km for this analysis.

B.1 Plume spreading

The plume width, $b(x)$, is estimated using the control-volume freshwater conservation equation,

$$\int_{-d}^{0} jbu \, \mathrm{d}z = Q_f \qquad . \tag{B.1}$$

The integral is evaluated at the x-location of microstructure profiles. Assuming Q_f does not depend on x, $b(x)$ can be estimated as the best fit line that satisfies (B.1). For the example transect of section 3.4.1, this method gives an estimate of aug20b's spreading center $x_\circ = 0.8 \pm 1.5$km. This agrees with spreading estimates from drifter releases during ebb aug19b that estimate the plume spreading center 0.3km inshore of the mouth [R.M. McCabe and B. M. Hickey, personal communication].

The form of (B.1) weights the spreading estimate heavily in the plume, where j and u are large. This provides a reasonable estimate for spreading within the plume, but is a poor representation of lateral fluxes below the plume base. This is the primary reason the control-volume method does not apply below $z^* \approx -1$ (a

more detailed consideration of this issue is given in MG04's appendix B).

B.2 Vertical velocity

Assuming that b does not vary in time, the volume conservation equation is,

$$w(z^*) = \frac{1}{b}\left\langle \frac{\partial}{\partial x}\int_{h_p z^*}^{0} bu\,\mathrm{d}z \right\rangle \qquad . \tag{B.2}$$

This gives an estimate of the quasi-vertical velocity normal to z^* surfaces. Throughout this work, averages of x-gradients of a quantity $G(x)$, (i.e. $\left\langle \frac{\partial}{\partial x} G \right\rangle$) are estimated as the slope of the linear best fit to $G(x)$. This has the advantage of including all data in a transect in the estimate of the gradient (rather than a true average of a finite-difference, which is merely a difference of the endpoints).

B.3 Advective acceleration

Now that we have estimates of b and w we are prepared to estimate,

$$\vec{u}\cdot\vec{\nabla}u = \frac{1}{b}\frac{\partial bu^2}{\partial x} + \frac{\partial uw}{\partial z} \tag{B.3a}$$

$$= \frac{1}{b\,\langle h_p\rangle}\frac{\partial}{\partial z^*}\left\langle \frac{\partial}{\partial x}\int_{h_p z^*}^{0} bu^2\mathrm{d}z \right\rangle + \frac{1}{\langle h_p\rangle}\frac{\partial}{\partial z^*}\left\langle u(z^*)\right\rangle\left\langle w(z^*)\right\rangle \quad . \tag{B.3b}$$

Here, volume conservation has been used to rewrite $\vec{u} \cdot \vec{\nabla} u$ as momentum flux divergence (i.e. $\vec{u} \cdot \vec{\nabla} u$). The presence of b in the first term on the right hand side of (B.3) is the control volume's accounting of the unresolved lateral flux divergence term ($\partial vu/\partial y$). It arises after performing the control-volume y-integral. Note that the form of (B.3b) highlights the control-volume method. Each term is integrated from the bottom of the control volume to the surface, then averaged in the x-direction and re-differentiated vertically to give the acceleration profile.

The first term on the right hand side of (B.3) represents the change in momentum flux from one side of the box to the other, including the effect of spreading. The second term is the momentum flux through the lower boundary of the control volume by w. Though each of these terms are strongly dependent on the choice for the control-volume's lower boundary (in our case, z^*), this dependence cancels in their sum so that $\vec{u} \cdot \vec{\nabla} u$ is independent of the choice of lower boundary.

B.4 Pressure gradients

Estimating the baroclinic pressure gradient does not require the control-volume method. However, for consistency we estimate the internal pressure gradient in a similar, "control-volume integral, gradient along z^* surfaces, vertical derivative" manner,

$$\frac{\partial P_{\mathrm{bc}}}{\partial x} = \frac{1}{h_{\mathrm{p}}} \frac{\partial}{\partial z^*} \left\langle \frac{\partial}{\partial x} \int_{h_{\mathrm{p}} z^*}^{0} P_{\mathrm{bc}} \mathrm{d}z \right\rangle \qquad . \tag{B.4}$$

The surface pressure gradient, $\partial P_\eta/\partial x$, is estimated so that the depth-integrated momentum equation balances (with observed τ_s and τ_b applied as boundary conditions). The error in this term, therefore, includes the accumulated bias in all other terms. This includes error in the advective flux terms associated with unresolved lateral fluxes below the plume base. However, because the depth-integrated advective flux terms are dominated by fluxes within the plume, this is only a small error in $\partial P_\eta/\partial x$.

B.5 Control-volume error

The major source of error in the control-volume method is due to error in plume spreading estimates ($\partial b/\partial x$). This has three potential sources: 1) time-dependence of the outflow which can not be incorporated in the control-volume method causes error in $\partial b/\partial x$, 2) misalignment of our sampling with the plume axis and 3) inaccuracy of the depth-invariant spreading assumption.

The first source of error is caused by pulses of buoyant fluid or waves that passed through the domain. If such a pulse is sampled at the onshore end of the control volume, but not at the offshore end, (B.1) gives an overestimate of spreading. Including time-dependence in spreading estimates does not remove this bias because the advective timescale is shorter than the sampling interval. In other words, pulses passed through the domain before they could be sampled a second time and properly accounted for in a time-dependent freshwater equation. Interpolating u and s fields between transects helps smooth out these pulses, reducing the bias

they introduce, but not eliminating it. Averaging multiple transects together, as in Figures 3.10 and 3.11, further reduces this error in the mean, but does not help with individual transect estimates. In the second source of error, misalignment of the transect with the plume axis can bias spreading estimates because freshwater fluxes at one end of the transect are not along the same streamlines as the fluxes measured at the other end. Error introduced by the depth-invariant spreading assumption introduces error into the acceleration profile below $z^* \approx -1$.The questions of how plume spreading evolves in time and space, and what environmental factors influence it (e.g. $\overline{Q_f}$, tidal amplitude, wind) is left for future work.

Bibliography

Alpers, W. (1985), Theory of radar imaging of internal waves, *Nature*, *314*, 245–247.

Barnes, C. A., A. C. Duxbury, and B.-A. Morse (1972), *The Columbia River estuary and adjacent ocean waters*, chap. Circulation and Selected properties of the Columbia River effluent at sea, pp. 41–80, University of Washington Press.

Benjamin, T. B. (1968), Gravity currents and related phenomena, *Journal of Fluid Mechanics*, *31*, 209–248.

Berdeal, G., B. M. Hickey, and M. Kawase (2002), Influence of wind stress and ambient flow on a high discharge river plume, *Journal of Geophysical Research*, *107*(C9), 3130, doi:10.1029/2001JC000932.

Bowden, K. F., and R. M. Gilligan (1971), Characteristic features of estuarine circulation as represented in the Mersey estuary, *Limnology and Oceanography*, *16*(3), 490–502.

Britter, R. E., and J. E. Simpson (1978), Experiments on the dynamics of a gravity current head, *Journal of Fluid Mechanics*, *88*, 223–240.

Bruland, K. W., M. C. Lohan, A. M. Aguilar-Islas, G. J. Smith, B. Sohst, and A. Baptista (2008), Factors influencing the chemistry of the near-field Columbia River plume: Nitrate, silicic acid, dissolved Fe, and dissolved Mn, *Journal of Geophysical Research*, *113*, C00B02, doi:10.1029/2007JC004702.

Chant, R. J., S. M. Glenn, E. Hunter, J. Kohut, R. F. Chen, R. W. Houghton, J. Bosch, and O. Schofield (2008), Bulge formation of a buoyant river outflow, *Journal of Geophysical Research*, *113*, C01017, doi:10.1029/2007JC004100.

Chao, S.-Y., and W. C. Boicourt (1986), Onset of estuarine plumes, *Journal of Physical Oceanography*, *16*, 2137–2149.

Chapman, D. C., and S. J. Lentz (1994), Trapping of a coastal density front by the bottom boundary layer, *Journal of Physical Oceanography*, *24*, 1464–1479.

Chen, F., and D. G. MacDonald (2006), Role of mixing in the structure and evolution of a buoyant discharge plume, *Journal of Geophysical Research*, *111*, C11002, doi:10.1029/2006JC003563.

Chen, F., D. G. MacDonald, and R. D. Hetland (2009), Lateral spreading of a near-field river plume: Observations and numerical simulations, *Journal of Geophysical Research*, *114*, C07013, doi:10.1029/2008JC004893.

Chen, J.-C. (1980), Studies on gravitational spreading currents, Ph.D. thesis, California Institute of Technology.

De Ruijter, W. P., A. W. Visser, and W. Bos (1997), The Rhine outflow: A prototypical pulsed discharge plume in a high energy shallow sea, *Journal of Marine Systems*, *12*, 263–276.

Dewey, R. K., and W. R. Crawford (1988), Bottom stress estimates from vertical dissipation rate profiles on the continental shelf, *Journal of Physical Oceanography*, *18*, 1167–1177.

Didden, N., and T. Maxworthy (1982), The viscous spreading of plane and axisymmetric gravity currents, *Journal of Fluid Mechanics*, *121*, 27–42.

Drazin, P. G., and W. H. Reid (2004), *Hydrodynamic Stability*, 2 ed., Cambridge University Press.

Farmer, D. M., and L. Armi (1986), Maximal two-layer exchange over a sill and through the combination of a sill and contraction with barotropic flow, *Journal of Fluid Mechanics*, *164*, 53–76.

Flater, D. (2007), Xtide version 2.9.5, http://www.flaterco.com/xtide/.

Flater, D. (2008), Xtide version 2.9.5, http://www.flaterco.com/xtide/, data file: harmonics-dwf-20070318-free.tcd.

Fong, D. A., and W. R. Geyer (2001), Response of a river plume during an upwelling favorable wind event, *Journal of Geophysical Research*, *106*, 1067–1084.

Fong, D. A., and W. R. Geyer (2002), The alongshore transport of freshwater in a surface-trapped river plume, *Journal of Physical Oceanography*, *32*, 957–972, doi:10.1175/1520-0485(2002)032⟨0957:TATOFI⟩2.0.CO;2.

Fong, D. A., W. R. Geyer, and R. P. Signell (1997), The wind-forced response of a buoyant coastal current: Observations of the western Gulf of Maine plume, *Journal of Marine Systems*, *12*, 69–81.

Gander, W., G. H. Golub, and R. Strebel (1994), Least-squares fitting of circles and ellipses, *BIT Numerical Mathematics*, *34*, 558–578.

Garvine, R. W. (1974a), Physical features of the Connecticut River outflow during high discharge, *Journal of Geophysical Research*, *79*(6), 831–846.

Garvine, R. W. (1974b), Dynamics of small-scale oceanic fronts, *Journal of Physical Oceanography*, *4*, 557–569.

Garvine, R. W. (1982), A steady state model for buoyant surface plume hydrodynamics in coastal waters, *Tellus*, *34*, 293–306.

Garvine, R. W. (1984), Radial spreading of buoyant, surface plumes in coastal waters, *Journal of Geophysical Research*, *89*, 1989–1996.

Garvine, R. W. (1987), Estuary plumes and fronts in shelf waters: A layer model, *Journal of Physical Oceanography*, *17*, 1877–1896.

Garvine, R. W. (1995), A dynamical system for classifying buoyant coastal discharges, *Continental Shelf Research*, *15*, 1585–1596.

Garvine, R. W., and J. D. Monk (1974), Frontal structure of a river plume, *Journal of Geophysical Research*, *79*(15), 2251–2259.

Geyer, R. W., R. C. Beardsley, J. Candela, M. Castro, R. V. Legeckis, S. J. Lentz, R. Limeburner, L. B. Miranda, and J. H. Trowbridge (1991), The physical oceanography of the Amazon outflow, *Oceanography*, *4*, 8–14.

Geyer, R. W., P. Hill, T. Milligan, and P. Traykovski (2000), The structure of the Eel River plume during floods, *Continental Shelf Research*, *20*, 2067–2093.

Geyer, R. W., M. E. Scully, and D. K. Ralston (2008), Quantifying vertical mixing in estuaries, *Environmental Fluid Mechanics*, *8*, 495–509, doi:10.1007/s10652-008-9107-2.

Halpern, B. S., et al. (2008), A global map of human impact on marine ecosystems, *Science*, *319*, 948–952.

Hansen, D. V., and M. Rattray, Jr. (1965), Gravitation circulation in straits and estuaries, *Journal of Marine Research*, *23*, 104–122.

Hansen, D. V., and M. Rattray, Jr. (1966), New dimensions in estuary classification, *Limnology and Oceanography*, *11*, 319–326.

Hetland, R. D. (2005), Relating river plume structure to vertical mixing, *Journal of Physical Oceanography*, *35*, 1667–1688, doi:10.1175/JPO2774.1.

Hetland, R. D. (2010), The effects of mixing and spreading on density in near-field river plumes, *Dynamics of Atmospheres and Oceans*, *49*(1), 37–53, doi:10.1016/j.dynatmoce.2008.11.003.

Hetland, R. D., and D. G. MacDonald (2008), Spreading in the near-field Merrimack River plume, *Ocean Modelling*, *21*, 12–21, doi:doi:10.1016/j.ocemod.2007.11.001.

Hickey, B. M., G. N. Kachel, and A. MacFadyen (2005), A bi-directional river plume: The Columbia in summer, *Continental Shelf Research*, *25*, 1631–1656, doi:10.1016/j.csr.2005.04.010.

Hickey, B. M., R. M. McCabe, S. Geier, E. Dever, and N. Kachel (2009), Three interacting freshwater plumes in the northern California Current system, *Journal of Geophysical Research*, *114*, C00B03, doi:10.1029/2008JC004907.

Hickey, B. M., et al. (2010), River influences on shelf ecosystems: Introduction and synthesis, *Journal of Geophysical Research*, *115*, C00B17, doi:10.1029/2009/JC005452.

Horner-Devine, A. (2009), The bulge circulation in the Columbia River plume, *Continental Shelf Research*, *29*, 234–251, doi:10.1016/j.csr.2007.12.012.

Horner-Devine, A., D. A. Jay, P. M. Orton, and E. Y. Spahn (2009), A conceptual model of the strongly tidal Columbia River plume, *Journal of Marine Systems*, *78*, 460–475, doi:10.1016/j.jmarsys.2008.11.025.

Houghton, R. W., C. E. Tilburg, R. W. Garvine, and A. Fong (2004), Delaware River plume response to a strong upwelling-favorable wind event, *Geophysical Research Letters*, *31*, L07,302, doi:10.1029/2003GL018988.

Hoult, D. (1972), Oil spreading on the sea, *Annual Review of Fluid Mechanics*, *4*, 341–368.

Imberger, J., and G. N. Ivey (1991), On the nature of turbulence in a stratified fluid. part ii: Application to lakes, *Journal of Physical Oceanography*, *21*, 650–658.

Jay, D. A., and J. D. Smith (1990a), Circulation, density distribution and neap-spring transitions in the Columbia River estuary, *Progress in Oceanography*, *25*, 81–112.

Jay, D. A., and J. D. Smith (1990b), Residual circulation in shallow estuaries 1. highly stratified, narrow estuaries, *Journal of Geophysical Research*, *95*, 711–731.

Jay, D. A., E. D. Zaron, and J. Pan (2010), Initial expansion of the Columbia River tidal plume: Theory and remote sensing observations, *Journal of Geophysical Research*, *115*, C00B15, doi:10.1029/2008JC004996.

Jones, G. M., J. D. Nash, R. L. Doneker, and G. H. Jirka (2007), Buoyant surface discharges into water bodies. I: Flow classification and prediction methodology, *Journal of Hydraulic Engineering*, *133*, 1010–1020, doi:10.1061/(ASCE)0733-9429(2007)133:9(1010).

Kay, D. J., and D. A. Jay (2003), Interfacial mixing in a highly stratified estuary; 2. A "method of constrained differences approach for the determination of the momentum and mass balances and the energy of mixing, *Journal of Geophysical Research*, *108*, 3073, doi:10.1029/2000JC000253.

Kilcher, L. F., and J. D. Nash (2010), Structure and dynamics of the Columbia River tidal plume front, *Journal of Geophysical Research*, *115*, C05S90, doi:10.1029/2009JC006066.

Kunze, E., A. J. I. Williams, and M. G. Briscoe (1990), Observartions of shear and vertical stability from a neutrally buoyant float, *Journal of Geophysical Research*, *95*(C10), 18,127–18,142.

Large, W. G., and S. Pond (1981), Open ocean momentum flux measurements in moderate to strong winds, *Journal of Physical Oceanography*, *11*, 324–336.

Lentz, S. J., and J. Largier (2006), The influence of wind forcing on the Chesapeake Bay buoyant coastal current, *Journal of Physical Oceanography*, *36*, 1305–1316, doi:10.1175/JPO2909.1.

Luketina, D. A., and J. Imberger (1987), Characteristics of a surface buoyant jet, *Journal of Geophysical Research*, *92*, 5435–5447.

Luketina, D. A., and J. Imberger (1989), Turbulence and entrainment in a buoyant surface plume, *Journal of Geophysical Research*, *94*, 12,619–12,636.

MacCready, P., R. D. Hetland, and W. R. Geyer (2002), Long-term isohaline salt balance in an estuary, *Continental Shelf Research*, *22*, 1591–1601, doi:10.1016/S0278-4343(02)00023-7.

MacDonald, D. G., and W. R. Geyer (2004), Turbulent energy production and entrainment at a highly stratified estuarine front, *Journal of Geophysical Research*, *109*, C05004, doi:10.1029/2003JC002094.

MacDonald, D. G., L. Goodman, and R. D. Hetland (2007), Turbulent dissipation in a near-field river plume: A comparison of control volume and microstructure observations with a numerical model, *Journal of Geophysical Research*, *112*, C07026, doi:10.1029/2006JC004075.

MacKinnon, J. A., and M. C. Gregg (2003), Mixing on the late-summer New England shelf – solibores, shear and stratification, *Journal of Physical Oceanography*, *33*, 1476–1492, doi:10.1175/1520-0485(2003)033⟨1476:MOTLNE⟩2.0.CO;2.

Marmorino, G. O., and C. L. Trump (2000), Gravity current structure of the Chesapeake Bay outflow plume, *Journal of Geophysical Research*, *105*(C12), 28,847–28,861.

Marmorino, G. O., A. L. Cooper, R. P. Mied, G. J. Lindemann, D. B. Trizna, and D. L. Porter (2004), Onshore propagation of a buoyant ocean front observed using a shore-based marine radar, *Continental Shelf Research*, *24*, 951–964, doi:10.1016/j.csr.2004.03.011.

McCabe, R. M., B. M. Hickey, and P. MacCready (2008), Observational estimates of entrainment and vertical salt flux in the interior of a spreading river plume, *Journal of Geophysical Research*, *113*, C08027, doi:10.1029/2007JC004361.

McCabe, R. M., P. MacCready, and B. M. Hickey (2009), Ebb tide dynamics and spreading of a large river plume, *Journal of Physical Oceanography*, *39*, 2839–2856, doi:10.1175/2009JPO4061.1.

McClimans, T. (1978), Fronts in fjords, *Geophysical and Astrophysical Fluid Dynamics*, *11*, 23–34.

Moore, K. D., and M. P. Nelson (Eds.) (2010), *Moral Ground: Ethical action for a planet in peril*, Trinity University Press.

Moum, J. N. (1990), The quest for K_ρ - preliminary results from direct measurements of turbulent fluxes in the ocean, *Journal of Physical Oceanography*, *20*(12), 1980–1984.

Moum, J. N., M. Gregg, R. C. Lien, and M. E. Carr (1995), Comparison of turbulence kinetic energy dissipation rate estimates from two ocean microstrucure profilers, *Journal of Atmospheric and Oceanic Technology*, *12*(2), 346–366.

Moum, J. N., J. M. Klymak, J. D. Nash, A. Perlin, and W. D. Smyth (2007), Energy transport by nonlinear internal waves, *Journal of Physical Oceanography*, *37*, 1968–1988, doi:10.1175/JPO3094.1.

Nash, J. D., and J. N. Moum (2001), Internal hydraulic flows on the continental shelf: High drag states over a small bank, *Journal of Geophysical Research*, *106*(C3), 4593–4611.

Nash, J. D., and J. N. Moum (2005), River plumes as a source of large-amplitude internal waves in the coastal ocean, *Nature*, *437*, 400–403, doi: 10.1038/nature03936.

Nash, J. D., L. F. Kilcher, and J. N. Moum (2009), Structure and composition of a strongly stratified, tidally pulsed river plume, *Journal of Geophysical Research*, *114*, C00B12, doi:10.1029/2008JC005036.

O'Donnell, J. (1990), The formation and fate of a river plume: A numerical model, *Journal of Physical Oceanography*, *20*, 551–569.

Orton, P. M., and D. A. Jay (2005), Observations at the tidal plume front of a high-volume river outflow, *Geophysical Research Letters*, *32*, L11,605, doi: 10.1029/2005GL022372.

Pritchard, D. W. (1955), Estuarine circulation patterns, *Proceedings of the American Society of Civil Engineers*, *81*(717), 1–9.

Pritchard, D. W. (1967), *Estuaries*, chap. What is an estuary: physical viewpoint, pp. 3–5, AAAS.

Rottman, J., and J. Simpson (1983), The initial development of gravity currents from fixed-volume releases of heavy fluids, in *Atmospheric Dispersion of Heavy Gases and Small Particles*, edited by G. Ooms and H. Tennekes, pp. 347–359, IUTAM Symposium, Springer-Verlag, New York.

Scarpace, F., and T. Green III (1973), Dynamic surface temperature structure of thermal plumes, *Water Resources Research*, *9*, 138–153.

Sherwood, C. R., D. A. Jay, R. B. Harvey, P. Hamilton, and C. A. Simenstad (1990), Historical changes in the Columbia River estuary, *Progress in Oceanography*, *25*, 299–352.

Shin, J. O., S. B. Dalziel, and P. F. Linden (2004), Gravity currents produced by lock exchange, *Journal of Fluid Mechanics*, *521*, 1–34, doi:10.1017/S002211200400165X.

Simenstad, C. A., L. F. Small, C. D. McIntire, D. A. Jay, and C. R. Sherwood (1990), Columbia River estuary studies: An introduction to the estuary, a brief history, and prior studies, *Progress in Oceanography*, *25*, 1–13.

Simpson, J. E. (1982), Gravity currents in the laboratory, atmosphere, and ocean., *Annual Review of Fluid Mechanics*, *14*, 213–234.

Simpson, J. H. (1997), Physical processes in the ROFI regime, *Journal of Marine Systems*, *12*, 3–15.

Spahn, E. Y., A. R. Horner-Devine, J. D. Nash, and L. F. Kilcher (2009), Particle re-suspension in the Columbia River plume near-field, *Journal of Geophysical Research*, *114*, C00B14, doi:10.1029/2008JC004986.

Stashchuk, N., and V. Vlasenko (2009), Generation of internal waves by a supercritical stratified plume, *Journal of Geophysical Research*, *114*, C01004, doi:10.1029/2008JC004851.

Ungarish, M., and H. E. Huppert (1998), The effects of rotation on axisymmetric gravity currents, *Journal of Fluid Mechanics*, *362*, 17–51.

Ungarish, M., and H. E. Huppert (2004), On gravity currents propagating at the base of a stratified ambient: effects of geometrical constraints and rotation, *Journal of Fluid Mechanics*, *521*, 69–104, doi:10.1017/S0022112004000965.

Verdin, K. L., and J. P. Verdin (1999), A topological system for delineation and codifcation of the Earth's river basins, *Journal of Hydrology*, *218*, 1–12.

Vörösmarty, C. J., et al. (2010), Global threats to human water security and river biodiversity, *Nature*, *467*, 555–561, doi:10.1038/nature09440.

White, B. L., and K. R. Helfrich (2008), Gravity currents and internal waves in a stratified fluid, *Journal of Fluid Mechanics*, *616*, 327–356, doi:10.1017/S0022112008003984.

Wright, L. D., and J. M. Coleman (1971), Effluent expansion and interfacial mixing in the presence of a salt wedge, Mississippi River delta, *Journal of Geophysical Research*, *76*(36), 8649–8661.

Yankovsky, A. E., and D. C. Chapman (1997), A simple theory for the fate of buoyant coastal discharges, *Journal of Physical Oceanography*, *27*, 1386–1401.